Technical Report

TR-00-08

# Evaluation of the conservativeness of the methodology for estimating earthquake-induced movements of fractures intersecting canisters

Paul R La Pointe, Trenton T Cladouhos
Golder Associates Inc, USA

Nils Outters, Sven Follin
Golder Grundteknik KB, Stockholm

April 2000

**Svensk Kärnbränslehantering AB**
Swedish Nuclear Fuel
and Waste Management Co
Box 5864
SE-102 40 Stockholm Sweden
Tel 08-459 84 00
+46 8 459 84 00
Fax 08-661 57 19
+46 8 661 57 19

# Evaluation of the conservativeness of the methodology for estimating earthquake-induced movements of fractures intersecting canisters

Paul R La Pointe, Trenton T Cladouhos
Golder Associates Inc, USA

Nils Outters, Sven Follin
Golder Grundteknik KB, Stockholm

April 2000

# ABSTRACT

This study evaluates the parameter sensitivity and the conservativeness of the methodology outlined in TR 99-03 (La Pointe and others, 1999). Sensitivity analysis focuses on understanding how variability in input parameter values impacts the calculated fracture displacements. These studies clarify what parameters play the greatest role in fracture movements, and help define critical values of these parameters in terms of canister failures. The thresholds or intervals of values that lead to a certain level of canister failure calculated in this study could be useful for evaluating future candidate sites. Key parameters include:

1. magnitude/frequency of earthquakes;
2. the distance of the earthquake from the canisters;
3. the size and aspect ratio of fractures intersecting canisters; and
4. the orientation of the fractures.

The results of this study show that distance and earthquake magnitude are the most important factors, followed by fracture size. Fracture orientation is much less important. Regression relations were developed to predict induced fracture slip as a function of distance and either earthquake magnitude or slip on the earthquake fault. These regression relations were validated by using them to estimate the number of canister failures due to single damaging earthquakes at Aberg, and comparing these estimates with those presented in TR 99-03.

The methodology described in TR 99-03 employs several conservative simplifications in order to devise a numerically feasible method to estimate fracture movements due to earthquakes outside of the repository over the next 100,000 years. These simplifications include:

1. fractures are assumed to be frictionless and cohesionless;
2. all energy transmitted to the fracture by the earthquake is assumed to produce elastic deformation of the fracture; no energy is diverted into fracture propagation; and
3. shielding effects of other fractures between the earthquake and the fracture are neglected. The numerical modeling effectively assumes that the rock is completely intact between the fault on which the earthquake occurs and the fracture that intersects the canister.

As detailed in TR 99-03, these assumptions are conservative in that the calculated displacements are larger than they would be if the simplifications had not been made. Conservativeness was quantified by using an advanced three-dimensional fracture mechanics code, FRANC3D (Cornell University Fracture Group, 1998) together with POLY3D (Thomas, 1993). The results show that the probability of fracture movements exceeding a displacement threshold of 0.1 m is considerably less than that reported in TR 99-03.

# SAMMANFATTNING

Föreliggande studie utvärderar parameterkänslighet och graden av konservatism i den metodik som används i SKB TR 99-03 (La Pointe m fl, 1999). Känslighetsanalysen fokuseras på att förstå hur variabiliteten i indata påverkar de beräknade spricknätverks-förskjutningarna. Studierna tydliggör vilka parametrar som har störst betydelse vid sprickrörelser och hjälper till att definiera kritiska värden för dessa parametrar med hänsyn till risken för kapselbrott. De gränsvärden eller intervall av värden som leder till given grad av kapselbrott i föreliggande studie skulle kunna användas för att utvärdera framtida kandidatområden. Viktiga parametrar inkluderar:

1. magnitud och frekvens hos jordbävningar,
2. avståndet mellan jordbävningen och kapslarna,
3. storlek och längd-bredd förhållande hos sprickor som skär kapselhålen, och
4. orienteringen hos sprickorna.

Resultaten i denna studie visar att avstånd och jordbävningsmagnitud är de viktigaste faktorerna följt av sprickstorlek. Sprickorientering spelar mycket mindre roll. Regressionssamband har tagits fram för att prediktera inducerade sprickförskjutningar som funktion av avstånd och, endera, jordbävningsmagnitud eller jordbävningsför-skjutning. Regressionssambanden validerades genom att använda dem för att skatta antalet kapselbrott för enskilda, skadande, jordbävningar i Aberg och jämföra dessa skattningar med de skattningar som presenterades i TR 99-03.

Metodiken, som beskrivs i TR 99-03, bygger på ett flertal konservativa förenklingar för att kunna ta fram en numeriskt ändamålsenlig metod att skatta sprickrörelser på grund av jordbävningar vid sidan av djupförvaret under de kommande 100 000 åren. Dessa förenklingar inkluderar:

1. sprickorna antas sakna friktion och kohesion,
2. all energi som överförs till sprickan från jordbävningen antas orsaka elastisk deformation av sprickan; ingen energi tas upp som sprickpropagering; och
3. skyddande effekter hos andra sprickor, som finns mellan jordbävningen och sprickan, försummas. Den numeriska modelleringen bygger helt och hållet på antagandet att berget är fullständigt intakt mellan förkastningen, där jordbäv-ningen sker, och sprickan vid kapselhålet.

Som beskrivits i TR 99-03 är ovanstående antaganden konservativa i den mening att beräknade förskjutningar är större än de skulle vara om förenklingarna inte hade gjorts. Graden av konservatism har kvantifierats med hjälp av en avancerad tredimensionell sprickmekanisk programkod FRANC3D (Cornell University Fracture Group, 1998) tillsammans med POLY3D (Thomas, 1993). Resultaten visar att sannolikheten för sprickrörelser större än tröskelvärdet 0,1 m är betydligt mindre än vad som rapporterats i TR 99-03.

# TABLE OF CONTENTS

# LIST OF FIGURES

# LIST OF TABLES

# 1 INTRODUCTION

A methodology to estimate the movements of fractures intersecting canisters due to earthquakes was devised in TR 97-07 (La Pointe and others, 1997). It was subsequently further developed and applied to the three generic sites, Aberg, Beberg and Ceberg in TR 99-03 (La Pointe and others, 1999). The estimates of movements and potential canister failures resulting from these movements were for a 100,000 year time period, and were based on the earthquake magnitude-frequency relations established for the geographic regions in which these three site lie and the site structural geology. Canister failure risk was expressed by several different measures:

- the number of damaging earthquakes at each site over the 100,000 period;
- the percentage of canister failures expected for each damaging earthquake;
- the probability of canister failures due to the cumulative slip of multiple, non-damaging earthquakes;
- the probability of canister failure due to damaging earthquakes; and
- the probability of canister failure due to both damaging earthquakes and cumulative effects.

The term damaging earthquake is used in TR 99-03 to refer to a single earthquake that induces 0.1 m or more displacement on any fracture intersecting a canister.

In addition, the horizontal distance between the center of the earthquake rupture and the fractures whose slip exceed the threshold 0.1m displacement was studied for Ceberg. The results showed that most damaging earthquakes (>95%) occurred within a kilometer.

Although the probability of induced slips exceeding 0.1 m was very low, and many credible sets of parameter assumptions produced no canister failures, a few sets of parameter value assumptions led to one or two canisters over the 100,000-year performance period. The question arises as to whether these one or two failures are mostly a result of the underlying conservativeness of the method or not.

The methodology described in TR 99-03 employs several conservative simplifications to make the numerical calculations feasible. These simplifications include (Figure 1-1):

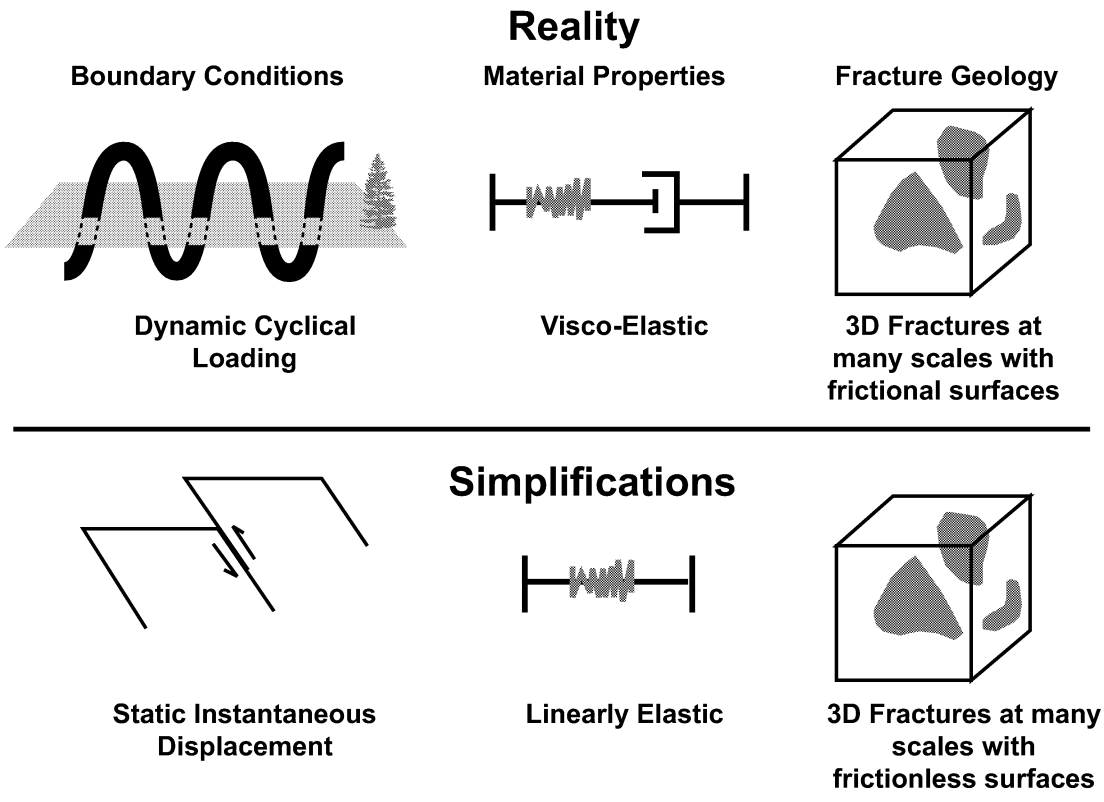


*Figure 1-1 Conservative simplications used in TR 99-03 for estimating the slip on fractures induced by earthquakes*

- fractures are assumed to be frictionless and cohesionless;
- all energy transmitted to the fracture by the earthquake is assumed to produce elastic deformation of the fracture; no energy is diverted into fracture propagation; and
- shielding effects of other fractures between the earthquake and the fracture are neglected. The numerical modeling effectively assumes that the rock is completely intact between the fault on which the earthquake occurs and the fracture that intersects the canister.

TR 99-03 describes how these assumptions simplify the numerical modeling process and also lead to conservative estimates of displacement. Since these conservative calculations predicted some canister failures, it would be useful to quantify how conservative, in practice, these estimates might actually be.

The work reported in TR 97-07 and TR 99-03 illustrated how induced fracture slip related, in a general sense, to such parameters as earthquake magnitude, distance

between the earthquake and the fracture, and fracture size. These general tendencies suggested that a more systematic analysis of parameter sensitivity could enhance the methodology's usefulness. For example, a better understanding of sensitivity could make it possible to derive criteria for ranking sites in terms of easily measurable parameter values like regional earthquake source parameters, the size of nearby lineaments, or the size distribution of fractures within the repository block. Establishment of threshold values for these parameters from the sensitivity analyses might also provide tools for preliminary site screening or risk evaluation.

For these reasons, the current study focuses on evaluating the parameter sensitivity and the conservativeness of the methodology outlined in TR 99-03. Because some of the conclusions from the sensitivity analysis are relevant to conclusions drawn from the analysis of the conservativeness of the modeling assumptions, the sensitivity analysis is presented first. The strategy for evaluating sensitivity and conservativeness is described in the next two sections.

## 1.1 Sensitivity Analysis

### 1.1.1 Background

Sensitivity analysis focuses on understanding how variability in input parameter values impacts the calculated fracture displacements. The numerical modeling approach described in TR 99-03 relies upon the assignment of values for several parameters. The first series of parameters have to do with the magnitude and frequency of future earthquakes, which is described by two parameters, $a$ and $b$, according to the equation:

$$Log(N) = -bm + Log(a) \tag{1}$$

where $N$ is the number of earthquakes in a specified length of time,

$m$ is the magnitude, and

$a$ and $b$ are parameters that are estimated from measured earthquakes.

The parameter, $b$, describes the ratio of the number of large magnitude earthquakes to small magnitude earthquakes. As $b$ decreases, the proportion of large earthquakes increases. The parameter, $a$, describes the areal density of all earthquakes.

Values of $a$ and $b$ have been calculated for various regions of Sweden, as well as for many other surrounding areas. TR 99-03 utilized four different sets of $a$ and $b$ values to assess risk at the generic sites. The results indicated that lower $b$ values or higher $a$ values lead to higher canister failures.

The numerical code Poly3D (Thomas, 1993) is used to estimate the induced slips on fractures intersecting canisters for each future earthquake in TR 99-03. Poly3D requires specification of several parameter values having to do both with the fractures intersecting canisters, and also the earthquake rupture itself.

Each earthquake is represented as an instantaneous displacement on a plane represented by a rectangle (Figure 1-2). The rectangle has a horizontal extent and a down-dip extent, an orientation and a location. The instantaneous displacement is assumed to be uniform over the entire rectangle.

Wells and Coppersmith (1994) showed that the horizontal extent, the down-dip extent (often termed the *width*), and the instantaneous displacement are strongly correlated with the moment magnitude and slip type. Thus, specification of the earthquake magnitude makes it possible to specify parameter values for the rupture surface size and instantaneous displacement, and this approach was adopted in TR 99-03. The relations between these parameters and earthquake moment magnitude sometimes differ by fault type. Only the regressions derived for strike-slip faults are used in this report. This is because the strike-slip regressions predict the largest slip for earthquakes of a particular magnitude (see Figure 2-5, TR 97-07) except at the largest magnitudes. At the largest magnitudes, reverse faults have slightly larger slips but these predictions are not significant at the 95% probability level, and thus are not used.

The regression relations for strike-slip faults are (Wells and Coppersmith 1994):

$$\log(AD) = 0.90 * M - 6.32 \tag{2}$$

$$\log(MD) = 1.03 * M - 7.03 \tag{3}$$

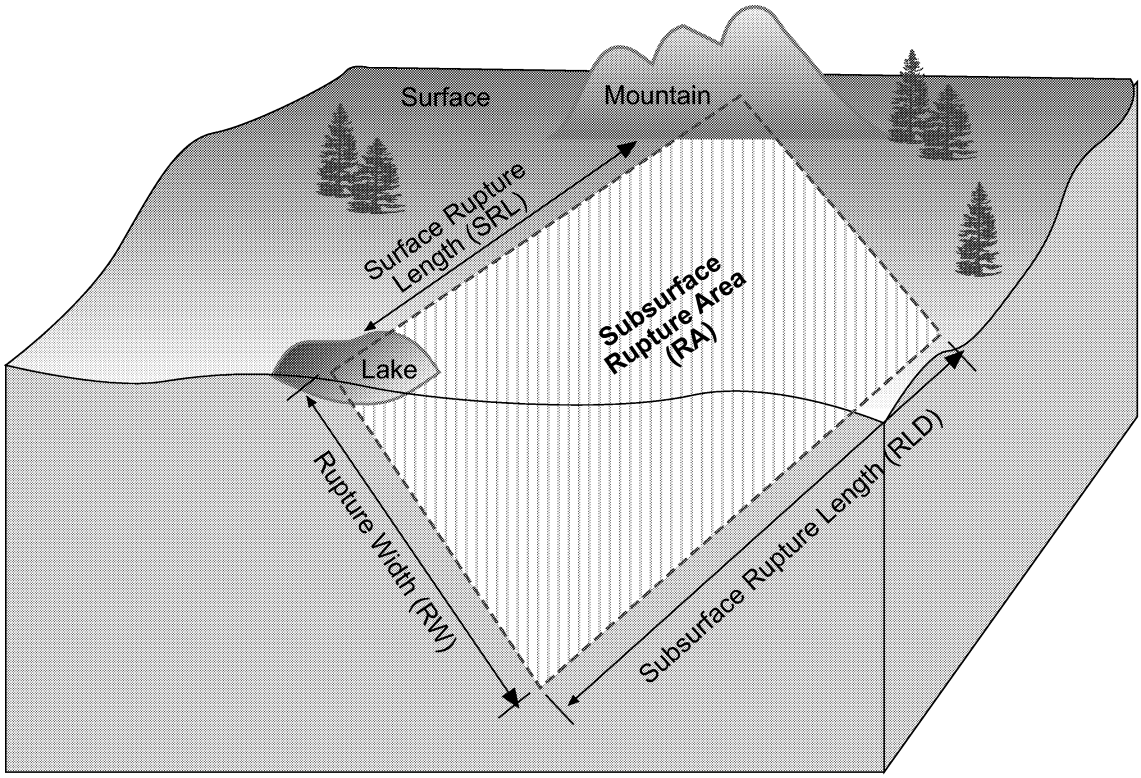


| Key Parameters: | Use: |
|---|---|
| SRL vs. M | Estimate M from SRL |
| Displacement vs. M | Estimate Displacement from M |
| RW vs. M<br>RLD vs. M | Determine fault length and width as a function of M |

Where:

M = 2/3 log $M_0$ - 10.7 (Hanks and Kanamori, 1970)
$M_0$ = μ x D x RA
μ = shear modulus
D = average displacement
RA = rupture area

*Figure 1-2 Parmeters used to describe an earthquake rupture*

$$\log(RW) = 0.27 * M - 0.76 \quad (4)$$

$$\log(RLD) = 0.62 * M - 2.57 \quad (5)$$

where M is the moment magnitude, AD is average displacement, MD is maximum displacement, RW is downdip rupture width, and RLD is subsurface rupture length.

An additional regression was carried out in TR 97-07 (**Table** 2-4, pg. 24) to relate magnitude and subsurface displacement (SD). For strike-slip faults, the relation was found to be:

$$\log(SD) = 0.47 * M - 2.95 \quad (6)$$

Table 1-1 shows the predicted parameters for earthquakes between Magnitude 2 and 8. The regression relations are based on medium to large earthquakes, and so their extrapolation of smaller magnitude earthquakes is uncertain.

**Table 1-1 Rupture parameters of strike-slip faults (from Wells and Coppersmith, 1994, and TR-97-07, Table 2-3b & Table 2-4)**

| Magnitude | Average Surface Slip (m) | Maximum Surface Slip (m) | Subsurface Slip (m) | Width (km) | Length (km) |
|---|---|---|---|---|---|
| 2 | 3.02E-05 | *Maximum Surface Slip regression not significant for these magnitudes* | 0.010 | 0.60 | 0.05 |
| 2.5 | 8.51E-05 | | 0.017 | 0.82 | 0.10 |
| 3 | 2.40E-04 | | 0.029 | 1.12 | 0.19 |
| 3.5 | 6.76E-04 | | 0.050 | 1.53 | 0.40 |
| 4 | 1.91E-03 | | 0.085 | 2.09 | 0.81 |
| 4.5 | 5.37E-03 | | 0.146 | 2.85 | 1.66 |
| 5 | 1.51E-02 | | 0.251 | 3.89 | 3.39 |
| 5.5 | 0.04 | 0.04 | 0.43 | 5.31 | 6.92 |
| 6 | 0.12 | 0.14 | 0.74 | 7.24 | 14.13 |
| 6.5 | 0.34 | 0.46 | 1.27 | 9.89 | 28.84 |
| 7 | 0.95 | 1.51 | 2.19 | 13.49 | 58.88 |
| 7.5 | 2.69 | 4.95 | 3.76 | 18.41 | 120.23 |
| 8 | 7.59 | 16.22 | 6.46 | 25.12 | 245.47 |

In TR 99-03, large magnitude earthquakes were situated on existing lineaments, while smaller earthquakes were assigned random spatial locations and orientations.

The relation between earthquake magnitude and slip may be somewhat more complex than the power law functions shown in Equations 2, 3, and 6. For eample, some researchers (e.g. Davison and Scholz, 1985; Scholz and Aviles, 1986) have found that small earthquakes may have magnitude/frequency parameter values that differ from those of large earthquakes in the same fault zone. They explain this difference on the basis of the seismogenic thickness and factors that may influence stress drop differently for large ruptures vs. small ruptures. As a result, the displacement/magnitude relations might be different between earthquakes that rupture the entire seismogenic thickness of the lithosphere from those that do not.

However, the data compiled and analyzed by Wells and Coppersmith (1994) suggest that the magnitude/slip relations do not have a discontinuity at or near magnitude 7.0 earthquakes. The regressions between magnitude and displacement reported by Wells and Coppersmith (1994) are significant at the 95% level. Their database includes earthquakes with moment magnitudes from 5.2 to 8.1. There is no obvious break in the data or bad fit in the regression lines corresponding to magnitude 7.0 or thereabouts. For this reason, Wells and Coppersmith's regressions are applied to earthquakes greater than magnitude 7.0

An earthquake is rarely a single rupture event. It is often accompanied by foreshocks and aftershocks that may be of magnitudes significant for considerations of fracture movements. It is common practice when analyzing the main earthquake event and its aftershocks to try to de-convolve the record into separate events if at all possible. Thus, the magnitude of the main shock and significant aftershocks are often identified and are given calculated magnitudes (e.g. Slunga, 1985). The $a$ and $b$ parameter values thus take into account measurable foreshocks and aftershocks.

The major difference between foreshocks or aftershocks and other earthquakes is that aftershocks and foreshocks are correlated in time with the main shock, but were assumed to be uncorrelated in the modeling reported in TR 99-03. However, the net displacement is not a function of the time interval between events, only the number and magnitude of events over the 100 000 year time-period, and the orientation of the fault and fractures. The Poissonian temporal assumption is not strictly correct when talking about the temporal relation between a main shock and after shocks, but (1) the time intervals have no impact on the final calculations, and (2) the Poissonian assumption is the one commonly used in earthquake engineering to estimate seismic risk. For these reasons, the results obtained using the methodology described in TR 99-03 should not be greatly affected by treating foreshocks and aftershocks as temporally-independent events.

The fractures intersecting canisters are described as polygons. The polygons have orientations, sizes and locations. These polygons were created by creating a three-dimensional Discrete Fracture network (DFN) model from measurements of fracture geometric parameters appropriate for each site, and combining it with a canister emplacement hole model for each site to determine which of the fractures intersected canisters. Not all canisters had fractures intersecting them. Moreover, bigger fractures and those with certain orientations were more likely to intersect the canisters, and as a result, the size and orientation statistics that characterize the canister fractures are a biased subset of the overall fracture population.

The displacement on fractures is often classified according to one of three modes (see inset, Figure 1-3). Mode I displacement is normal to the fracture surface and results in a change of fracture pore volume. Mode II displacement consists of shear displacement in the direction perpendicular to the leading edge of the fracture. Mode II displacements are the type of displacements that are of concern for the fractures intersecting canisters in this study, and represent the displacements expected on a fault rupturing due to an earthquake. Mode III displacements consist of shear in the plane of the fracture in the direction parallel to the leading edge of the fracture.

Analysis of the modeling results in TR 99-03 and the numerical simulations performed in TR 97-07 indicated that the distance between the earthquake and the canister was an important factor in the induced displacement. Earthquake impact diminishes with increasing distance. For the Ceberg example, earthquakes more than a few kilometers produced very little induced slip, even for very large magnitude earthquakes. TR 99-03 also showed that the overall percentage of canister failures is a complex function of at least two competing factors: while the impact of an earthquake varies inversely with distance, the *number* of earthquakes (assuming random spatial locations) *increases* with the square of the distance. These two competing considerations tend to define a zone where most of the damaging earthquakes occur. For a particular set of earthquake parameters and fracture parameters at Ceberg, this zone ranged from about 400 m to about 1500 m.

In both TR-97-07 and TR-99-03 the distance from the center of the fault responsible for the earthquake (the epicenter) to the canister was measured. In this report, the distance from the earthquake *tip* is considered to be more fundamental for two reasons. First, as shown in Figure 1-3, the tip is the locus of the maximum elastic strain produced by earthquake slip (Pollard and Segall, 1987). In fact, the minimum elastic strain in the rock adjacent to the earthquake rupture occurs at the earthquake rupture center. Second,

depending on the orientation of the earthquake fault, the shortest distance to the earthquake will be overestimated by the distance to the center, especially for large events. For example, a magnitude 7.5 earthquake which would occur on a 120 km long fault (Table 1-1) with a center at a distance of 70 km would have a tip just 10 km from the repository. To avoid this problem, the distance to the tip of the earthquake is specified in the new simulations, and the rupture geometry is set such that this is also the closest point to the canister. Simulations are also run specifying the earthquake centroid to demonstrate a possible difference between the method used in this report and the previous two reports.

The size of the fracture intersecting the canister also plays a role. Small fractures with the same properties and applied stresses deform less than larger fractures. Thus, larger fractures present a greater potential risk than smaller fractures.

The final parameter for calculating induced slip is the orientation of the target fracture. Some fractures may be oriented such that the loads applied to them by an earthquake are applied primarily normal to the fracture plane, producing little if any slip. Other fractures may be oriented so that the shear stresses are maximized on the fracture, producing much greater slip. In the sensitivity analysis below, the orientation of the target fracture is specified by the trend and plunge of its pole.

These considerations and general relations suggest the following strategy to systematically evaluate parameter sensitivity in the modeling approach undertaken in TR 99-03.

### 1.1.2 Strategy

The sensitivity analyses are separated into two tasks. Task 1.1 describes the results of the sensitivity analyses for the input parameters. Task 1.2 describes the comparison of canister failure predictions made by using the relations established in Task 1.1 with results published in TR 97-07 and TR 99-03, in order to determine the usefulness of the sensitivity analyses for site screening or site comparison purposes.

Task 1.1 consisted of two series of investigations concerning the parameters described in Section 1.1.1. First, earthquake magnitude, distance and azimuthal angle between the nearest earthquake rupture tip and the fracture centroid, fracture orientation, and fracture size were varied simultaneously to roughly determine the relationships between the five variables and induced slip. These simulations required 10,780 runs of Poly3D for both strike-slip movement and reverse movement. Second, simulations were made in which three variables were held constant and just two varied. In the end, the rough simulations proved to be detailed enough to calculate useful empirical relations. Table 1-2 summarizes the parameters varied for the detailed simulations, the range of values used for each variable, and the number of steps for both the initial simulations and the detailed simulations.

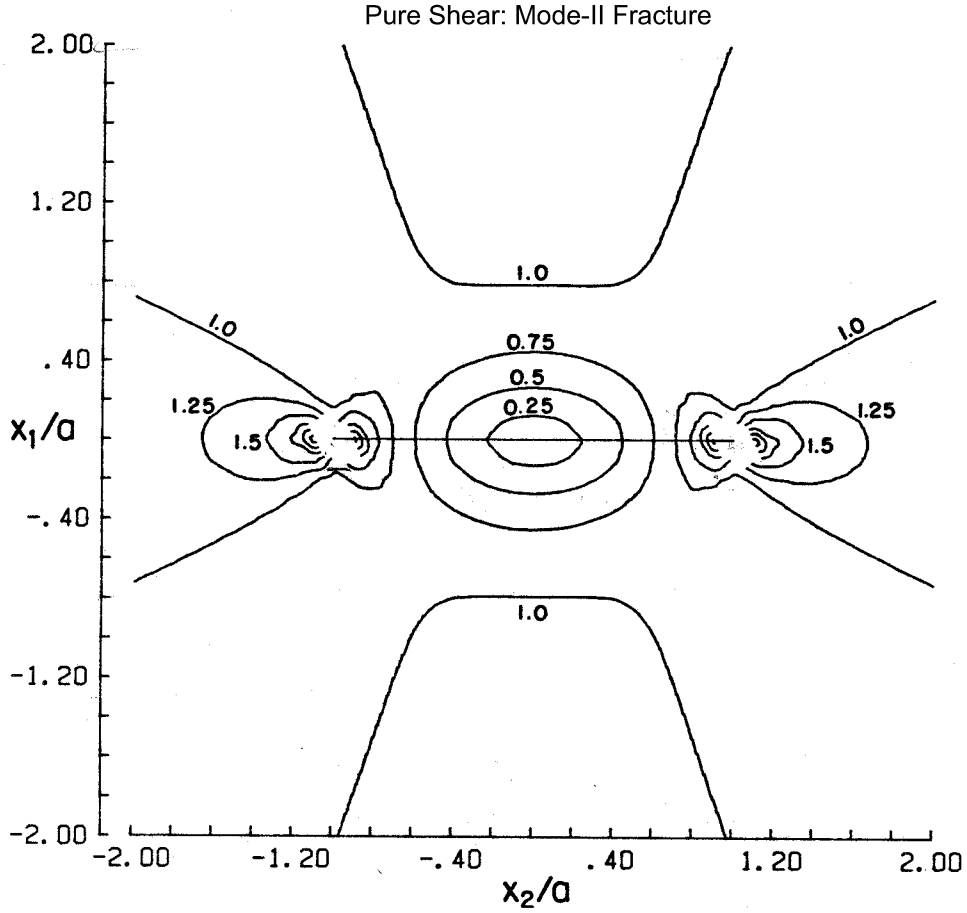


Basic modes of loading involving different crack surface displacements.

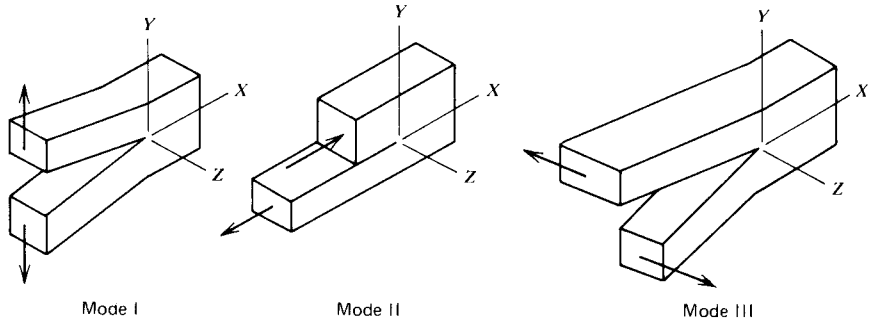


*Figure 1-3 Contour of maximum shear stress in the ($x_1$, $x_2$) plane for mode II crack subjected to unit driving stress (Pollard and Segall, 1987). "a" is the fracture radius, "$x_1$" is the vertical distance perpendicular to the fracture, and "$x_2$" is the distance from the fracture centroid in the direction of fracture propagation*

In all simulations, the earthquake rupture is a north/south-striking, vertical plane, since simultaneously varying both fracture and rupture orientation is redundant. The azimuth parameter refers to the horizontal angle relative to North of a vector beginning at the rupture tip and ending at the fracture centroid.

The results can also be easily applied to a vertical plane with any orientation. The top of the rupture is assumed to be at the ground surface, 500 m above the repository fracture. The length (parallel to the earth's surface) and width (perpendicular to the earth's

surface) and instantaneous displacement are determined by the magnitude, using the regression relations as described in the previous section (Table 1-1).

**Table 1-2 Ranges of parameters for sensitivity analysis**

| Parameter | Range | # Steps Initial | # Steps Detailed | Parameter varied in detailed runs |
|---|---|---|---|---|
| Earthquake Magnitude | 4 to 8 | 7 | -- | -- |
| Distance | 10 m to 100 km | 11 | 21 | Azimuth |
| Fracture Size | 1 m to 1000 km | 4 | -- | -- |
| Azimuth | 0° to 90° | 5 | 7 | Distance & Fracture Orientation |
| Fracture Orientation (Pole trend and plunge) | both 0° to 90° | 7 | 49 | Azimuth |

Task 1.2 focuses on the usefulness of the relations and thresholds deduced from Task 1.1 for purposes of site screening or site comparison. This Task uses the relations to estimate some of the performance measures calculated in TR 99-03, and compares them to the results shown in TR 99-03. Task 1.1 results can be used to predict certain performance measures in two different ways. The first might be most appropriate for relative ranking of sites with little actual site reconnaissance data; the second more appropriate for providing a coarse estimate of canister failures.

The first method, for ranking alternative sites, is as follows:

1. Calculate the maximum induced slip as a function of both earthquake magnitude and distance between the rupture tip and the fracture intersecting the canister for a fracture of constant size. The result of these series of calculations is a lookup table, which gives a maximum induced slip for any combination of earthquake magnitude and distance.

2. Next, calculate the number of earthquakes expected to occur for a given region (100 km circle) around the repository over a given time frame (100,000 years). If the spatial pattern of earthquakes is assumed to be spatially random, then the probability of an earthquake occurring at a distance $r$ from the repository varies as $r^2$. The number of earthquakes is determined from the $a$ and $b$ parameters, and the ratio of the area of interest (a circle of 100 km radius) to the area over which the $a$ and $b$ parameters were calculated. The results can be put into a table that describes the number of expected earthquakes as a function of both distance and magnitude.

3. These two tables can be multiplied. The result is the total slip for each class of earthquake magnitude and distance for the reference fracture.

4. Sum the slips for each magnitude-distance class to estimate the total induced slip for all of the future earthquakes. This represents the total possible induced slip on a single target fracture of a given reference size.

5. This total induced slip could be adjusted for other fracture sizes by multiplying the slip by the ratio of desired fracture radius divided by the reference fracture radius.

6. In order to rank alternative sites, the induced slip might be adjusted to reflect the mean fracture size and the mean fracture multiplied by the fracture intensity, if either of these quantities is known. This measure would provide an index of earthquake risk, but not an actual calculation of canister failure.

More elaborate calculations could be undertaken to estimate canister failure potential. These could be carried out as follows:

1. From knowledge of *a* and *b* values, it is possible to compute the number of earthquakes of a given magnitude for a 100,000 year time period and a circular area of radius 100 km around the repository site. The locations of the earthquake are assumed to be random. The fracture sizes and the relative orientation between fault and fractures are not yet specified.

2. Determine a target fracture size distribution. Assume that the probability of a fracture intersecting a canister is proportional to its radius, which is true for circular fractures. Using the size distribution reported in TR 99-03, calculate the target size fracture distribution.

3. Use the results reported in TR 99-03 to estimate what percentages of these fractures actually intersect canisters.

4. Use the relation developed in the sensitivity analyses to estimate the displacements on these fractures for worst case and best case orientation models.

5. Modify these results using results from the orientation sensitivity analysis to weight the true relative orientations properly.

6. Calculate the mean percentage of failed canisters, the mean displacements, and the number of damaging earthquakes. Compare results to those reported in TR 99-03.

If the comparison is successful, then this six-step methodology can be used to quickly estimate earthquake risk from reconnaissance data without using the numerical models or having to undertake extensive site investigations.

In order to apply this method, it is necessary to specify the magnitude/frequency of earthquakes.

Table 1-3 shows the number of earthquakes predicted for magnitudes between 3.5 and 8.0 within a 100 km radius of a generic repository using the same *a* and *b* parameters as in TR 99-03. In this table, $\lambda_{2.4}$ represents the number of earthquakes with magnitudes greater than or equal to magnitude 2.4 expected to occur in one year within the area of the earthquake catalog. The magnitude/frequency parameter values used in this and previous studies were taken from work by Kijko and others (1993), who used a reference magnitude of 2.4 for their calculations. *b* is the Gutenberg-Richter parameter (Equation 1) that essentially describes the proportion of large magnitude earthquakes to small magnitude earthquakes. As *b* decreases, there are proportionally more large earthquakes. The value of *a* shown in Equation 1 can be calculated from $\lambda_{2.4}$, *b* and the reference magnitude. Not all of the *a* and *b* parameter values evaluated in TR 99-03 were selected. The two sets of earthquake parameters that were selected constitute the two sets that both pertain to at least one of the generic sites, and are also likely to cause the greatest number of large earthquakes. The parameters for Northern Sweden produce fewer large earthquakes, and those related to Lake Vänern do not apply to any of the three generic sites.

The numbers listed in the columns for the Gulf of Bothnia and for Southern Sweden are the probability that an earthquake with a magnitude in the range indicated will occur in

100,000 years (from Table 4-3, TR-99-03). The values in this Table form the basis of the calculations reported in Chapter 2.2.

**Table 1-3 Number of earthquakes expected within a 100 km radius over 100,000 years (from Table 4-3 in TR-99-03). Values less than 1.0 imply that the recurrence interval is greater than the 100,000-year time period, suggesting that there may not be an earthquake in that magnitude within the prescribed area and time period.**

| Magnitude | Gulf of Bothnia $b = 1.26$, $\lambda_{2.4} = 2.4$ | Southern Sweden $b = 1.04$, $\lambda_{2.4} = 1.8$ |
|---|---|---|
| 3.5-4.0 | 1272 | 1955 |
| 4.0-4.5 | 298 | 591 |
| 4.5-5.0 | 70 | 178 |
| 5.0-5.5 | 16 | 54 |
| 5.5-6.0 | 3.84 | 16 |
| 6.0-6.5 | 0.8 | 5 |
| 6.5-7.0 | 0.21 | 1.48 |
| 7.0-7.5 | 0.05 | 0.45 |
| 7.5-8.0 | 0.012 | 0.14 |

## 1.2 Conservativeness

### 1.2.1 Background

In TR 97-07 and TR 99-03, the methodology for computation of fracture slip simplified the mechanical processes that occur in order to facilitate the intensive numerical computations required. These simplifications are conservative in the sense that computed induced slips on the fractures intersecting canisters are greater than would be expected had the simplifications not been made. These simplifications include:

1. All energy transmitted to the fracture by the earthquake is assumed to produce elastic deformation of the fracture; no energy is diverted into fracture propagation;

2. Shielding effects of other fractures between the earthquake and the fracture are neglected. The numerical modeling effectively assumes that the rock is completely intact between the fault on which the earthquake occurs and the fracture that intersects the canister; and

3. Fractures are assumed to be frictionless and cohesionless.

Each of these conservative assumptions is treated as a separate Task, and the methodologies for estimating the conservativeness of each is described in the remainder of this section.

### 1.2.2 Fracture Propagation

Fracture propagation effects are evaluated in Task 2.1. Mechanical analysis of rock fracture indicates that for a low state of stress, a fracture will deform. However, at a higher state of stress, the rock surrounding the fracture will collapse and the fracture will propagate. Since the previous work assumed that all energy applied to fractures

intersecting canisters was expended as slip without propagation, it is worthwhile to estimate the conservativeness of this approach.

This can be accomplished by calculating the maximum shear displacement possible before any fracture propagation. In this way it is possible to better understand how conservative the assumption of all energy being dissipated into slip might be. In order to assess this conservativeness, it is not necessary to carry out simulations of the complexity of those in TR 99-03, in which there were thousands of fractures. Rather, the current study focuses on the simple case of a penny shaped-fracture subjected to a loading stress (Figure 1-4). The angle between the fracture plane and the loading stress is 45°, an angle that maximizes shear stress on the plane. Since displacement is a function of fracture size, a sensitivity analysis of the maximum shear displacement as a function of the fracture radius was carried out to determine the maximum shear displacement that is likely to take place prior to propagation as a function of fracture size.

The methodology of the evaluation of the maximum shear displacement in a fracture plane before any propagation is based on the comparison of two distinct cases: the pure propagation and the pure shear displacements in a similar fracture.

The energy required to propagate an existing fracture can be used to estimate the amount of fracture slippage that might occur prior to fracture propagation. First, the minimum amount of energy required to initiate fracture propagation is determined. This energy is a function of the crack geometry, the stress applied to the rock, and the material properties of the rock. It is calculated through a numerical simulation in which the stress applied to the fractured rock is increased until the fracture begins to propagate. Propagation initiation is determined by a failure criterion that is a function of the stress intensity factor around the fracture, as described later in this section. The energy necessary to initiate fracture propagation is denoted as $E_p$. It is assumed that all of the energy up to $E_p$ is dissipated as fracture slip.

A second numerical calculation is carried out to estimate the maximum fracture slip prior to propagation. This is accomplished by applying the same critical stresses that produced $E_p$ to an identical fracture, but in this case, there is no propagation. All of the crack energy goes into normal and shear displacement of the fracture walls. This displacement represents the maximum shear displacement possible prior to fracture propagation.

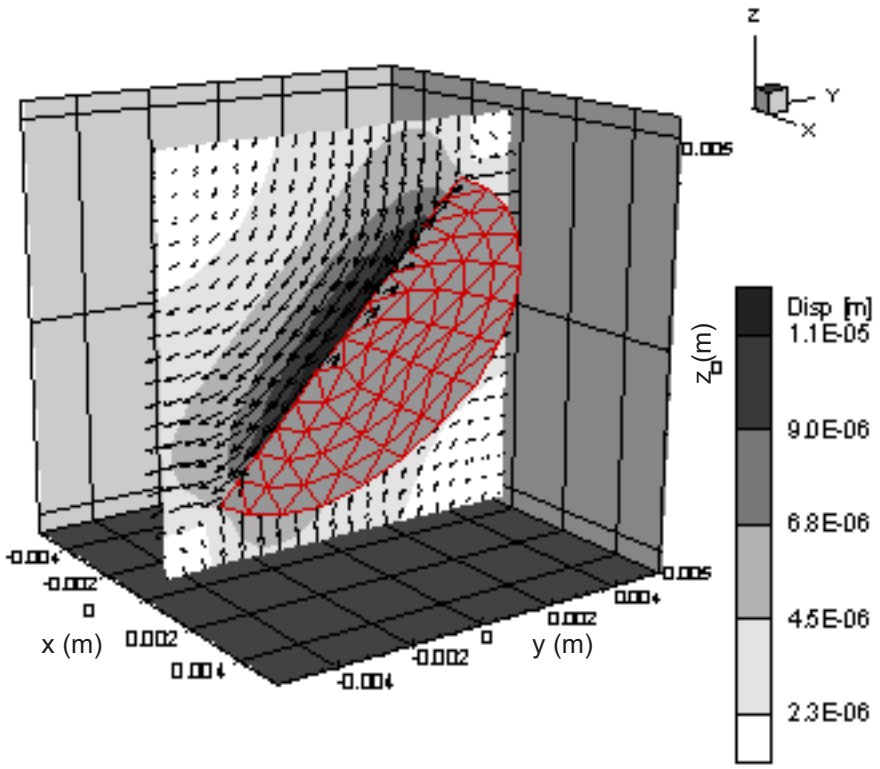


*Figure 1-4 Numerical simulation setup for fracture propagation studies. The arrows represent the direction of displacement, and their lengths the magnitude of displacement. Shaded contours of the displacement magnitudes are also shown to make it easier to distinguish magnitude from direction, as the pattern of arrow lengths is much more difficult to visually separate into regions of similar magnitude.*

These calculations can be carried out through the use of a specialized fracture mechanics code. When the load applied to a fracture in rock mass increases beyond the limits of the fracture to deform, the fracture may propagate. Fracture propagation is a complex process. In most cases, the analysis of the initiation and the propagation of fractures require numerical methods or sophisticated laboratory experiments. Two numerical methods are commonly used to study fracturing: the finite element method (FEM); and the boundary element method (BEM). Finite elements are very useful in that their numerical discretization is such that they can accurately approximate irregular geometry, such as the surface of a crack. However, the solid material away from the crack must also be discretized, which may lead to numerical complications and unnecessary computational effort. Boundary elements, on the other hand, discretize only the boundaries of objects, essentially reducing the dimensionality of the numerical computation by one dimension and avoid the numerical effort of discretizing the solid material in which the fracture occurs. A drawback of boundary elements is that they are not well suited to modeling inhomogeneous materials, which, fortunately, is not an issue for this investigation. Moreover, boundary elements are particularly useful for studying fracture in rock, since only the fracture surface needs to be discretized. Thus, in order to study fracture propagation in three dimensions, it is only necessary to solve the governing equations of stress and strain on the locally two- dimensional fracture surface. For this reason, the boundary element formulation was chosen for this study.

The fracture propagation code Franc3D (Cornell University Fracture Group, 1998) used in this study uses a boundary element discretization for fracture mechanics. Franc3D is a three-dimensional fracture mechanics code developed by the Cornell Fracture Group

at Cornell University. Franc3D computes the stress intensity factors K in mode I, II and III at the fracture tip in three dimensions, and derives the new geometry of the propagated fracture. The Franc3D code has been validated against experiments of three-dimensional fatigue crack growth (Ridell and others, 1997). Fracture propagation will not be modeled in this Task since it is only necessary to calculate the stress intensity factors at the fracture tip.

The propagation criterion used in this study has been proposed by Shen (1993). Its calculation is based on the strain energy release rate in fracture propagation in mode I (pure traction) and mode II (pure shearing). Mode III fracture propagation is not considered in this task.

The criterion has the expression:

$$F = \frac{G_I}{G_{Ic}} + \frac{G_{II}}{G_{IIc}} \tag{7}$$

where

- $F$ is the factor that controls the propagation of the fracture tip. Propagation initiates when $F \geq 1$.
- $G_{I,II}$ are the strain energy release rates in mode I and II.
- $G_{Ic,IIc}$ are the critical strain energy release rates in mode I and II for which the fracture propagate purely in mode I and II respectively.

The $G$-value can be obtained by using the relation:

$$G_{I,II} = \frac{(1-\nu^2)}{E} K_{I,II}^2 \tag{8}$$

where

- $K_{I,II}$ are the stress intensity factor at the crack tip in mode I and II respectively.
- $E$ and $\nu$ and the Young's modulus and the Poisson's ratio of the material respectively.

Replacing Equation (8) in Equation (7) gives:

$$F = \left(\frac{K_I}{K_{Ic}}\right)^2 + \left(\frac{K_{II}}{K_{IIc}}\right)^2 \tag{9}$$

It has been recognized that $G_{IIc}$ is normally much higher than $G_{Ic}$ due to the difference of failure mechanism (Li, 1991). For example, $G_{IIc} > 10^2 G_{Ic}$ for rocks.

After the critical stress that initiates the fracture propagation is calculated, it is applied to a similar system where only deformations are considered. Deformation calculations are computed using the code Poly3D (Thomas, 1993). In this way, the maximum possible shear displacements are evaluated.

This process is repeated for different loading scenarios and for different fracture sizes, since propagation depends upon both of these factors. It is then possible to express the propagation initiation loading stress as a function of the fracture radius.

### 1.2.3 Fracture Interactions or "Shielding"

A discrete fracture network consists of fractures distributed within a volume of rock. Their size, orientation, frequency and mechanical characteristics influence the overall mechanical characteristics of the rock mass. Since fractures may deform and propagate when subjected to an earthquake, it is reasonable to assume that the mechanical behavior of the fractures affects each other. In the particular case of the fractures located between an earthquake source and a fracture intersecting a deposition hole, it is relevant to evaluate how much of the elastic strain energy these fractures will consume and reduce the slippage or propagation of the canister fracture. Since the mechanical behavior of a complete fracture network is complicated, the problem is reduced to the case of two penny-shaped fractures with the same orientation. The study will only handle propagation issues. The influence of one fracture over the other is studied. This influence is expressed as an increase or a reduction of the risk for propagation. The risk for propagation is related to the propagation criterion $F$ presented in Equation (9).

The calculation of the $F$ factor is based on the computation of the maximum stress intensity factors at the tip of the two fractures in modes I and II. These factors are computed by the code Franc3D. The two fractures are designed as the reference fracture and the perturbation fracture. The influence of perturbation fracture on the reference fracture is studied in two cases. In the first case, the variation of the $F$ factor of the reference fracture is studied when the distance between the two fractures varies. In the second case, the effect of the change of the size of the perturbation fracture on the $F$ factor of the reference fracture is studied.

The external boundaries of the Franc3D model form a cubic block which size is chosen so that the boundary effects are negligible. Two penny-shaped fractures are located in the block. The fracture surfaces constitute internal boundaries. The fractures are dipping $45^{o}$. The reference fracture has a radius of 1 m and is located in the center of the model.

The disturbance fracture radius is also set to 1 m. Several distances between the fractures are considered. The distance between the fractures is defined as the distance between the fracture centroids along the normal of the reference fracture, see Figure 1-5a. Variation of the distance between the reference and the disturbance fractures. The distances considered are 1, 2, 4, and 10m.

In the previous case, the minimum distance of influence $D_{min}$ of the perturbation between the two fractures is estimated. If the distance is larger than $D_{min}$ then the influence is assumed negligible. The perturbation fracture is located at a distance $D_{min}$ from the reference fracture. The effect of the radius change of the disturbance fracture on the propagation criterion $F$ of the reference fracture is studied. The different radii are 1, 2 and 4m. The geometry of the system is presented in Figure 1-5b.

The material properties are the same as for Task 2.1, see section 3.1.1.

The displacements of the base of the model are set to 0 in the x, y, and z directions. A vertical normal compressive load is applied to the top of the model. The magnitude of the load, $\sigma_n$=2 MPa, was chosen so the reaction of the model was noticeable.

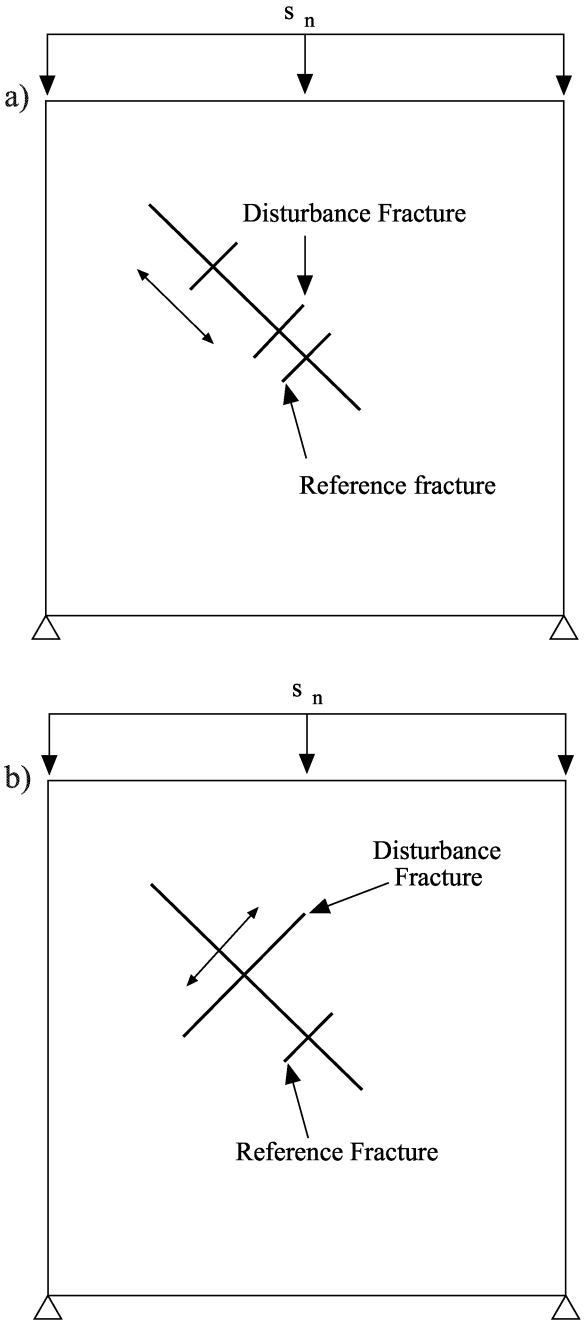


*Figure 1-5 Numerical setup for fracture propagation simulations: a) distance variations and b) radius variations*

### 1.2.4 Cohesion and Friction

The methodology employed in TR 97-07 and TR 99-03 assumed that fractures are frictionless and cohesionless. As detailed in Appendix C of TR 97-07, fractures often have cohesion and friction properties that relate to fracture size. For example, Pusch (1996) reports that fractures in the size range of 10 m to 100 m in crystalline rocks

typically have friction angles in the range of 20° to 30°, and cohesion values from 0.01 MPa to 1.0 MPa. This implies that the tractions produced on the fracture by an earthquake may not lead to slip unless the shear tractions overcome the surface friction and cohesion. In the numerical simulations reported in TR 99-03 and TR 97-07, *all* tractions produced slip, making the resulting estimates conservative.

A commonly used criterion to evaluate whether a fracture will slip is the Mohr-Coulomb criterion (Coulomb, 1773; Mohr, 1900):

$$\tau = S_o + \sigma \tan\phi \tag{10}$$

where

– $\tau$ = the shear stress on a plane

– $\sigma$ = the normal stress on a plane

– $S_o$ = the cohesion and

– $\phi$ = the friction angle.

According to this criterion, slip can occur if the shear stress on a fracture plane exceeds the stresses related to cohesion and friction that resist shear movement.

While it is not possible to directly include friction and cohesion in the Poly3D calculations, Poly3D can calculate displacements and the tractions parallel and perpendicular to fractures, but not both at the same time. The simulations reported in TR 99-03 assumed a shear stress boundary condition parallel to the fracture surfaces in order to compute the shear displacements parallel to the fracture plane. Thus the shear stresses that would have developed if sliding had been prohibited were not calculated. These stresses can be calculated by assigning 0.0 displacement boundary conditions in the plane of the fracture.

In order to calculate the shear and normal tractions on the fractures, 650 realizations for the Aberg site were re-run with boundary conditions on the fractures set to 0.0 shear displacement. These 650 realizations represent the entire range in earthquake magnitudes and distances used in the calculations reported in TR 99-03. Earthquake magnitudes varied from $M_L$ 2.0 to $M_L$ 8.5, and distances from the repository from a few meters up to 100 km.

Once the tractions were computed for these realizations, they were evaluated using the Mohr-Coulomb criterion. Three sets of cohesion and friction parameters were used to represent the range of possible values for fractures in the size range of 10 m to 100 m. These three sets were:

**Table 1-4. Mohr-Coulomb parameters for friction and cohesion simulations**

| Parameter Set | Cohesion (MPa) | Friction Angle |
|---|---|---|
| 1 | 0.01 | 20° |
| 2 | 0.1 | 25° |
| 3 | 1.0 | 30° |

Parameter Set #1 corresponds to the weakest and lowest friction case, while Parameter Set #3 corresponds to the strongest and highest friction case. Failures should be lowest for Parameter Set #3, intermediate with Parameter Set #2 and highest with Parameter Set #1.

If the tractions on a fracture are such that they exceed the Mohr-Coulomb criterion, then the fracture is allowed to slip the entire amount that was predicted in TR 99-03. If the Mohr-Coulomb criterion was not exceeded, the fracture was given 0.0 m slip, regardless of the amount predicted in TR 99-03. Of particular interest are the fractures whose calculated slip in TR 99-03 exceeded the displacement threshold of 0.1 m. A key question is whether the inclusion of fracture cohesion and friction would have significantly reduced the number of failed canisters.

Fracture size, earthquake magnitude and the distance of the earthquake from the fractures intersecting the canisters can also impact induced fracture displacements. Since induced displacement and tractions on a fracture are a function of fracture radius, it is conceivable that large fractures may be more affected by including slip and cohesion than small fractures, or perhaps small fractures would be differentially impacted. Also, large, close earthquakes produce greater tractions and displacements. The inclusion of friction and cohesion might reduce the impact of earthquakes that are far away or are of smaller magnitudes. On the other hand, large nearby earthquakes may produce such large tractions that they always exceed the Mohr-Coulomb criterion. For these reasons, the effects of earthquake magnitude, separation distance between the earthquake rupture centroid and the fractures, and fracture radius were also studied.

# 2 SENSITIVITY ANALYSIS RESULTS

## 2.1 Task 1.1 – Modeling Results

The result of a single run of Poly3D is the induced slip on a target fracture due to the elastic field generated by a dislocation (earthquake). Over 50,000 runs were performed in order to quantify the sensitivity of the induced slip on the parameters in Table 1-2. Induced slips greater than 10 cm (0.1 m) are the most critical, as these would cause canister failure. Induced slips greater than 1 cm are also noted. Because induced slips vary over approximately 12 orders of magnitude, all figures show the logarithmic (Base 10) values of induced slip.

Results are shown as two types of line diagrams and three types of contour plots. The contour plots require some further explanation:

1. Contour plots of induced slip (Figure 2-3 through 2-6) against the variables of log distance and earthquake magnitude are used to derive empirical relations between these parameters and induced slip.

2. A geographic map view (Figures 2-7 through 2-11) shows log contours of the induced slip caused by earthquakes of a certain magnitude with the near tip at grid points on the map. Each map is valid only for a certain combination of target fracture orientation and size, and earthquake magnitude and rupture orientation. The irregular shapes of the contours confirm the difficulty of fitting simple equations to predict induced slip as a function of magnitude, orientation and size.

3. In order to assess the importance of target fracture orientation for a constant earthquake, the trend and plunge of the fracture pole are plotted and the induced slip contoured (Figure 2-14). This diagram was created for five different azimuths.

Section 2.1.1 presents the results from the initial numerical simulations in which all of the parameters were varied according to the values in Table 1-2. Section 2.1.2 focuses on the relation between fracture radius and induced slip for the situation when all other parameters are held constant. This relation is required for the calculations carried out in Task 1.2 (Section 2.2). Section 2.1.3 provides a more detailed analysis of the impact of the relative orientation of the fault and the target fracture using the parameter ranges shown in Table 1.2 for the detailed simulations. The results from these more comprehensive simulations are used to identify the worst-case scenario of relative orientation, which is also used to carry out the calculations in Task 1.2.

### 2.1.1 Preliminary simulations

Preliminary simulations were run by simultaneously varying all five parameters. Seven magnitudes, eleven radial distances, four target fracture sizes, five azimuths in the first quadrant, and seven target fracture orientations resulted in 10,780 runs. This scenario was run for both strike-slip and reverse movement. Of the 10,780 strike-slip simulations, 2586 had slips greater than 1 cm, and 1279 greater than 10 cm.

Figure 2-1 shows the primary importance of earthquake magnitude and radial distance to the tip. In the upper left half of the figure, no combination of azimuth to the earthquake, target fracture size, or orientation caused induced slips greater than 10 cm. However, below and to the right of the line in the diagram, 31% of the simulated earthquakes caused 10-cm slips. The equation of the line separating damaging slips from non-damaging slips can be used to make the following statement:

*If 0.85 M – 2.6 < log(distance) then there is a chance of a damaging earthquake*

The position of the target fracture centroid relative to the fault tip on which the earthquake occurs impacts the induced slip, as shown in Figure 1-3. This figure shows that the maximum shear stress varies with relative location about a fracture displacing in Mode II shear. The magnitude of shear depends upon the distance from the fracture centroid to the earthquake rupture tip, and the angle or azimuth between them. At a radius of 40% of the rupture length, shear stress goes from less than 1.0 perpendicular to the fracture at the fracture centerline (up, or an azimuth of $0^{\circ}$) to a value near 1.75 parallel to the fracture centerline (right, or an azimuth of $90^{\circ}$).

Figure 2-2 summarizes the importance of the other parameters on induced slip.

Figure 2-2a shows the large and direct effect that fracture size has on induced slips. Very large (1000 m radius) target fractures are much more likely to have large slips. Figure 2-2b shows that although the effect is small, target fractures offset from the strike of the earthquake rupture (azimuth=67.5°) will be more likely (12.4%) to experience the large induced slips, while target fractures at an azimuth parallel (0°) to the rupture will be least likely (9.0%). For comparison, overall 12% (1279 out of 10780) of the simulations caused 10 cm or greater induced slip. Another parameter with a small effect is the orientation of the target fracture (Figure 2-2c). Horizontal fractures are the least likely to experience induced slip greater than 10 cm and west dipping fractures (pole = 090/45) are most likely. However, the overall difference between the worst (15% with >1 cm slip) and best (4% with >1 cm slip) is less than a factor of four.

Another way to plot the results of the preliminary runs is to contour the log values of induced slip as a function of distance and magnitude as shown in Figures 2-3 through 2-6. In Figure 2-3 the results for a single combination of orientation (fracture pole = 000/00), azimuth (0º), and size (r=1000 m) are shown. However, this plot is not as useful as contouring the *maximum* induced slip for all combinations of orientation and azimuth (Figure 2-4). For any each magnitude and distance combination, the largest induced slips may occur at a different azimuth, and target fracture orientation (Table 2-1). For example, at a magnitude distance combination of 7.5 and 3.2 km the maximum induced slip (17 cm) occurs on a fracture with a pole trend of 045/45 at an azimuth of 45°. Meanwhile at a magnitude distance combination of 7.0 and 1 km the maximum induced slip (21 cm) occurs on a fracture with a pole trend of 000/00 at an azimuth of 90°. This phenomenon is due to the irregular shape of the shear stress contours (Figure 1-3) and 3D effects caused by the target fracture depth (500 m) which is offset from the earthquake rupture center depth (1 to 12 km, for magnitude 4.0 to 8.0, respectively, Table 2-1).

**Table 2-1. Characteristics of earthquake producing the maximum slip for each distance/magnitude combination**

| Run# | Maximum Induced Slip | Pole Trend | Pole Plunge | Azimuth | Distance | log(Distance) | Mag |
|---|---|---|---|---|---|---|---|
| T_1804 | 1.45E-09 | 90 or 0 | 0 | 45 | 100000 | 5 | 4 |
| T_8292 | 8.12E-09 | 90 or 0 | 0 | 45 | 56234 | 4.75 | 4 |
| T_8264 | 4.50E-08 | 90 or 0 | 0 | 45 | 31623 | 4.5 | 4 |
| T_1808 | 8.72E-08 | 90 or 0 | 0 | 45 | 100000 | 5 | 5 |
| T_8296 | 4.75E-07 | 90 | 0 | 45 | 56234 | 4.75 | 5 |
| T_1784 | 1.31E-06 | 90 | 0 | 45 | 10000 | 4 | 4 |
| T_9948 | 2.52E-06 | 90 | 45 | 45 | 31623 | 4.5 | 5 |
| T_3912 | 4.74E-06 | 90 | 45 | 45 | 100000 | 5 | 6 |
| T_9916 | 6.80E-06 | 90 | 45 | 45 | 5623 | 3.75 | 4 |
| T_9980 | 2.43E-05 | 90 | 45 | 45 | 56234 | 4.75 | 6 |
| T_9888 | 3.10E-05 | 90 | 45 | 45 | 3162 | 3.5 | 4 |
| T_5848 | 3.28E-05 | 0 | 45 | 22.5 | 100000 | 5 | 6.5 |
| T_3888 | 6.17E-05 | 90 | 45 | 45 | 10000 | 4 | 5 |
| T_9952 | 1.13E-04 | 90 | 45 | 45 | 31623 | 4.5 | 6 |
| T_8752 | 1.53E-04 | 0 | 45 | 22.5 | 56234 | 4.75 | 6.5 |
| T_2376 | 2.07E-04 | 0 | 45 | 22.5 | 100000 | 5 | 7 |
| T_9920 | 2.36E-04 | 90 | 45 | 45 | 5623 | 3.75 | 5 |
| T_224 | 3.02E-04 | 0 | 0 | 22.5 | 1000 | 3 | 4 |
| T_9956 | 5.89E-04 | 90 | 45 | 45 | 31623 | 4.5 | 6.5 |
| T_9780 | 7.41E-04 | 90 | 45 | 22.5 | 3162 | 3.5 | 5 |
| T_8648 | 7.72E-04 | 0 | 45 | 0 | 56234 | 4.75 | 7 |
| T_5796 | 1.03E-03 | 0 | 45 | 0 | 100000 | 5 | 7.5 |
| T_624 | 1.37E-03 | 0 | 0 | 90 | 316 | 2.5 | 4 |
| T_3752 | 1.55E-03 | 90 | 45 | 22.5 | 10000 | 4 | 6 |
| T_9852 | 2.72E-03 | 90 | 45 | 22.5 | 31623 | 4.5 | 7 |
| T_3728 | 3.39E-03 | 90 | 45 | 22.5 | 1000 | 3 | 5 |
| T_9876 | 3.45E-03 | 90 | 45 | 22.5 | 56234 | 4.75 | 7.5 |
| T_9812 | 3.92E-03 | 90 | 45 | 22.5 | 5623 | 3.75 | 6 |
| T_3780 | 4.27E-03 | 90 | 45 | 22.5 | 100000 | 5 | 8 |
| T_6400 | 5.64E-03 | 90 | 45 | 22.5 | 10000 | 4 | 6.5 |
| T_604 | 5.90E-03 | 0 | 0 | 90 | 100 | 2 | 4 |
| T_9784 | 7.66E-03 | 90 | 45 | 22.5 | 3162 | 3.5 | 6 |
| T_9848 | 0.0104 | 90 | 45 | 22.5 | 31623 | 4.5 | 7.5 |
| T_9816 | 0.0115 | 90 | 45 | 22.5 | 5623 | 3.75 | 6.5 |
| T_628 | 0.0132 | 0 | 0 | 90 | 316 | 2.5 | 5 |
| T_9884 | 0.0133 | 90 | 45 | 22.5 | 56234 | 4.75 | 8 |
| T_3756 | 0.0173 | 90 | 45 | 22.5 | 10000 | 4 | 7 |
| T_1984 | 0.0208 | 90 or 0 | 0 | 90 | 32 | 1.5 | 4 |
| T_9340 | 0.0208 | 45 | 45 | 45 | 3162 | 3.5 | 6.5 |
| T_652 | 0.0257 | 0 | 0 | 90 | 1000 | 3 | 6 |
| T_9824 | 0.0318 | 90 | 45 | 22.5 | 5623 | 3.75 | 7 |
| T_9856 | 0.0356 | 90 | 45 | 22.5 | 31623 | 4.5 | 8 |
| T_6404 | 0.0493 | 90 | 45 | 22.5 | 10000 | 4 | 7.5 |
| T_9348 | 0.0600 | 45 | 45 | 45 | 3162 | 3.5 | 7 |
| T_1964 | 0.0680 | 90 or 0 | 0 | 90 | 10 | 1 | 4 |
| T_5160 | 0.0750 | 0 | 0 | 90 | 1000 | 3 | 6.5 |
| T_9372 | 0.0919 | 45 | 45 | 45 | 5623 | 3.75 | 7.5 |
| T_632 | 0.1095 | 0 | 0 | 90 | 316 | 2.5 | 6 |
| T_4320 | 0.1398 | 0 | 90 | 0 | 10000 | 4 | 8 |
| T_1988 | 0.1687 | 90 or 0 | 0 | 90 | 32 | 1.5 | 5 |
| T_9344 | 0.1709 | 45 | 45 | 45 | 3162 | 3.5 | 7.5 |

| Run# | Maximum Induced Slip | Pole Trend | Pole Plunge | Azimuth | Distance | log(Distance) | Mag |
|---|---|---|---|---|---|---|---|
| T_656 | 0.2160 | 0 | 0 | 90 | 1000 | 3 | 7 |
| T_9380 | 0.2634 | 45 | 45 | 45 | 5623 | 3.75 | 8 |
| T_5152 | 0.3114 | 0 | 0 | 90 | 316 | 2.5 | 6.5 |
| T_612 | 0.4028 | 0 | 0 | 90 | 100 | 2 | 6 |
| T_9352 | 0.4834 | 45 | 45 | 45 | 3162 | 3.5 | 8 |
| T_1968 | 0.5441 | 90 or 0 | 0 | 90 | 10 | 1 | 5 |
| T_5164 | 0.6175 | 0 | 0 | 90 | 1000 | 3 | 7.5 |
| T_636 | 0.8824 | 0 | 0 | 90 | 316 | 2.5 | 7 |
| T_5704 | 1.138 | 90 or 0 | 0 | 90 | 100 | 2 | 6.5 |
| T_1992 | 1.345 | 90 or 0 | 0 | 90 | 32 | 1.5 | 6 |
| T_660 | 1.757 | 0 | 0 | 90 | 1000 | 3 | 8 |
| T_5156 | 2.496 | 0 | 0 | 90 | 316 | 2.5 | 7.5 |
| T_616 | 3.213 | 0 | 0 | 90 | 100 | 2 | 7 |
| T_5696 | 3.794 | 90 or 0 | 0 | 90 | 32 | 1.5 | 6.5 |
| T_1972 | 4.325 | 90 or 0 | 0 | 90 | 10 | 1 | 6 |
| T_640 | 7.050 | 0 | 0 | 90 | 316 | 2.5 | 8 |
| T_5148 | 9.065 | 0 | 0 | 90 | 100 | 2 | 7.5 |
| T_1996 | 10.700 | 90 or 0 | 0 | 90 | 32 | 1.5 | 7 |
| T_5688 | 12.190 | 90 or 0 | 0 | 90 | 10 | 1 | 6.5 |
| T_620 | 25.560 | 0 | 0 | 90 | 100 | 2 | 8 |
| T_5700 | 30.170 | 90 or 0 | 0 | 90 | 32 | 1.5 | 7.5 |
| T_1976 | 34.380 | 90 or 0 | 0 | 90 | 10 | 1 | 7 |
| T_2000 | 85.030 | 90 or 0 | 0 | 90 | 32 | 1.5 | 8 |
| T_5692 | 96.920 | 90 or 0 | 0 | 90 | 10 | 1 | 7.5 |
| T_1980 | 273.100 | 90 or 0 | 0 | 90 | 10 | 1 | 8 |

Fitting a plane to the contours above an induced slip of $10^{-2}$ m in Figure 2-4 gives;

$$\text{Log(max. slip)} = 0.9*M - 1.1*\text{Log(distance)} - 3.6 \quad (11)$$

This equation can be recast in terms of earthquake slip rather than magnitude by substituting in Equation (2):

$$\text{Log(max. slip)} = \text{Log(earthquake slip)} - 1.1*\text{Log(distance)} + 2.7 \quad (12)$$

Figure 2-4 is plotted for strike-slip movement; Figure 2-5 is for reverse (vertical) earthquake slip. The fit to the plane in Figure 2-5 is nearly the same as Equation (11):

$$\text{Log(induced slip)} = 0.9*M - 1.1*\text{Log(distance)} - 3.8 \quad (13)$$

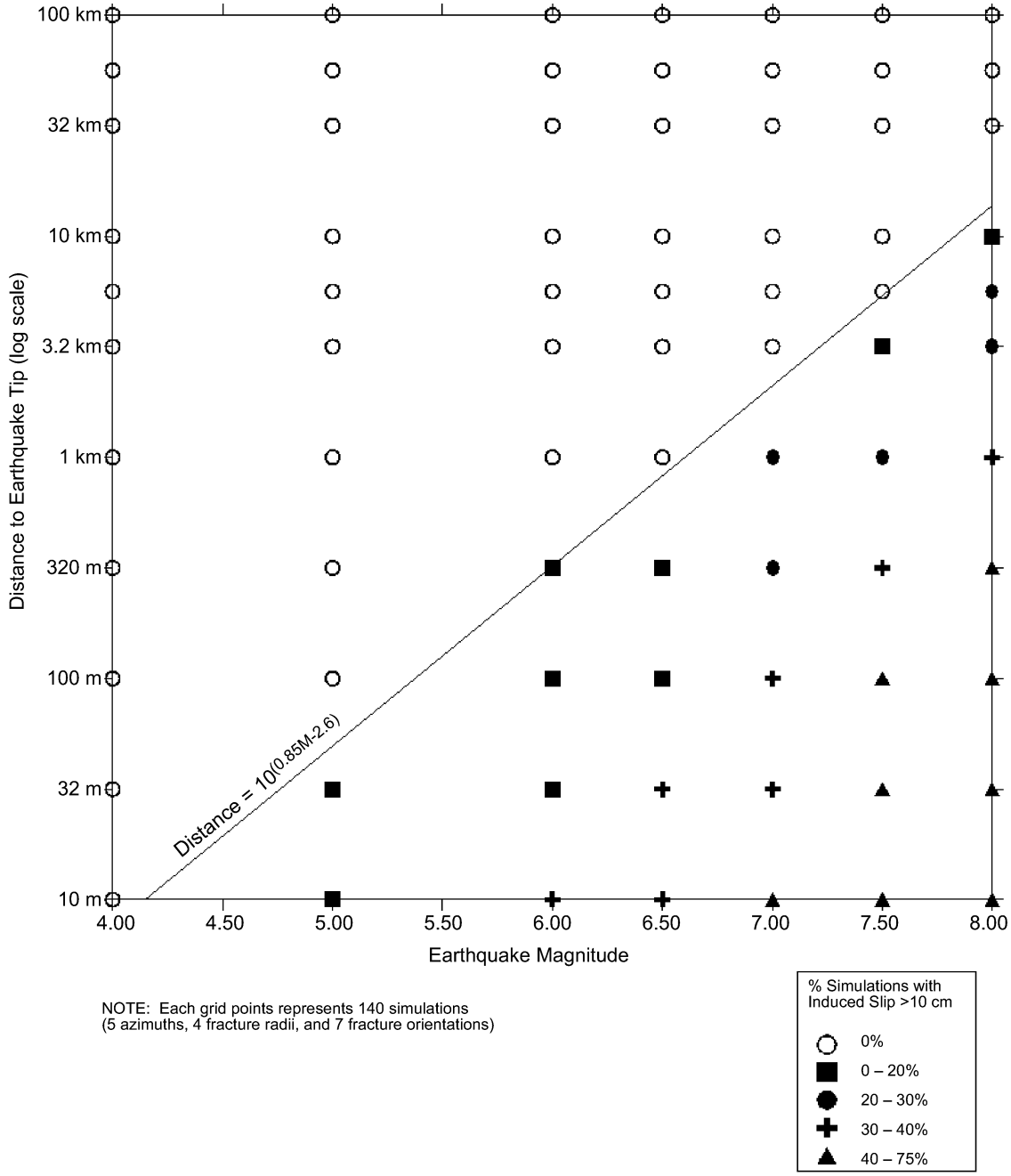


*Figure 2-1 Percent earthquakes causing induced slips greater than 10 cm as a function of earthquake magnitude and distance*

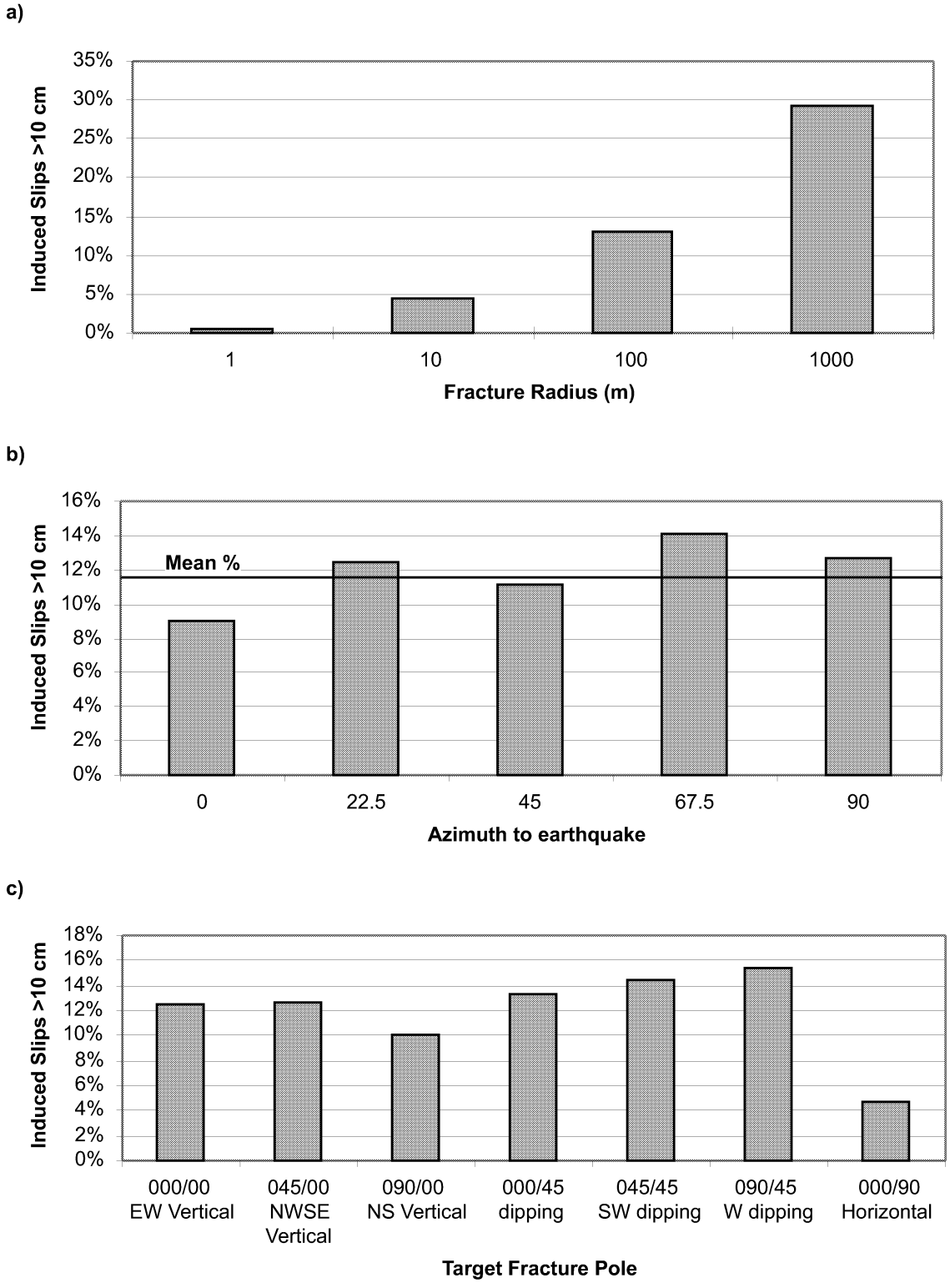


*Figure 2-2 Effect of azimuth and target fracture size and orientation on induced slip*

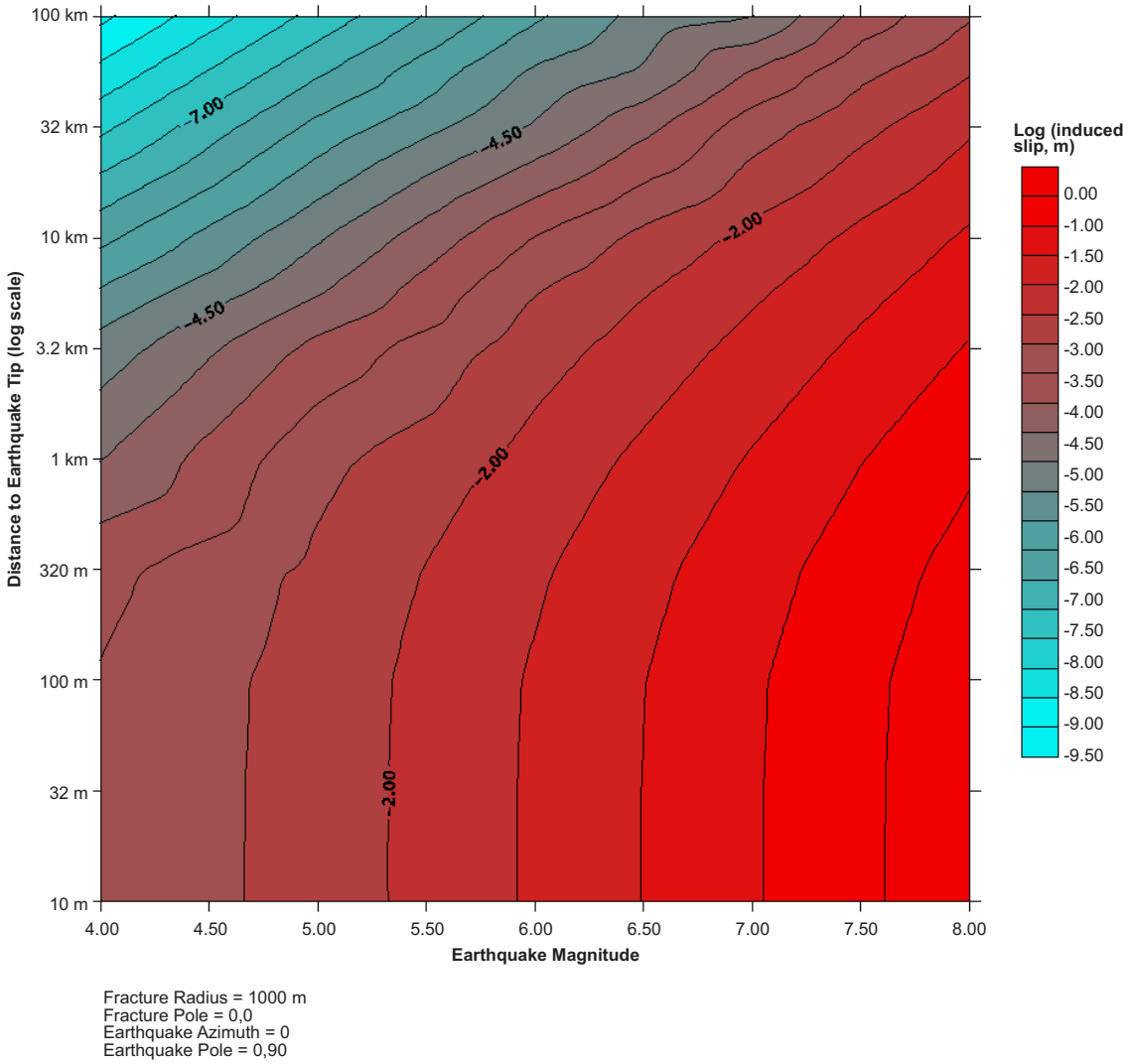


*Figure 2-3 Induced slip as a function of magnitude and distance for single geometry*

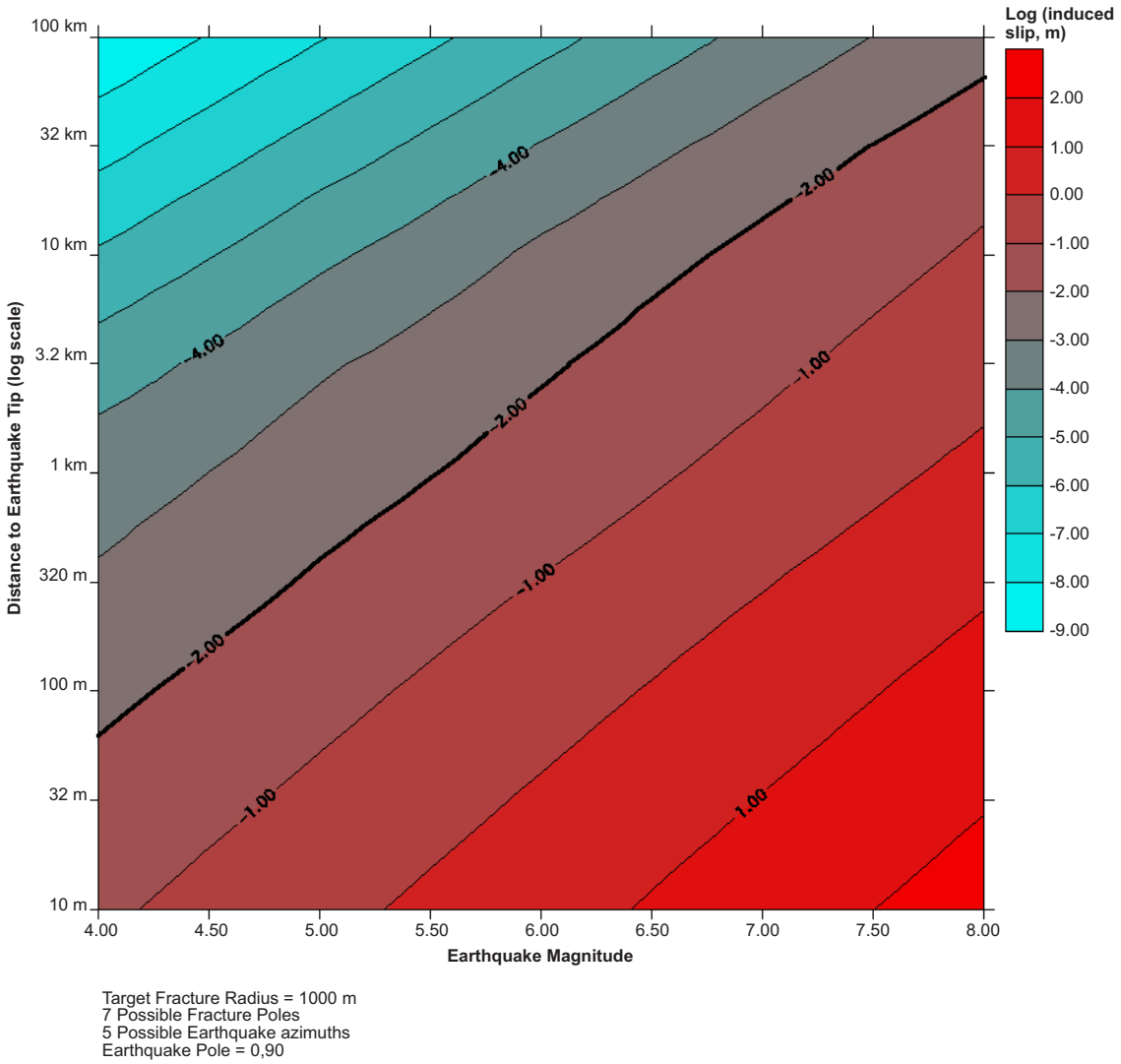


*Figure 2-4 Maximum induced slip as a function of magnitude and distance for strike slip*

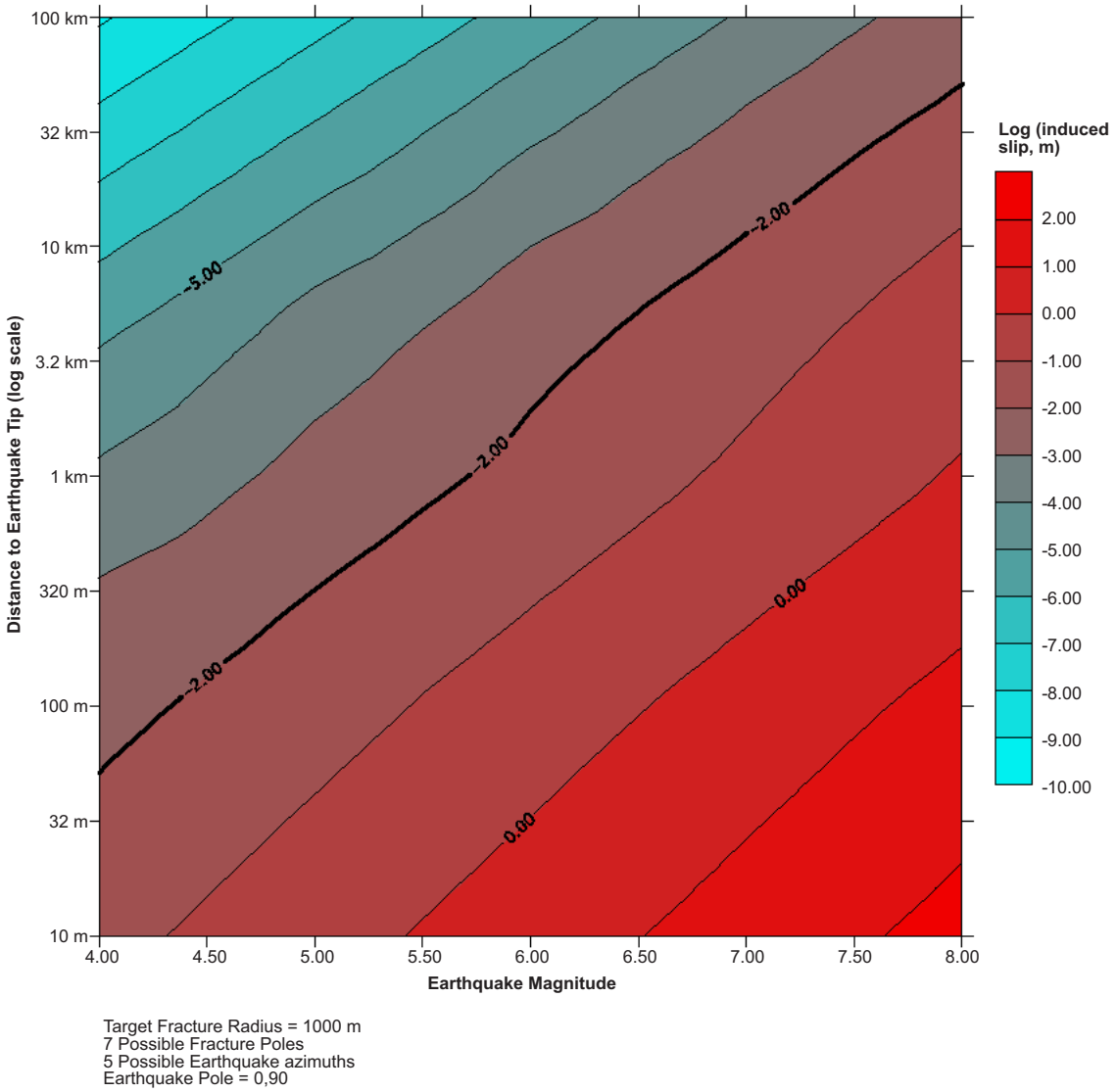


*Figure 2-5 Maximum induced slip as a function of magnitude and distance for dip slip*

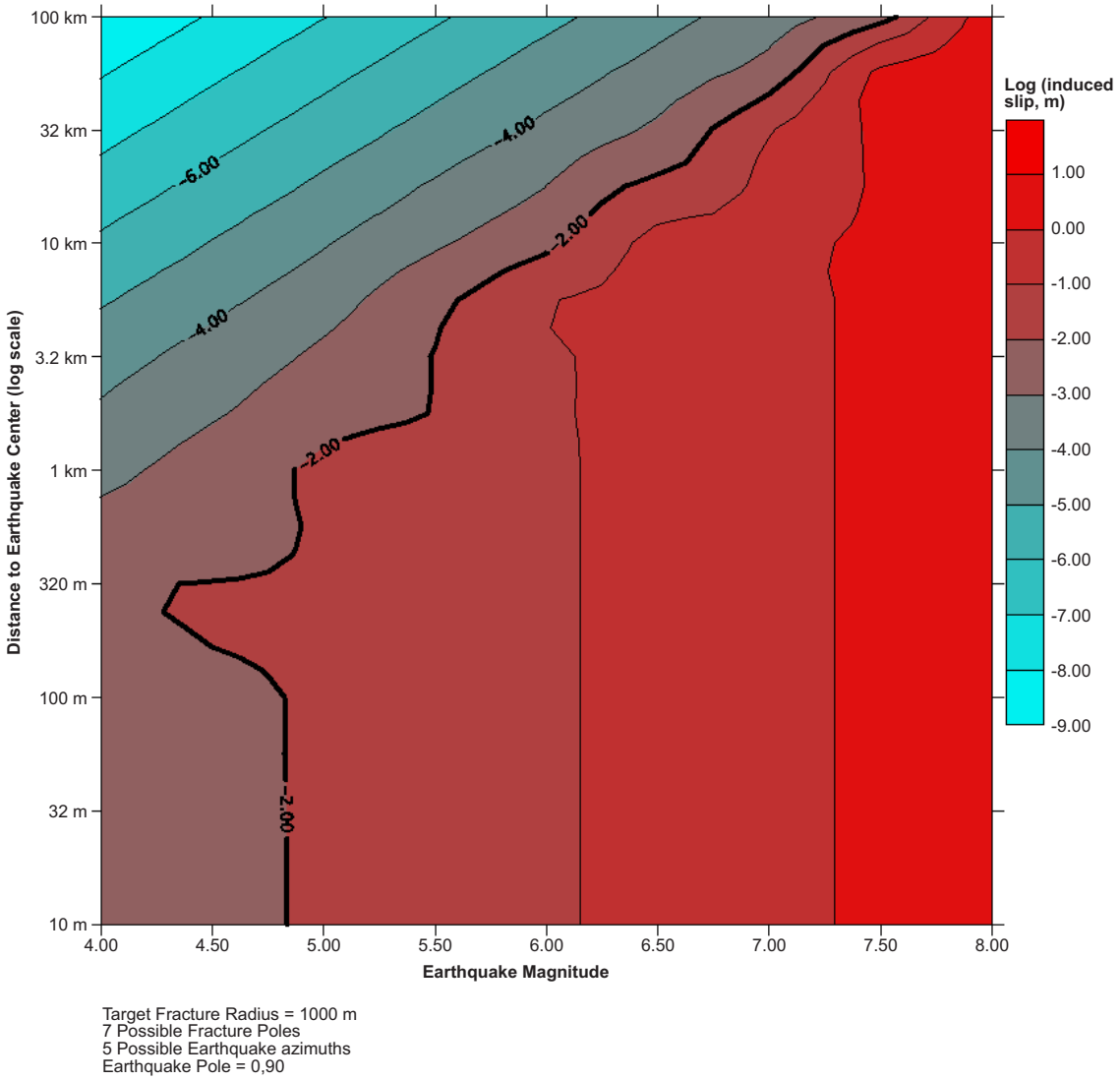


*Figure 2-6 Maximum induced slip as a function of magnitude and measured to earthquake center*

These three equations are for a target fracture radius of 1000 m. The following sections show the effect of fracture size on induced slip.

Distance in these simulations is measured to the tip of the earthquake rupture, not to the epicenter. Measuring distance to the earthquake center might make results more difficult to interpret because the tip is the locus of stress and it could be much closer than the center to the target fracture. Figure 2-6 shows a similar diagram derived when measuring to the earthquake center. Notice that unlike Figures 2-4 and 2-5, the contours cannot be fit to a plane nor can simple relations like those in Equations (11) and (13) be developed.

The preliminary simulations show that:

1. The primary controls on induced slip are earthquake magnitude and distance. Maximum induced slip is a well-behaved function of earthquake magnitude and distance to the tip of the earthquake rupture.

2. Although numerical modeling is necessary to find the induced slip on a particular orientations and azimuth combination (Table 2-1), the maximum induced slip for a given combination of magnitude and distance can be determined by Equations (11), (12), and (13).
3. The distance to the earthquake rupture tip rather than center makes for a simpler relationship.

In order to further determine the sensitivity of induced slip predictions to earthquake location (distance and azimuth), further Poly3D simulations were run varying earthquake distance and azimuth while holding magnitude, and earthquake and target fracture orientation constant (Table 1-2). These simulations are summarized as maps with the target fracture at the center (0,0) and contours of induced slip caused by earthquakes with tips at the geographic map positions. The crosses on Figures 2-7 through 2-11 show the location of the simulation results that fored the basis for the contour plots. The graphs were created for magnitude 7.0 earthquake for strike-slip movement on parallel earthquake rupture and target fracture (Figure 2-7), strike-slip movement perpendicular earthquake rupture and target fracture (Figure 2-8), and vertical movement on parallel earthquake rupture and target fracture (Figure 2-9).

As the stress field near a Mode II fracture (Figure 1-3) suggests, the induced slip contours show some dependence upon the azimuth or relative position between the target fracture and the fault. Figures 2-7 through 2-9 illustrate the impact of location, the relative angular orientation between the fault and the target fracture, and the type of slip. For example, Figure 2-7 shows the results of varying the azimuth for the case where the fault and the target fracture are parallel. The two plots in this figure show the magnitude of induced slip as a function of distance and azimuth. This figure shows that for a given distance, fractures that are located with azimuths of $45^{\circ}$, $90^{\circ}$, $135^{\circ}$, $225^{\circ}$, $270^{\circ}$, and $315^{\circ}$ relative to the fault have the greatest displacements. Figures 2-8 and 2-9 are similar in that they show results for the case where the fault and the target fracture are perpendicular. Figure 2-8 shows results for strike-slip motion, while Figure 2-9 shows results for a reverse fault type of displacement.

Figures 2-7 through 2-9 are for a particular earthquake magnitude. However, these maps are still useful for estimating the slips caused by larger or smaller earthquakes, because changing the earthquake magnitude linearly changes the induced slip but the overall shape of the contours do not significantly change (i.e. Figure 2-10).

In previous reports (TR-99-03), distance was measured to the epicenter of the earthquake. For earthquake ruptures located on specific lineaments, as was performed in TR-99-03, this is a logical measurement. However, if the earthquake rupture is allowed to trend towards the repository from its center, significant irregularities can occur. This is shown in Figure 2-11. In this set of simulations, a NS earthquake rupture has a very long influence in the north and south of the repository simply because the tip of the rupture can be within the repository even though the center is far away.

### 2.1.2 Target Fracture Size

The relation between fracture radius and induced slip, while other parameters are held constant is necessary for the estimation of canister failure in Task 1.2. Pollard and Segall (1987) have shown that induced slip should increase linearly with fracture radius, and is also a function of the elastic moduli of the rock and the applied stresses. This suggests that the induced slip, as a function of fracture radius, should have the form:

$$Slip = Size/k \quad (14)$$

where the constant $k$ is a function of the target fracture and rupture geometry.

Figure 2-12 illustrates the results from the initial simulations in which fracture radius varied from 1 m to 1000 m for strike-slip and reverse fault motions. The three curves on the two inset graphs correspond to the relative orientations between the fault and the target fracture also used in Figures 2-7 through 2-9. The values of k range from 20,000 to 250,000 depending on orientation and azimuth, for the elastic moduli assumed in the simulations. In order to derive the induced slip on a new fracture with a different radius, the induced slip is multiplied by the ratio of the radius divided by 1000 m for the 1000 m fracture of the same azimuth, orientation, magnitude, and distance. Table 2-1 gives values for the 1000 m reference fracture.

### 2.1.3 More Detailed Investigations on Induced Slip as a Function of the Relative Orientation and Location Between Faults and Target Fractures

One strategy for qualitatively comparing alternative sites, or for making preliminary estimates of canister failure risk, would be to develop a comprehensive look-up table or functional relation between the relative orientation between the fault and the target fracture, and the induced displacements. However, the preliminary results shown in Figures 2-7 through 2-9 suggest that there is no simple functional relation. A look-up table could be created from the data underlying these plots, but its utility in site comparison or canister failure estimation is limited. The limitations arise from the fact that it is only useful if the orientations of the earthquake fault and the fractures at the candidate site are well known. Since the orientation of the fault on which a future earthquake might take place is poorly constrained, and the orientation of fractures at future candidate sites may not be well-known during early site selection phases, it is more useful to determine the order of magnitude impact of relative orientation, and to identify the worst-case orientation for possible use in site comparison and failure estimation.

In this set of simulations, magnitude was set to 7.0 for a NS strike-slip rupture, and the target fracture size was set to 1000 m. First, simulations were made for a complete range of relative orientation between the target fracture and the earthquake rupture. In these simulations, seven different target fracture orientations and five azimuths between the target fracture and earthquake rupture were simulated. Figure 2-13 shows the results of the preliminary runs and the complex relationship between these two parameters.

For example, at an azimuth of 22.5°, the greatest amount of induced slip occurs on a west dipping fracture, whereas at an azimuth of 67.5°, the greatest amount of induced slip occurs on a NS, vertical fracture.

In order to further investigate the role of target fracture orientation and azimuth, and additional 245 simulations were made (49 target fracture orientations and 5 azimuths). Figure 2-14 shows contours of induced slip as a function of target fracture trend and plunge at each azimuth. Overall, the worst orientation for a target fracture to have is to make a solid angle of 45° with the rupture (Figure 2-14f). This is not surprising, since linear elasticity predicts that the maximum shear stress magnitude will occur at locations along the two planes perpendicular to the $\sigma_1,\sigma_3$ plane and making a solid angle of ±45° to the $\sigma_1,\sigma_2$ plane (Pollard and Segall, 1987).

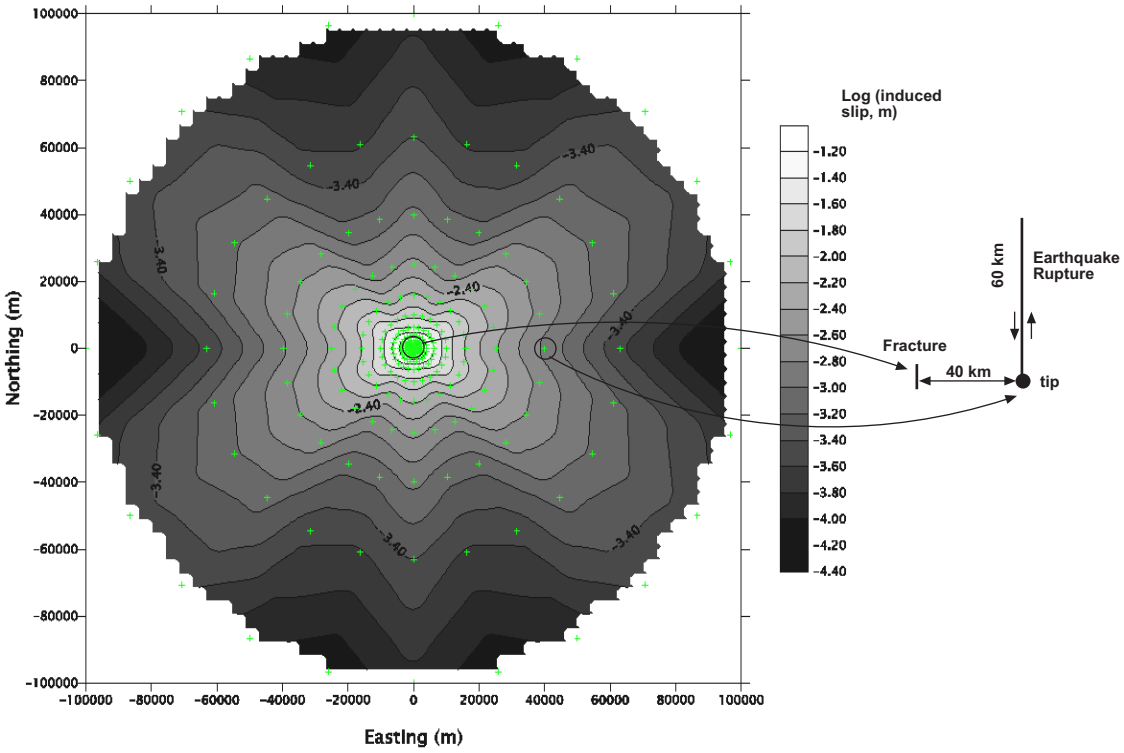


a) 100 x 100 km map (points show simulated earthquake tip locations)

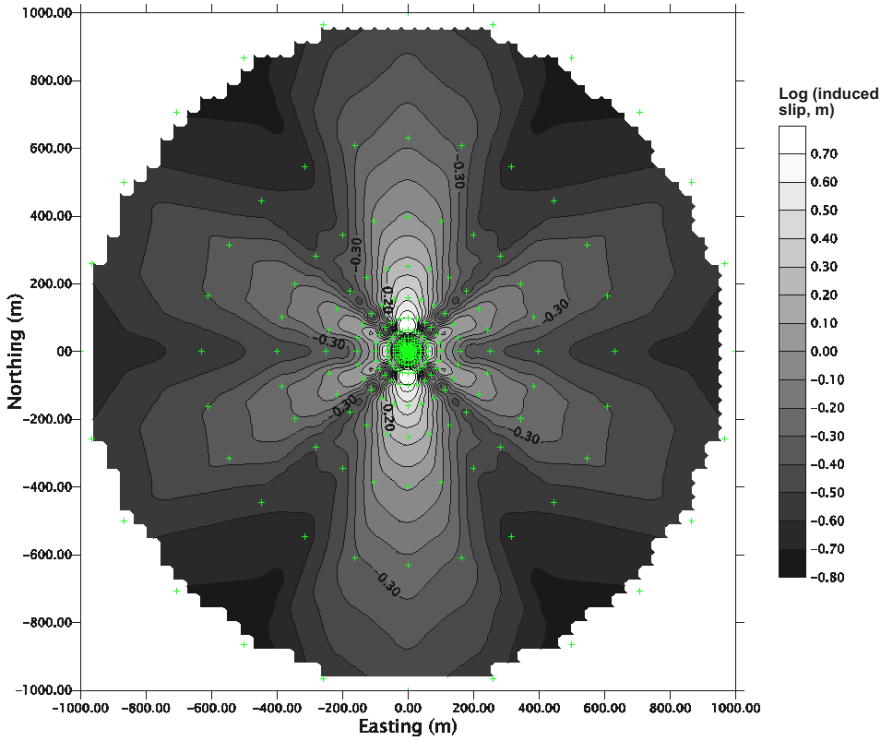


b) 1 x 1 km map

*Figure 2-7 Map view of effect of magnitude 7.0 strike-slip earthquake on parallel target fracture*

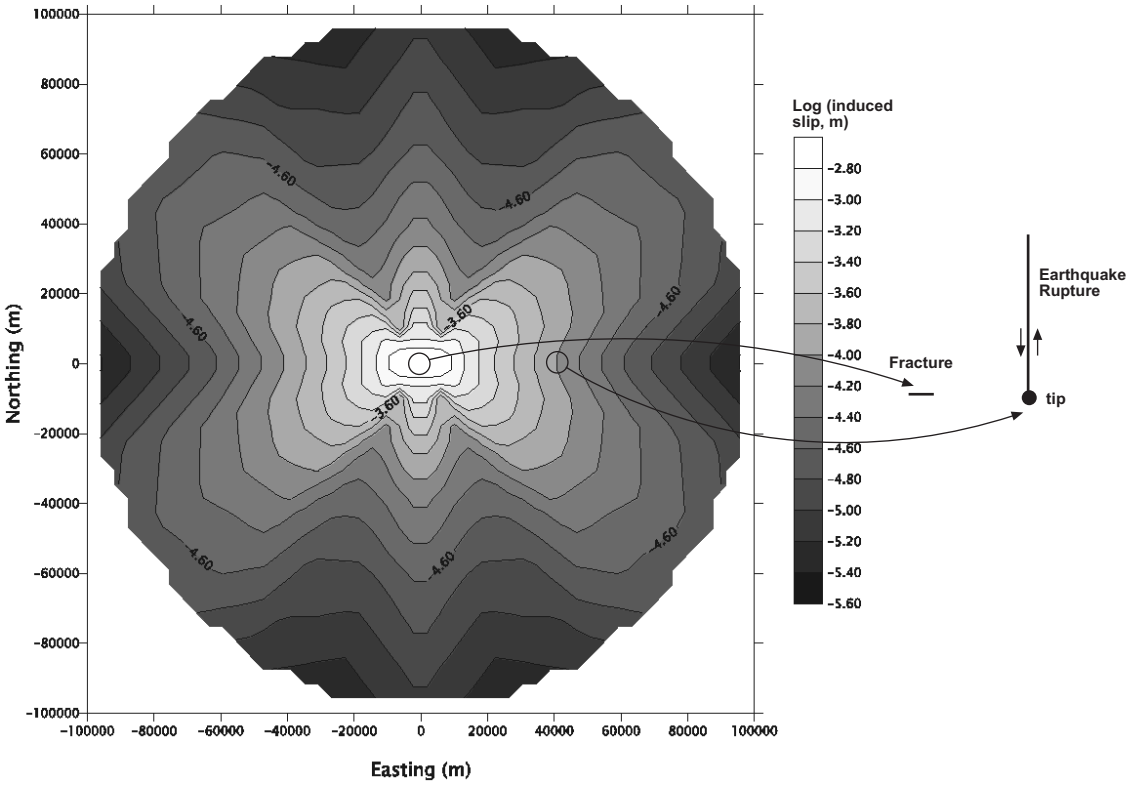


a) 100 x 100 km map

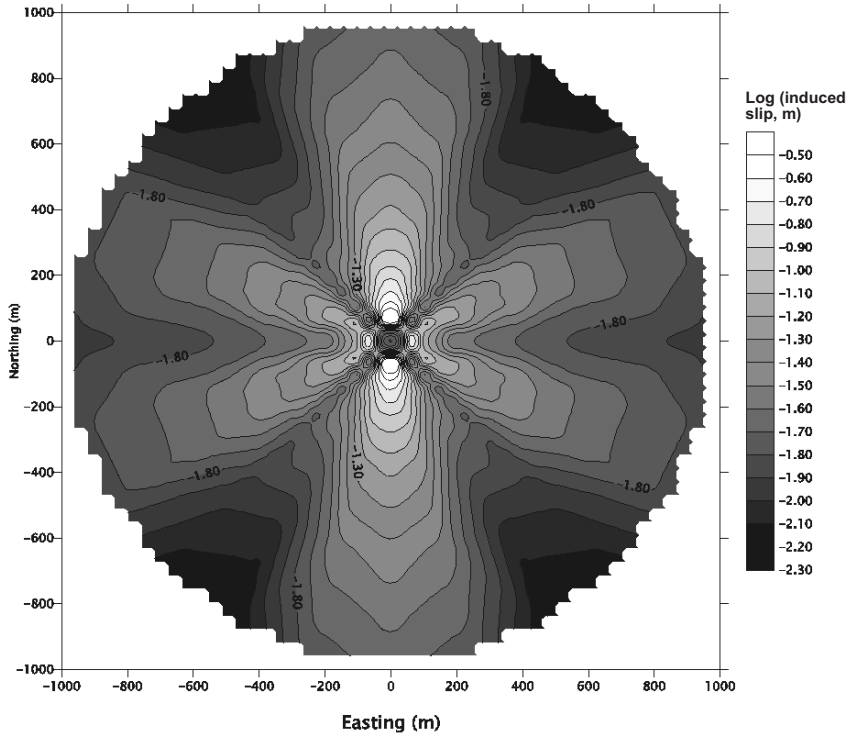


b) 1 x 1 km map

*Figure 2-8 Map view of effect of magnitude 7.0 strike-slip earthquake on perpendicular target fracture*

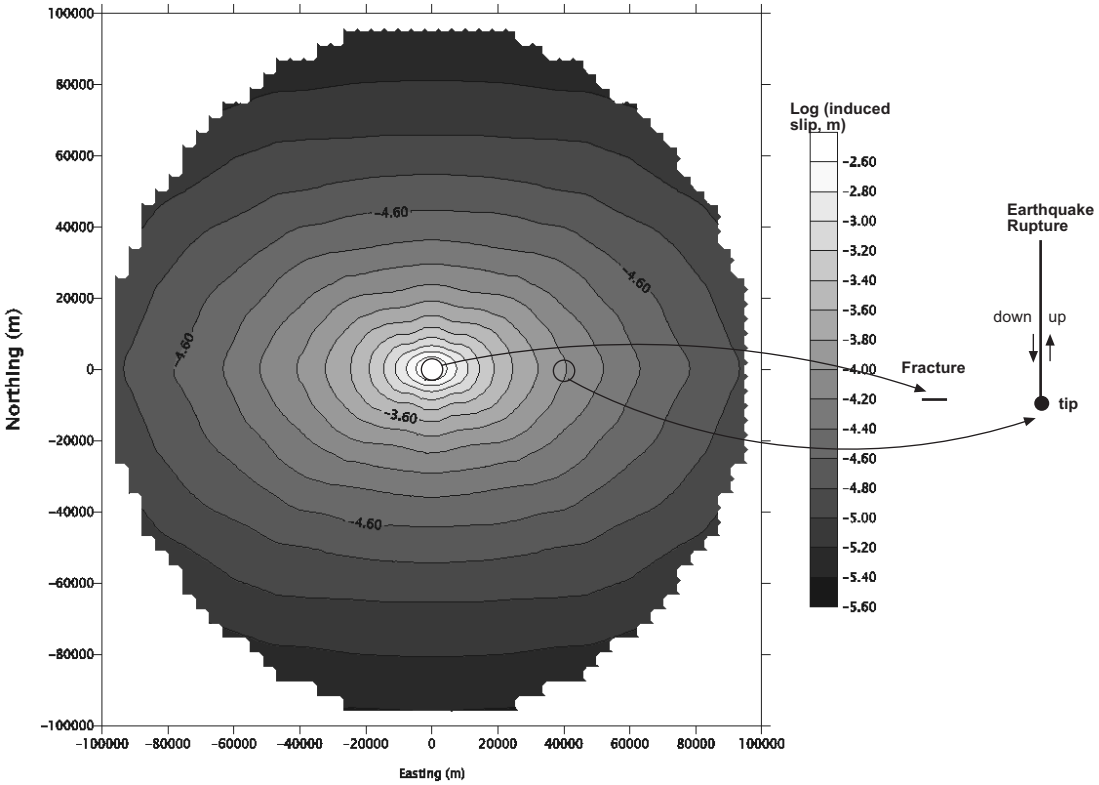


a) 100 x 100 km map

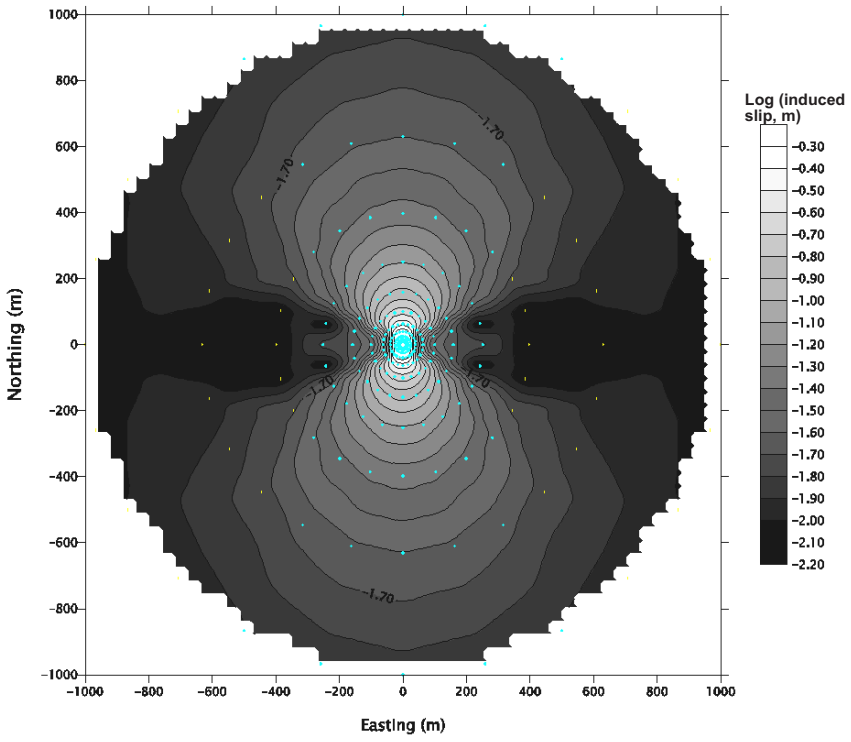


b) 1 x 1 km map (points show simulated earthquake locations)

*Figure 2-9 Map view of effect of magnitude 7.0 reverse-slip earthquake on parallel target fracture*

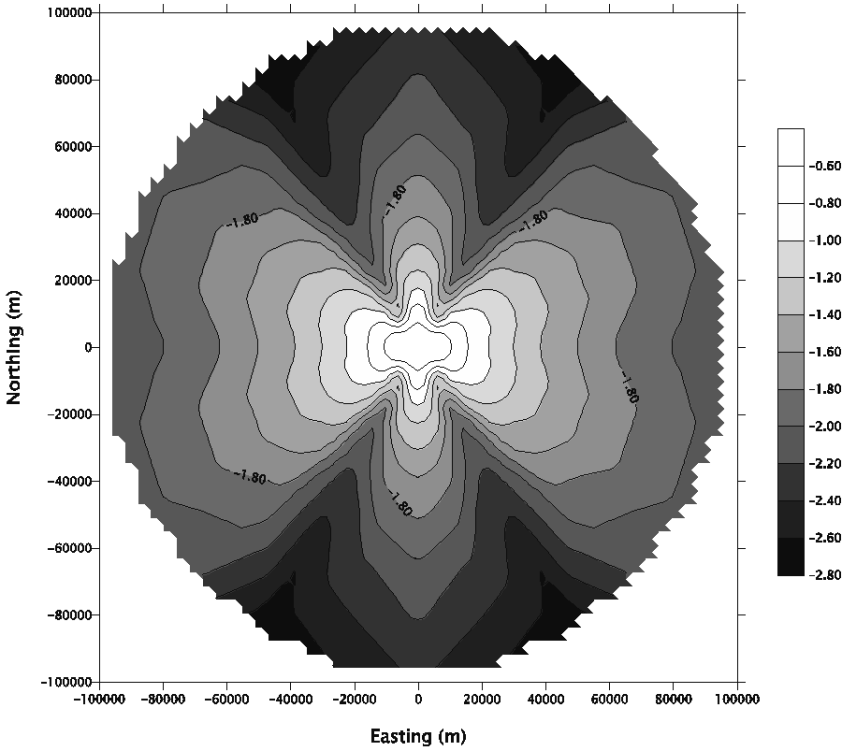


a) 100 x 100 km map.

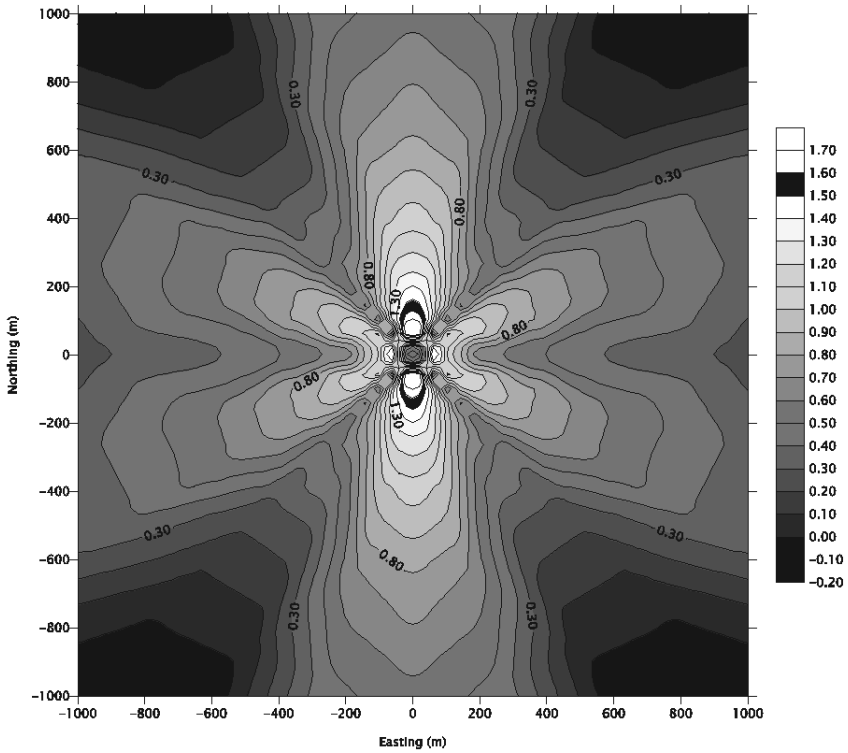


b) 1 x 1 km map.

*Figure 2-10 Map view of effect of magnitude 8.0 strike-slip earthquake on perpendicular target fracture*

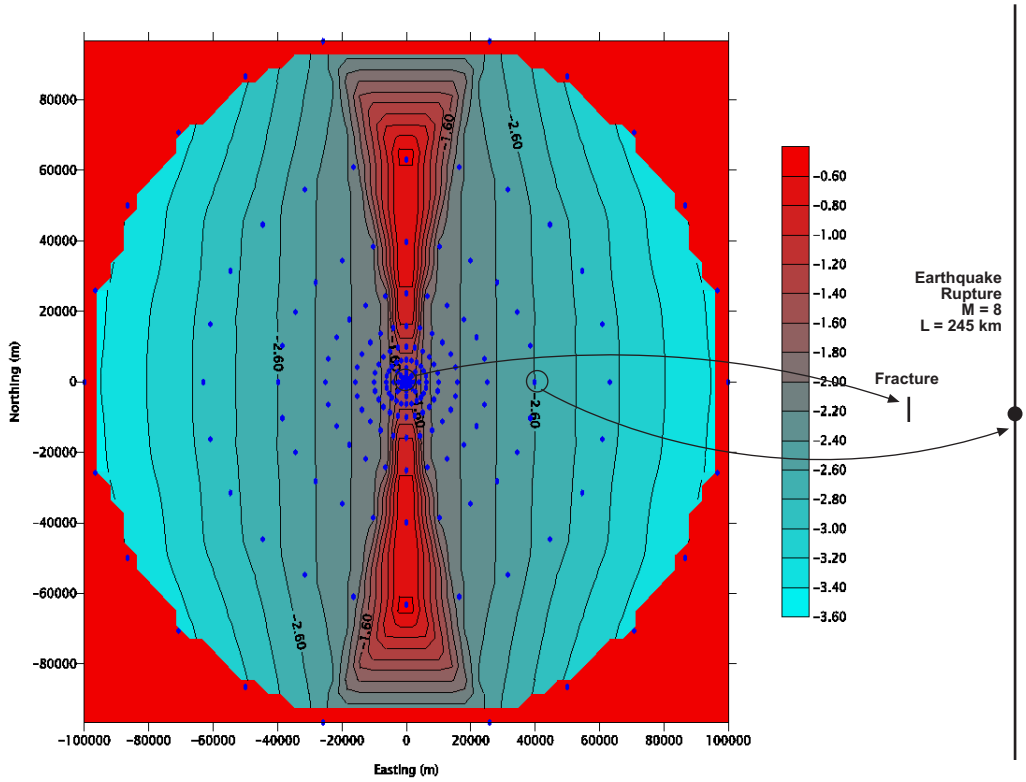


a) Magnitude 8.0.

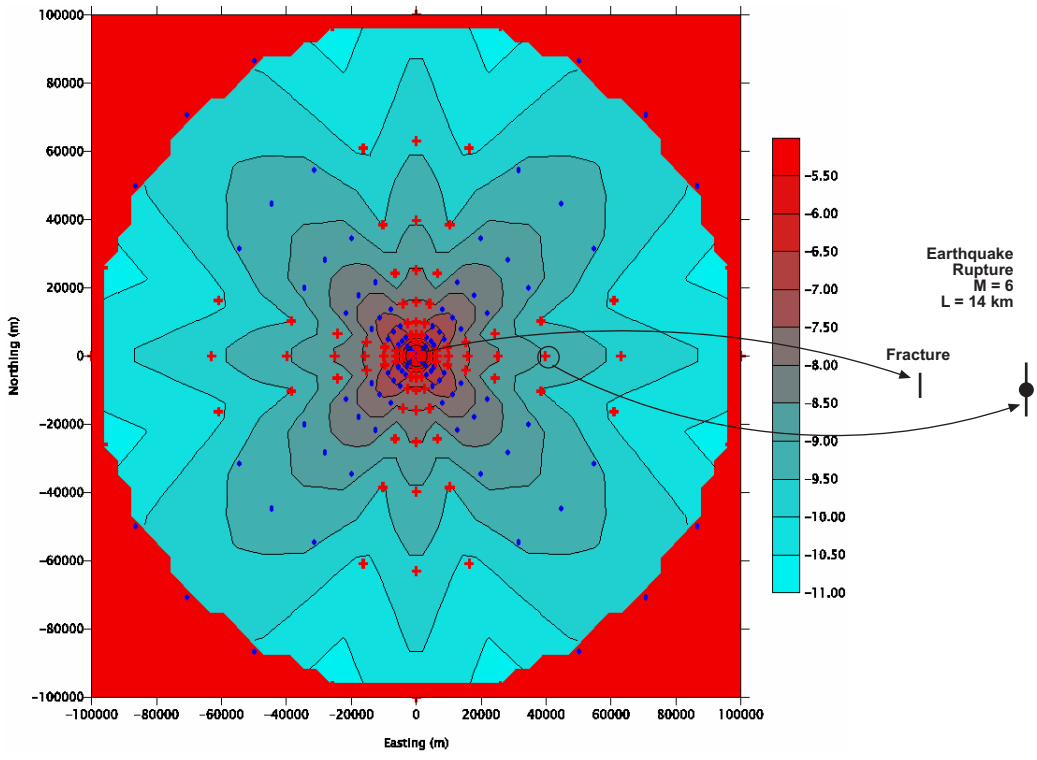


b) Magnitude 6.0.

*Figure 2-11 Map view when distance measured to earthquake epicenter*

At a given location, fractures oriented parallel to the local maximum shear stress orientation will have the greatest shear displacement. The results in the simulations are for the specific case of a NS strike-slip fault. In general, the conservative approach is to

assume that a combination of rupture orientation, slip direction (i.e. strike-slip, reverse, or some combination), azimuth, and target fracture orientation may exist to produce the maximum induced slip possible. In this case the induced slip graphed in Figure 2-4 and derived in equations (11) and (13) can be used to calculate the worst case scenario for any combination of magnitude and distance.

The numerical relations provided by these simulations could be used for relative site ranking when very little actual fracture data is available. As an example of how these relations could be used to make such estimates, total induced slip is calculated for a single reference fracture. These results are also used to make some simple estimates of damaging earthquakes.

In addition, more elaborate calculations are carried out to evaluate whether these simple relations might also provide order-of-magnitude estimates of canister failure when greater knowledge about the rock mass fracture geometry is available.

## 2.2 Task 1.2 – Comparison to TR 99-03 Results

The results graphically shown in Figure 2-4 can be used to roughly estimate the probability of damaging earthquakes. Table 2-2 shows the maximum induced slip values plotted in Figure 2-4; induced slips greater than 1 cm are in italics and those greater than 10 cm in bold.

The next step in the estimate is to determine the probability of occurrence of a damaging earthquake. Table 4-3 of TR-99-03 lists the number of earthquakes to be expected for each magnitude range normalized to a circle with a 100-km radius. These numbers were calculated from the $a$ and $b$ values for each of the seismic zones. The number of earthquakes occurring within the same distance bins on Table 2-2 can easily be calculated based on the area of each bin. Table 2-3 shows the result of this calculation for the Gulf of Bothnia and Table 2-4 for Southern Sweden.

To determine the cumulative effect of the earthquakes in Tables 2-3 and 2-4 on the target 1000 m fracture, the terms of the two matrices can simply be multiplied (Table 2-5). Summing all the slips gives a total induced slip of 2.6 mm over 100,000 years. Thus, even in a very conservative scenario (see below), one would expect no canister failures.

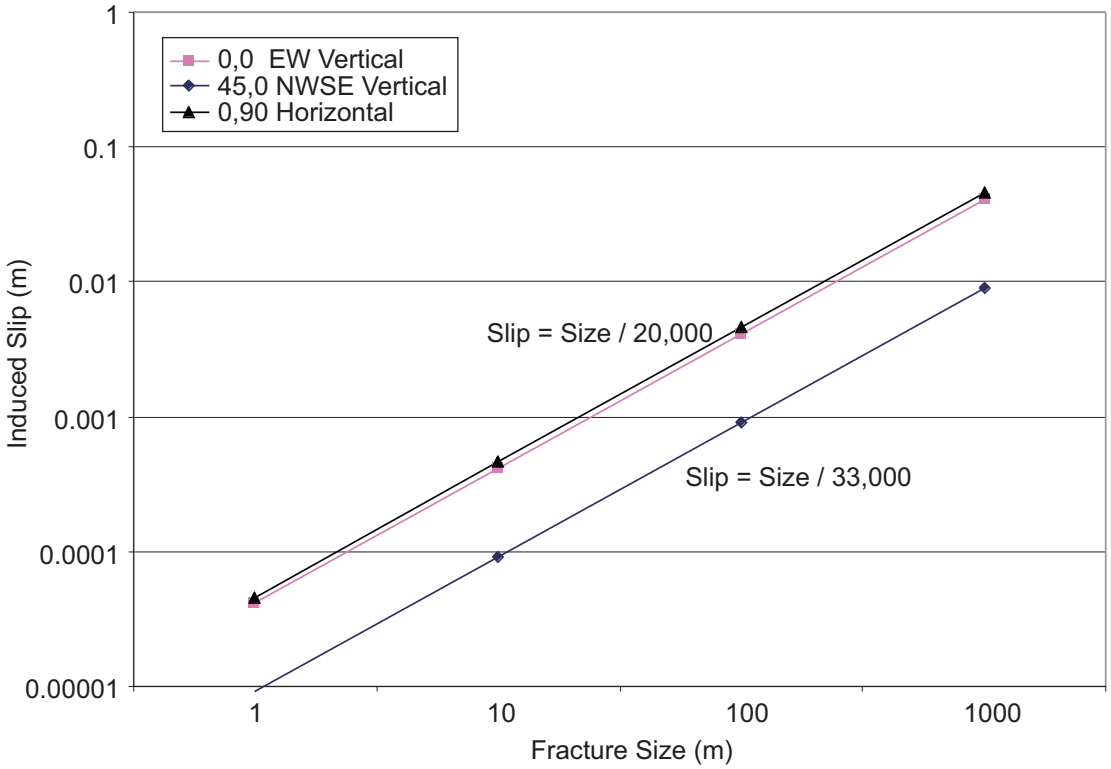


a) Strike-Slip earthquake.

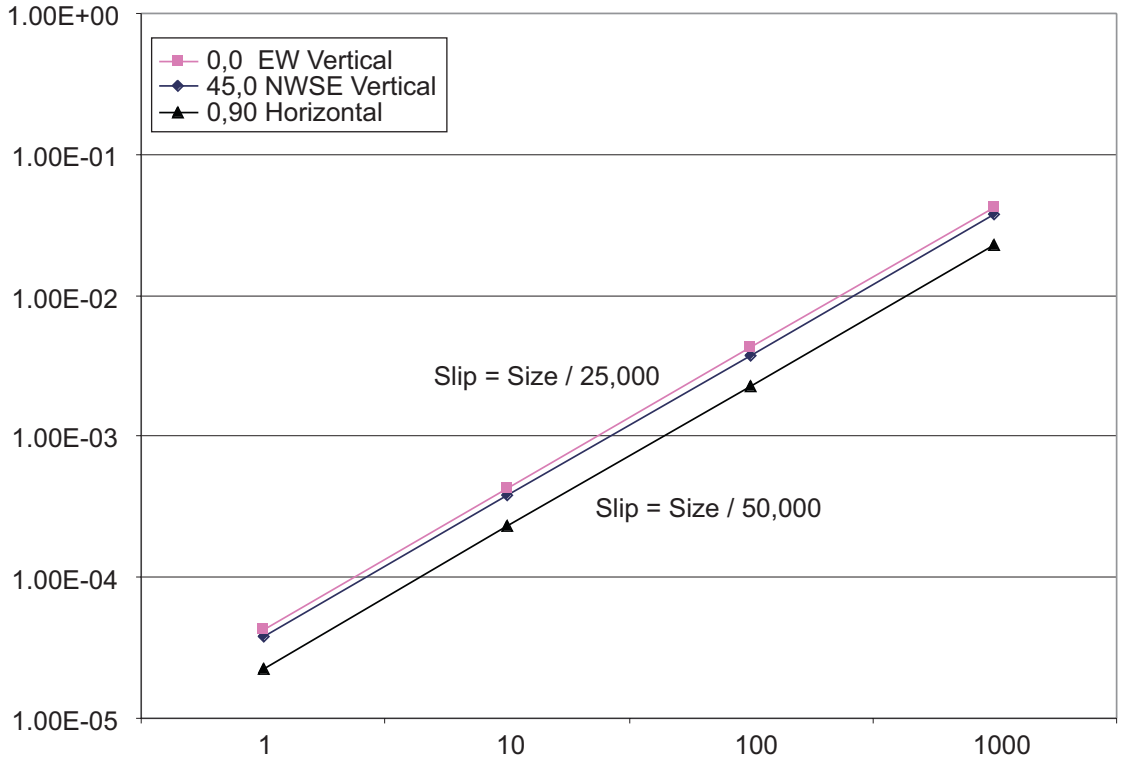


b) Reverse earthquake.

*Figure 2-12 Effect of fracture size on induced slip*

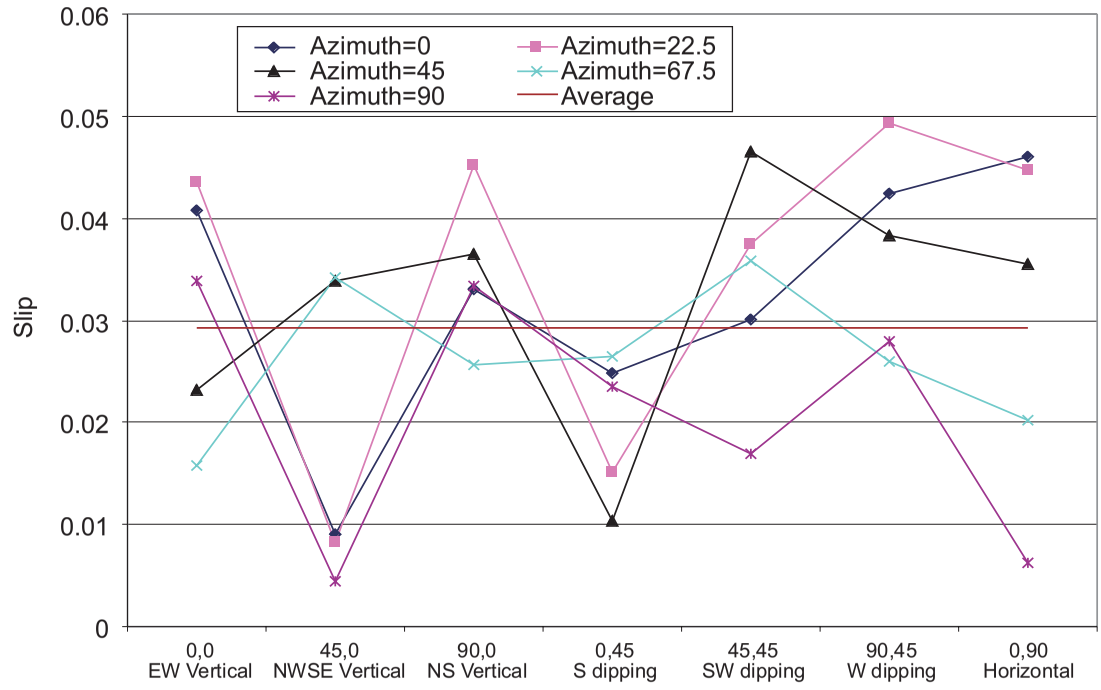


a) Strike-Slip.

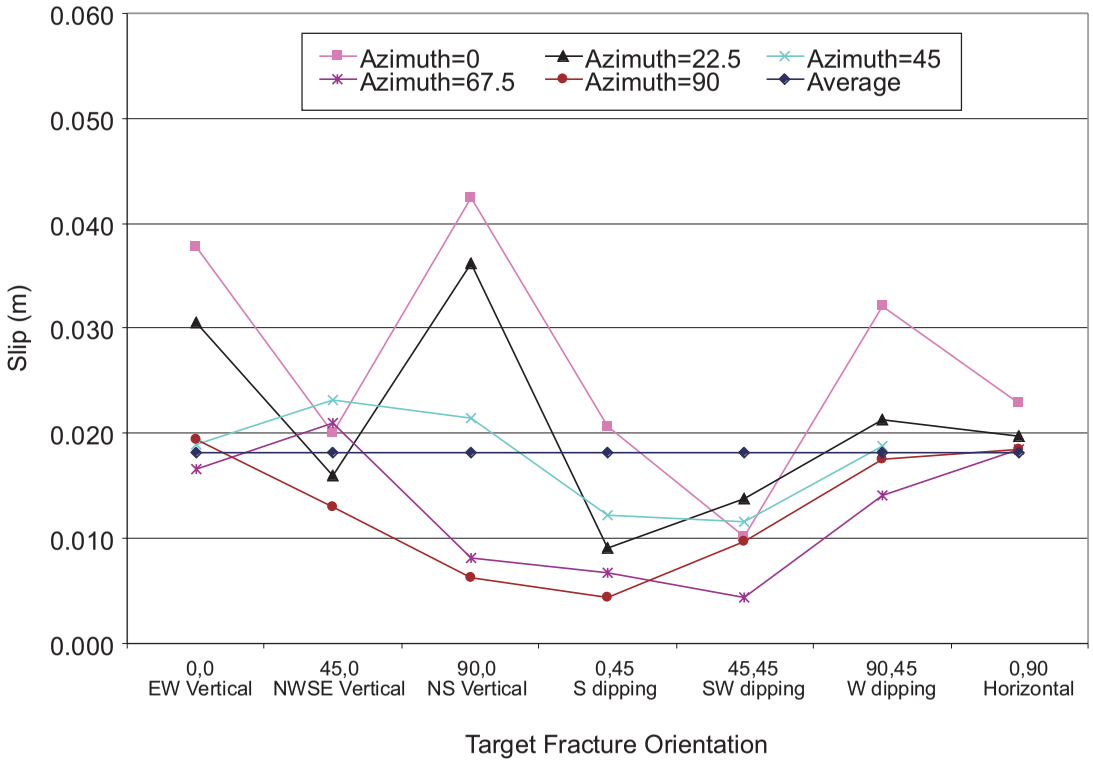


b) Reverse Slip.

*Figure 2-13 Effect of azimuth and target fracture orientation on induced slip*

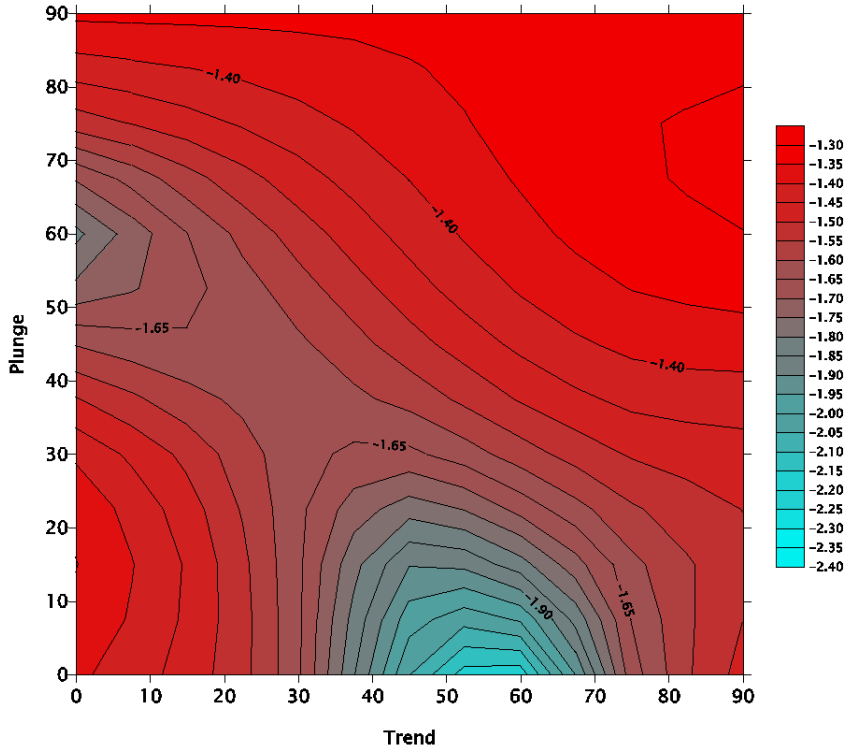


a) Azimuth = 0.

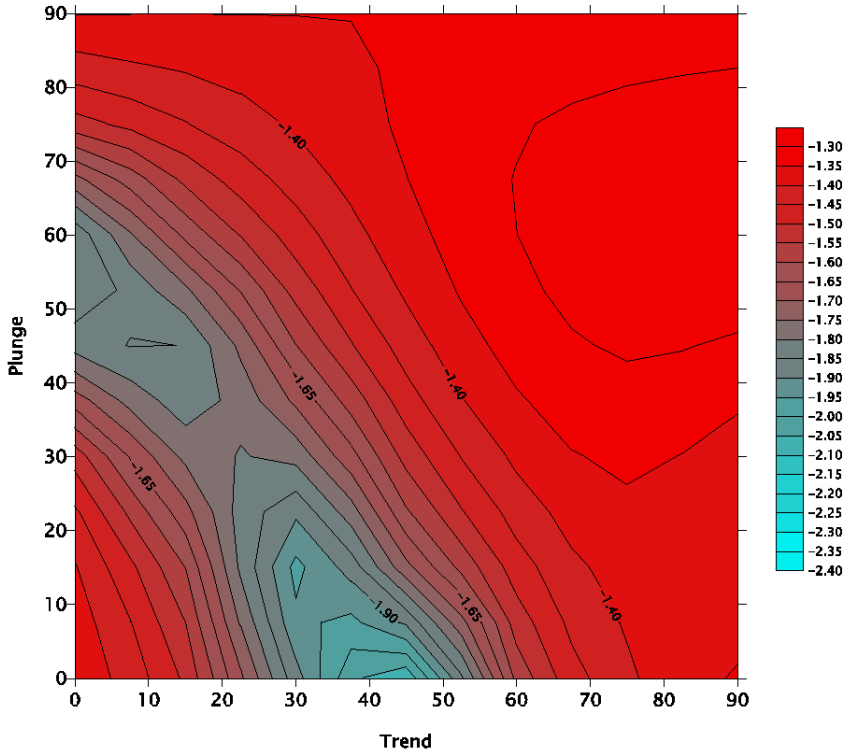


b) Azimuth = 22.5.

*Figure 2-14. Effect of azimuth to earthquake and target fracture orientation on induced slip: countour diagrams: a) azimuth = 0º; b) azimuth = 22.5º; c) azimuth =45º; d) azimuth = 67.5º; e) azimuth = 90º; f) azimuth = geometric average*

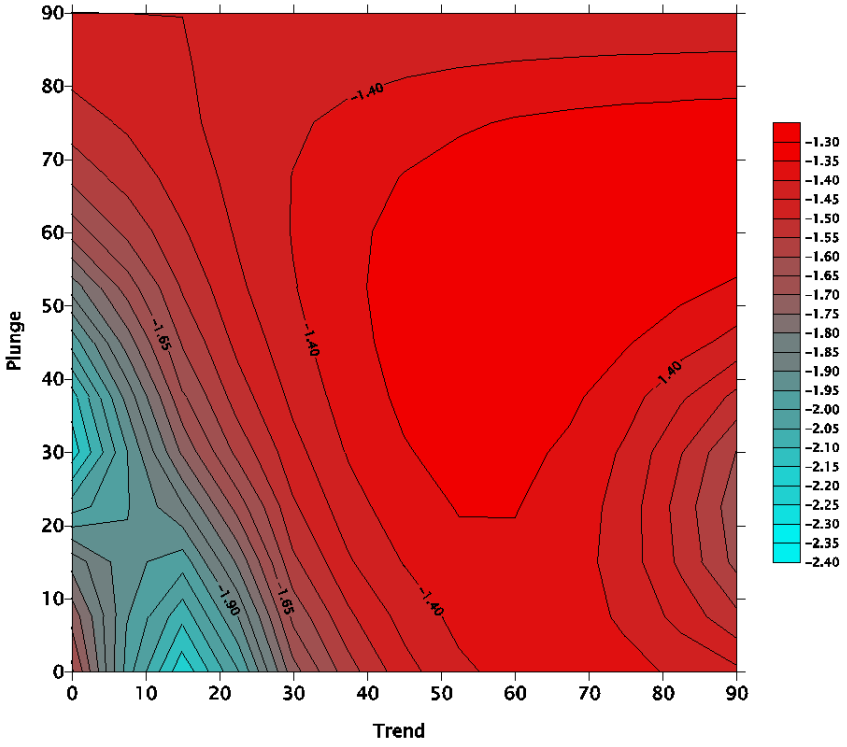


c) Azimuth = 45.

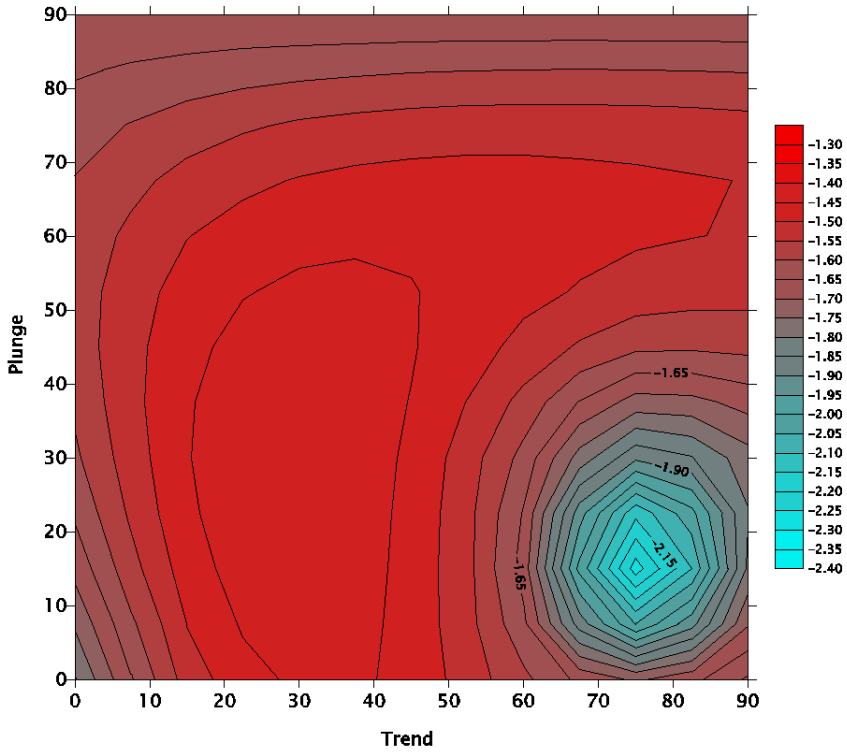


d) Azimuth = 67.5.

*2-14 cont.*

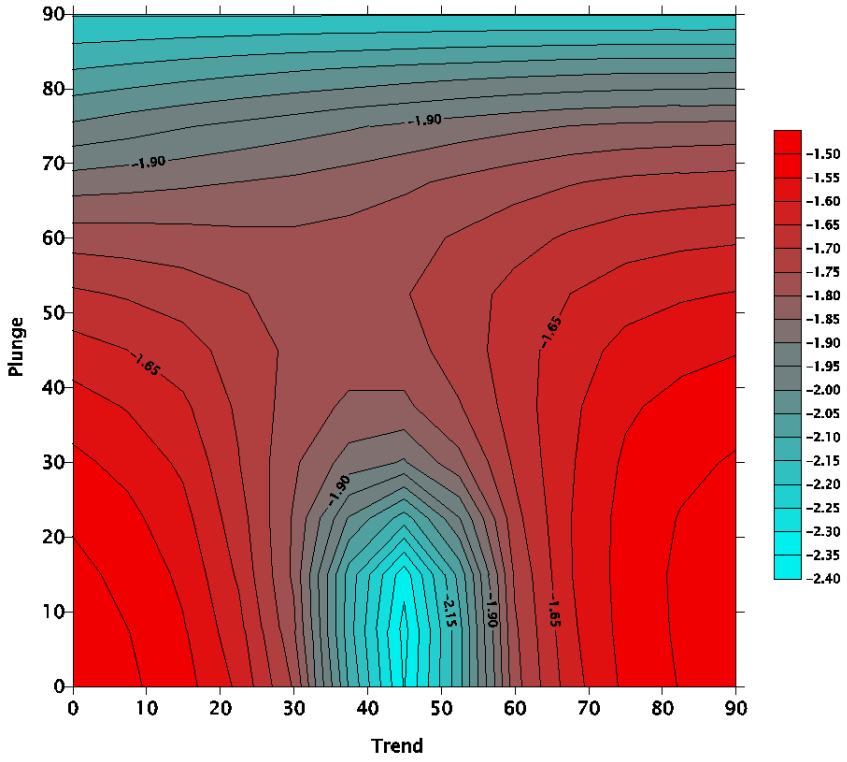


e) Azimuth = 90.

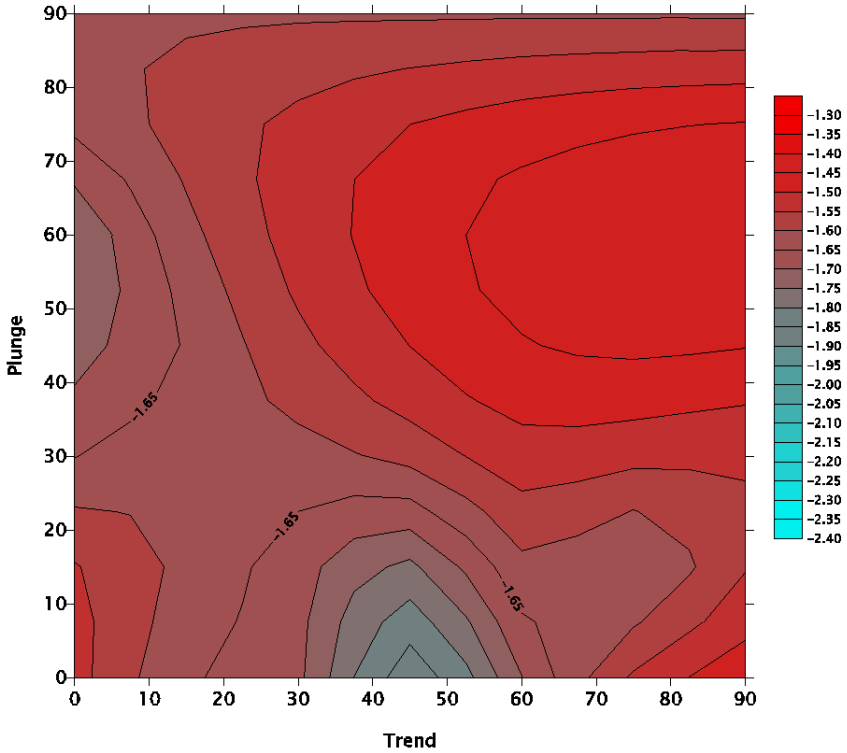


f) Geometric Average of all Azimuths.

*2-14 cont.*

**Table 2-2 Maximum induced slip for distance/magnitude combinations. Target fracture radius =1000 m**

| | Distance (km) | | | | | | | | |
|---|---|---|---|---|---|---|---|---|---|
| **Magnitude** | 100 | 56.2 | 31.6 | 10 | 5.6 | 3.2 | 1.0 | 0.32 | 0.1 |
| 8.0 | 0.004 | *0.013* | *0.036* | **0.14** | **0.263** | **0.483** | **1.757** | **7.05** | **25.56** |
| 7.5 | 0.001 | 0.003 | *0.01* | *0.049* | *0.092* | **0.171** | **0.618** | **2.496** | **9.065** |
| 7.0 | 2E-04 | 8E-04 | 0.003 | *0.017* | *0.032* | *0.06* | **0.216** | **0.882** | **3.213** |
| 6.5 | 3E-05 | 2E-04 | 6E-04 | 0.006 | *0.012* | *0.021* | *0.075* | **0.311** | **1.138** |
| 6.0 | 5E-06 | 2E-05 | 1E-04 | 0.002 | 0.004 | 0.008 | *0.026* | **0.11** | **0.403** |
| 5.0 | 9E-08 | 5E-07 | 3E-06 | 6E-05 | 2E-04 | 7E-04 | 0.003 | *0.013* | *0.05* |
| 4.0 | 1E-09 | 8E-09 | 5E-08 | 1E-06 | 7E-06 | 3E-05 | 3E-04 | 0.001 | 0.006 |

**Table 2-3 Number of earthquakes in 100,000 years, Gulf Of Bothnia, those in bold would be damaging earthquakes according to Table 2-2**

| | Distance Bin (km) | | | | | | | | | |
|---|---|---|---|---|---|---|---|---|---|---|
| **Mag. Range** | 100 – 56.2 | 56.2 – 31.6 | 31.6 – 10 | 10 – 5.6 | 5.6 – 3.2 | 3.2 – 1.0 | 1.0 – 0.32 | 0.32 – 0.1 | < 0.1 | **Sum** |
| 7.5-8.0 | 8.2E-03 | *2.6E-03* | *1.1E-03* | **8.2E-05** | **2.6E-05** | **1.1E-05** | **1.1E-06** | **1.1E-07** | **1.1E-08** | 0.012 |
| 7.0-7.5 | 3.4E-02 | 1.1E-02 | *4.5E-03* | *3.4E-04* | *1.1E-04* | **4.5E-05** | **4.5E-06** | **4.5E-07** | **4.5E-08** | 0.05 |
| 6.5-7.0 | 1.4E-01 | 4.5E-02 | 1.9E-02 | *1.4E-03* | *4.5E-04* | *1.9E-04* | **1.9E-05** | **1.9E-06** | **1.9E-07** | 0.21 |
| 6.0-6.5 | 1 | 1.7E-01 | 7.2E-02 | 5.5E-03 | *1.7E-03* | *7.2E-04* | *7.2E-05* | **7.2E-06** | **7.2E-07** | 0.8 |
| 5.0-6.0 | 14 | 4 | 2 | 1.E-01 | 4.E-02 | 2.E-02 | *2.E-03* | **2.E-04** | **2.E-05** | 19.841 |
| 4.0-5.0 | 252 | 80 | 33 | 3 | 1 | 3.E-01 | 3.E-02 | *3.E-03* | *3.E-04* | 368.02 |
| 3.5-4.0 | 870 | 275 | 114 | 9 | 3 | 1 | 1.E-01 | 1.E-02 | 1.E-03 | 1272.0 |
| Sum | 1135.7 | 359.2 | 149.5 | 11.4 | 3.6 | 1.5 | 1.5E-01 | 1.5E-02 | 1.5E-03 | **1661.0** |

**Table 2-4 Number of earthquakes in 100,000 years, Southern Sweden, those in bold would be damaging earthquakes according to Table 2-2**

| | Distance (km) | | | | | | | | | |
|---|---|---|---|---|---|---|---|---|---|---|
| **Mag. Range** | 100 | 56.2 | 31.6 | 10 | 5.6 | 3.2 | 1.0 | 0.32 | 0.1 | Sum |
| 7.5-8.0 | 9.6E-02 | *3.0E-02* | *1.3E-02* | **9.6E-04** | **3.0E-04** | **1.3E-04** | **1.3E-05** | **1.3E-06** | **1.3E-07** | 0.14 |
| 7.0-7.5 | 3.1E-01 | 9.7E-02 | *4.0E-02* | *3.1E-03* | *9.7E-04* | **4.0E-04** | **4.0E-05** | **4.0E-06** | **4.0E-07** | 0.44999 |
| 6.5-7.0 | 1 | 3.2E-01 | 1.3E-01 | *1.0E-02* | *3.2E-03* | *1.3E-03* | **1.3E-04** | **1.3E-05** | **1.3E-06** | 1.47996 |
| 6.0-6.5 | 3 | 1 | 4.5E-01 | 3.4E-02 | *1.1E-02* | *4.5E-03* | *4.5E-04* | **4.5E-05** | **4.5E-06** | 4.99987 |
| 5.0-6.0 | 48 | 15 | 6 | 4.8E-01 | 1.5E-01 | 6.3E-02 | *6.3E-03* | **6.3E-04** | **6.3E-05** | 69.9982 |
| 4.0-5.0 | 526 | 166 | 69 | 5 | 2 | 6.9E-01 | 6.9E-02 | *6.9E-03* | *6.9E-04* | 768.981 |
| 3.5-4.0 | 1337 | 423 | 176 | 13 | 4 | 2 | 1.8E-01 | 1.8E-02 | 1.8E-03 | 1954.95 |
| Sum | 1915.2 | 605.7 | 252.1 | 19.2 | 6.1 | 2.5 | 2.5E-01 | 2.5E-02 | 2.5E-03 | **2801.0** |

**Table 2-5 Probabilistic maximum cumulative slip on single large 1000 m fracture exposed to seismicity with Gulf of Bothnia parameters**

| | Distance (km) | | | | | | | | | |
|---|---|---|---|---|---|---|---|---|---|---|
| **Mag.** | 100 | 56.2 | 31.6 | 10 | 5.6 | 3.2 | 1.0 | 0.32 | 0.1 | Sum |
| 8 | 3.4E-05 | 3.5E-05 | 3.8E-05 | 1.1E-05 | 6.8E-06 | 5.2E-06 | 1.9E-06 | 7.6E-07 | 2.8E-07 | 1.3E-04 |
| 7.5 | 3.4E-05 | 3.7E-05 | 4.6E-05 | 1.7E-05 | 9.9E-06 | 7.7E-06 | 2.8E-06 | 1.1E-06 | 4.1E-07 | 1.6E-04 |
| 7 | 3.0E-05 | 3.5E-05 | 5.1E-05 | 2.5E-05 | 1.4E-05 | 1.1E-05 | 4.1E-06 | 1.7E-06 | 6.1E-07 | 1.7E-04 |
| 6.5 | 1.8E-05 | 2.7E-05 | 4.2E-05 | 3.1E-05 | 2.0E-05 | 1.5E-05 | 5.4E-06 | 2.2E-06 | 8.2E-07 | 1.6E-04 |
| 6 | 6.4E-05 | 1.0E-04 | 2.0E-04 | 2.1E-04 | 1.7E-04 | 1.4E-04 | 4.6E-05 | 2.0E-05 | 7.2E-06 | 9.6E-04 |
| 5 | 2.2E-05 | 3.8E-05 | 8.3E-05 | 1.6E-04 | 1.9E-04 | 2.5E-04 | 1.1E-04 | 4.3E-05 | 1.7E-05 | 9.0E-04 |
| 4 | 1.3E-06 | 2.2E-06 | 5.2E-06 | 1.1E-05 | 1.9E-05 | 3.5E-05 | 3.5E-05 | 1.5E-05 | 6.8E-06 | 1.3E-04 |
| Sum | 2.0E-04 | 2.8E-04 | 4.7E-04 | 4.6E-04 | 4.3E-04 | 4.6E-04 | 2.1E-04 | 8.4E-05 | 3.3E-05 | **2.6E-03** |

The lower right-hand number (2.6E-03 m) represents the sum of all the slips in the matrix of magnitude and distance.

Table 2-5 represents the average probabilistic earthquake scenario. For earthquakes with numbers less than 1, the values in Table 2-5 represent probabilities rather than numbers. Of course, there is no such thing as a fractional earthquake. For example, while a magnitude 7.0 to 7.5 at a distance of 31.6 km or closer in Table 2-3 has a probability of just 0.45% in 100,000 years (or one every 22 million years) if one does occur it will cause canister failures. So rather than multiplying the probabilities by the induced slips, the cumulative probability of a damaging earthquake must be determined from Tables 2-3 and 2-4. This is done by summing the earthquake probabilities of all the induced slips >10 cm (in bold) values in Table 2-3 which gives a cumulative probability of 0.0004 or 0.04%. The same can be done for the earthquakes which cause induced slips > 1 cm, and for the Southern Sweden seismicity (Table 2-6).

To conclude, this estimate shows that the cumulative slip produced by small earthquakes can sum to produce canisters failures. It also illustrates how the method can be used to estimate the slip potential of a reference fracture for site comparison.

**Table 2-6 Summary of damaging earthquake estimates**

| Parameter | Southern Sweden | Gulf of Bothnia | How Calculated |
|---|---|---|---|
| Mean Cumulative Slip (m) | 1. $1x10^{-3}$ | $2.6x10^{-3}$ | Sum of cumulative slips, Table 2-5 |
| Probability of one 10cm slip | 0.27% | 0.04% | Sum of bold values in Tables 2-3 and 2-4 |
| Probability of one 1 cm slip | 13% | 1.9% | Sum of bold and italic values in Tables 2-3 and 2-4 |

There are several factors that make the calculations above different from the simulations reported in TR-99-03:

Table 2-2 is for a target fracture radius of 1000 m. This is significantly larger than the maximum fracture size in the generic site models of TR-99-03. The maximum fracture radius in the Aberg model was 50 m, and for Beberg and Ceberg, 160 m. As will be shown in Figure 2-12, the effect of fracture size is linear, so that the values in Table 2-2 would be reduced if the size distributions for Aberg, Beberg and Ceberg were taken into account.

1. The estimate uses the maximum induced slip. In the simulations performed in TR-99-03, there may not be a canister-intersecting fracture with the correct orientation to achieve the maximum induced slip.

2. In calculating the cumulative slip values (Table 2-5) all slips are assumed to sum. In the TR-99-03 simulations, some earthquake caused the opposite sense of induced slip, and most other cases the direction of slip was not collinear for two different earthquakes.

3. In TR-99-03 a correction was made to account for the probability that the actual slip would be less than the peak induced slip which occurs only at the center of the target fracture. In this estimate only the peak slip is used.

4. The magnitudes in the induced slip tables (Tables 2-3 and 2-4) are discrete values (i.e. 4.0) while the number of predicted earthquakes are ranges (i.e. 3.5 – 4.0). Therefore, for each magnitude class, the total induced slip is overestimated, since it is based on the maximum earthquake occurring in that class.

In order to directly compare these numbers with the results shown in TR 99-03, it would be necessary to adjust the calculated slips by the fracture size distribution, and also take into account for the fact that there are hundreds of fractures that intersect canisters at the three generic sites. The fracture size adjustment would have the effect of reducing the predicted slip, while the adjustment for the multiple fracture-canister intersections would multiply the probability of canister failure.

A more sophisticated calculation, taking these and other effects into account, is shown in the next section.

One final test of the sensitivity analysis and the regressions relations developed from it was to reproduce the sequence of calculations employed in TR 99-03 as closely as possible, but to substitute the regression relations for the actual Poly3D simulations. This required a more complex calculation than the previous one involving a single 1000 m fracture.

1. First, it is necessary to forecast the number and magnitude of future earthquakes. This is based on the magnitude/frequency relation relevant to the site under investigation, the area on which the calculation of these parameters have been based, and the target area over which the magnitude/frequency is to be calculated. For Southern Sweden, the parameters used were $a = 563.9914$, and $b = 1.04$. As in TR 99-03, the target area was assumed to be a circle of radius 100 km from the centroid of the repository. It is also necessary to define the time duration of interest. For this exercise, the time interval is 100,000 years. Earthquakes are assumed to occur at uniformly random locations throughout the 100 km circle surrounding the repository.

2. Next, the size distribution of fractures intersecting canisters needs to be calculated. For the three generic sites in Sweden studied in TR 99-03, the fracture radii conform to a power law distribution. However, the parameter values that characterize this distribution cannot be used directly, since the subset of fractures that intersect canisters is a biased subset of the parent population. The bias occurs because fractures oriented orthogonal to the canister holes will have a higher probability of intersecting a hole than will a fracture that is inclined. Fractures that are nearly parallel to the hole axis have the lowest probability of intersecting a canister hole. Moreover, the probability of intersection is also a linear function of fracture radius; the probability for a fracture independent of the fracture's orientation increases linearly with fracture radius (La Pointe and Hudson, 1985). Thus, the fractures that intersect canister holes tend to be preferentially larger than the general population of fractures, and fractures that are oriented subparallel to the canister hole tend to be under-represented relative to the general fracture population. For a power law relation, the relation between fracture radius and sampling probability implies that the radius distribution will have an exponent equal to 1.0 greater than the exponent that describes the parent fracture population (Appendix A).

3. Not all canisters have fractures intersecting them. Since a large number of fracture model realizations were used in TR 99-03, it was possible to determine the mean percentage of canisters that would be intersected by fractures, and also the standard deviation of the intersection percentage. For Aberg, the mean percentage of canisters intersected was 62.7% with a standard deviation of 2.8%. The intersection percentage was well characterized by a Normal distribution, passing the Chi-Square, Kolmogorov and Anderson-Darling tests at confidence. To compute the number of canisters intersected by fractures, a Monte Carlo sample of a Normal distribution with mean equal to 0.627 and standard deviation equal to 0.028 was taken and applied to the total number of canisters in the Aberg repository layout.

4. Sizes of fractures intersecting these canisters was based upon adding 1.0 to the Power law characterizing the parent population. The parent population of fractures at Aberg reported in TR 99-03 (Table 3-3) is on the order of 1.60 for all sets.

5. Orientations of fractures relative to the orientation of faults on which the earthquake was taking place were neglected, since

   – Sets of at least three different orientations with considerable dispersion occurred at Aberg, suggesting that many orientations are present;

   – Sensitivity analyses reported in Section 2.1.3 showed that relative orientation is of secondary importance.

The general procedure to compute induced displacement follows from the assumptions and values described above:

1. Using the earthquake magnitude/frequency relations described above, it is possible to forecast the future number of earthquakes of any given magnitude. The frequency is adjusted for the area of interest. The temporal pattern of occurrence of each earthquake is assumed to be a Poissonian Process, as in most earthquake codes and literature.

2. For each earthquake that occurs over the next 100,000 years, it necessary to compute its consequences in terms of induced fracture slip. Since orientation can be neglected as a minor effect, then all that matters is the distance and magnitude, and the fracture size. Locations are assumed to be uniformly random within the 100-km circle. Monte Carlo sampling was used to select a location within this circle. Because the distance and magnitude are now defined, it is possible to use the regression relations to estimate the impact of the earthquake on 1000-m radius fractures at each of the canisters at which there is a fracture.

3. Not all fractures intersecting the canisters are 1000 m in radius. Thus the induced displacement is adjusted, and almost always lowered, based upon the actual fracture radius. This relation is linear, as shown in Equation (14).

4. Another consideration in TR 99-03 is that Poly3D calculates the displacement at the center of a fracture. There is no reason to assume that canister emplacement holes will intersect fracture at their center. Rather, intersection is uniformly random with respect to the fracture surface. Induced displacement decreases with increased distance from the fracture centroid, as described by Equation 14 (Pollard and Segall, 1987):

$$\begin{Bmatrix} \Delta u_I \\ \Delta u_{II} \\ \Delta u_{III} \end{Bmatrix} = \begin{Bmatrix} \Delta\sigma_I \\ \Delta\sigma_{II} \\ \dfrac{\Delta\sigma_{III}}{1-\upsilon} \end{Bmatrix} \frac{2(1-\upsilon)}{\mu} (R^2 - x_2{}^2)^{\frac{1}{2}} \tag{15}$$

where

- $\begin{Bmatrix} \Delta u_I \\ \Delta u_{II} \\ \Delta u_{III} \end{Bmatrix}$ represents the displacements parallel and perpendicular to the fracture,
- $\begin{Bmatrix} \Delta\sigma_I \\ \Delta\sigma_{II} \\ \Delta\sigma_{III} \end{Bmatrix}$ represents the stresses on the fracture,
- $\mu$ and $\nu$ are elastic moduli,
- $R$ is the fracture radius, and
- $X_2$ is the distance from the fracture center to the fracture tip.

This equation shows that the maximum displacement occurs at the fracture center, and decreases to 0.0 at the fracture tip. It also shows that if the displacements are known at the fracture center, and the fracture radius is known, then it is possible to calculate the reduced displacement as a function of the distance from the fracture center. It is assumed that a canister could intersect a fracture anywhere on the fracture surface with equal probability, and displacements are adjusted based on this equation.

Five thousand realizations of earthquakes for a 100,000-year period were simulated, using the parameters for Aberg. The parameters used are summarized in Table 2-7.

One difference between this simplified calculation and the more sophisticated Poly3D calculations reported in TR 99-03 is that the *direction* of slip induced by each earthquake cannot be reproduced. The regression relations derived in Section 2.1.1. only describe the amount of slip, not the vectorial direction. As a result, it is not possible to calculate the cumulative slip induced by multiple earthquakes. This impacts the calculation of canister failure due to the cumulative effects of multiple earthquakes. Calculations relative to the impact of damaging earthquakes are not affected.

The results of these calculations are shown in Table 2-8.

**Table 2-7 Parameters used for comparison between sensitivity analysis and TR 99-03 results**

| Quantity | Value |
|---|---|
| Earthquake Magnitude/Frequency Parameters | a = 563.9914<br>b = 1.04<br>Magnitudes are computed as a temporal Poisson Process. |
| Area over which earthquakes are simulated | Circle, 100 km in radius |
| Time Period Considered | 100,000 years |
| Minimum Magnitude Simulated | $M_L$ = 4.5 |
| Orientation of Earthquake Fault with Respect to Fracture | Worst-Case Result from Section 2.3 |
| Earthquake Rupture Dimensions | Based upon Magnitude; Uses regression relations from Wells & Coppersmith (1994). Rupture width and length are stochastically drawn via Monte Carlo sampling from regression results, as in TR 99-03 |
| Earthquake Rupture Slip | Average subsurface slip, based upon regressions reported in TR 97-07 that were carried out on Wells & Coppersmith's (1994) data. Rupture slip is stochastically drawn via Monte Carlo sampling from regression results, as in TR 99-03 |
| Tip Distance | Uniformly Random throughout entire 100 km radius circle |
| Fracture Sizes | Based on results for Aberg reported in TR 99-03:<br>Power Law distribution<br>Minimum Size = 10.0 m<br>Exponent = 2.6 |
| Number of realizations | 5000 |
| Threshold for "Damaging" earthquake | 0.1 m |
| Percentage of canisters intersected by fractures | Normal Distribution<br>Mean = 62.7%<br>St. Dev. = 2.8%<br>Based upon analysis of Aberg models used in TR 99-03 |
| Correction for Non-centrality of fracture/canister intersection | As modeled in TR 99-03; Fractures are assumed to intersect a canister at a uniformly random location, and computed displacements are adjusted as in TR 99-03 |

**Table 2-8 Results of TR-99-03 comparison**

| Failure Measure | This Study | TR 99-03 (Table 5-1) |
|---|---|---|
| Probability of Canister Failure due to Single Damaging Earthquakes | 0.70% | 0.59% |
| Probability of Canister Failure due to Cumulative Effects | 0.12% | 0.06% |
| Probability of Canister Failure due to Single Damaging Earthquakes & Cumulative Effects | 0.82% | 0.65% |

This table shows that the results using the regression relations and approximating some of the calculation refinements used in TR 99-03 leads to a reasonable match, although the failure probability is higher in the current study, particularly for the failures due to cumulative effects. This higher probability may be due to the inability in the current method to vector sum of the displacements. The results shown are for the case when all induced displacements are additive, which is certainly more conservative than calculating the vector displacement.

Another measure of canister failure risk is to estimate the number of damaging earthquakes, and the consequences given that a damaging earthquake occurs. These results were reported in Table 5-2 and Table 5-3 in TR 99-03.

**Table 2-9 Comparison of failures in this study and TR 99-03**

| Failure Measure | This Study | TR 99-03 (Table 5-2 and Table 5-3) |
|---|---|---|
| Number of Damaging Earthquakes in 100,000 years | Mean = 0.0004<br>Median = 0.0<br>Maximum = 1 | Mean = 0.325<br>Median = 0.0<br>Maximum = 5 |
| Number of canister failures during damaging earthquake | Mean = 1.80%<br>Median = Not Calculated<br>Maximum = 3.0% | Mean = 1.82%<br>Median 0.31%<br>25.4% |

Both the current and the previous study shows that a damaging earthquake leads to a small number of canister failures, and that the number of expected damaging earthquakes over a 100,000 year time period is very small. Part of the disagreement between the current and previous results in the Table is due to the extremely small sample size on which to calculate statistics.

# 3 EVALUATION OF CONSERVATIVENESS

## 3.1 Task 2.1 – Fracture Propagation Effects

The external boundaries of the Franc3D model form a cubic block (Figure 3-1). A penny-shaped fracture is located in the center of the block. The fracture surface constitutes an internal boundary. The fracture is dipping 45°. Ranges of different fracture and block size are summarized in the table below.

**Table 3-1 Size of the fracture and the block**

| Fracture radius [m] | Block height/width [m] |
|---|---|
| 0.01 | 0.1 |
| 1 | 10 |
| 5 | 100 |
| 10 | 100 |

### 3.1.1 Material properties

The material properties are used after Shen (1993) so that the results of the analysis by Shen and the present analysis can be compared. The Young's modulus of the rock is set to 6.2 GPa and the Poisson ratio to 0.28. This Young's modulus is typical for gypsum material that has been used for laboratory test by Shen. This value should be compared with the Young's modulus equal to 75 GPa used in TR 97-07 (La Pointe and others, 1997) that is a representative value for typical intact rock found in Sweden (Pusch, 1996). On the other hand, the material surrounding the fracture is a fractured rock mass. Its quality is lower than for an intact rock material. It is thus valid to use lowered values of E. Table 3-2 below summarizes the mechanical properties used in this study.

### 3.1.2 Boundary conditions

The displacements of the base of the model are set to 0 in the x, y, and z directions.

Vertical normal compressive loads are applied to the top of the model. Loads are chosen within a range that includes the minimum normal compressive loads required for the propagation of the fracture of the different cases. Loads vary within the range of $\sigma_n \in$ [1 MPa; 100 MPa].

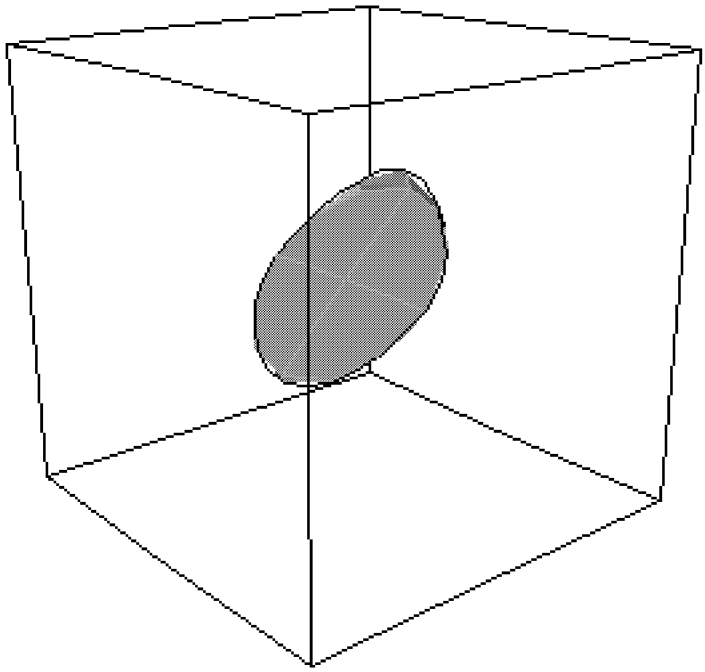

*Figure 3-1 Example of Franc3D model. The penny shape fracture is in the centre of the model*

**Table 3-2 Mechanical properties used in the study (after Shen, 1993)**

| Parameter name | Value | Unit |
|---|---|---|
| E (Young's modulus) | $6.20 \cdot 10^9$ | Pa |
| ν (Poisson's ratio) | 0.28 | - |
| $G_{Ic}$ | 50 | $J/m^2$ |
| $G_{IIc}$ | 500 | $J/m^2$ |
| $K_{Ic}$ | $5.80 \cdot 10^5$ | $Pa \cdot m^{0.5}$ |
| $K_{IIc}$ | $1.83 \cdot 10^6$ | $Pa \cdot m^{0.5}$ |

### 3.1.3 Results

The results are found consistent with the laboratory test carried out by Shen (1993). The stress intensity factors in mode I and II, $K_I$ and $K_{II}$, respectively, are computed by Franc3D. The stress intensity factors $K_I$ and $K_{II}$ are linear functions of the loading stress, $\sigma_n$, of the form:

$$K_I = \gamma_I \cdot \sigma_n \quad (16a)$$

$$K_{II} = \gamma_{II} \cdot \sigma_n \quad (16b)$$

For different fracture radii, the $\gamma_I$ and $\gamma_{II}$ functions are presented in Figure 3-2.

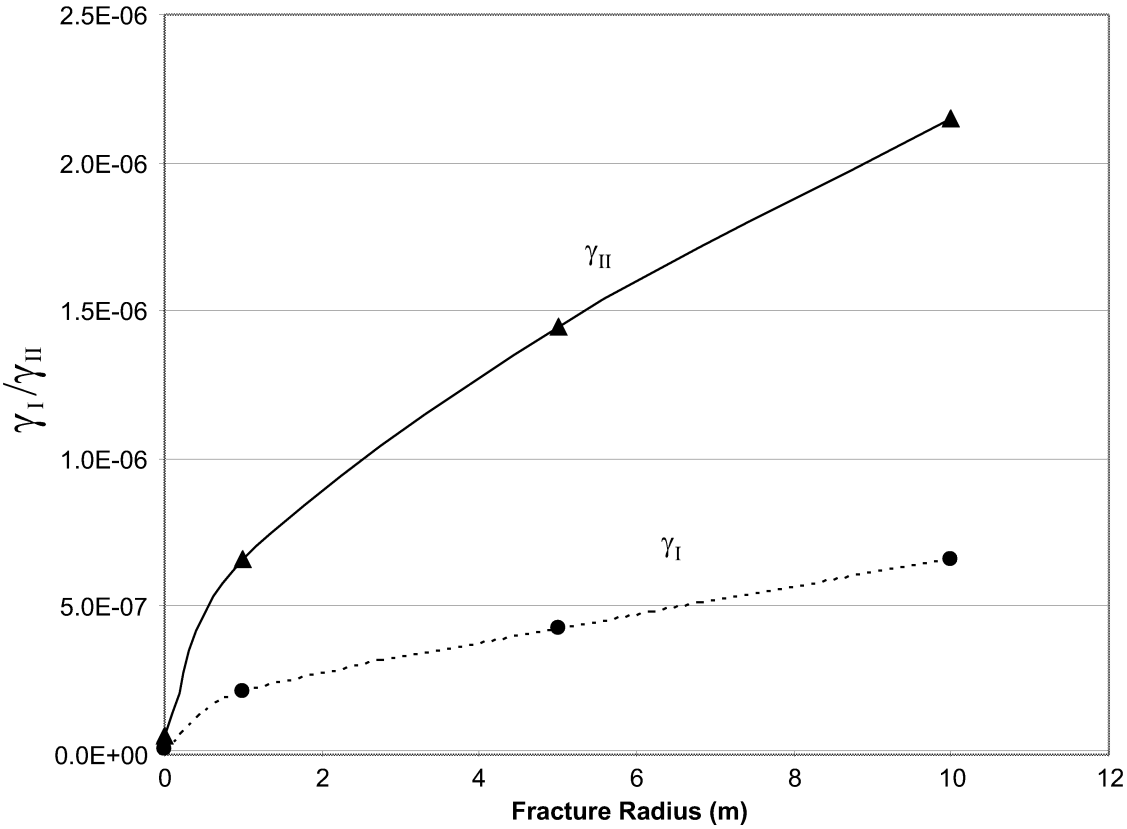


*Figure 3-2 Ratio $K/\sigma_n$ function of the fracture radius*

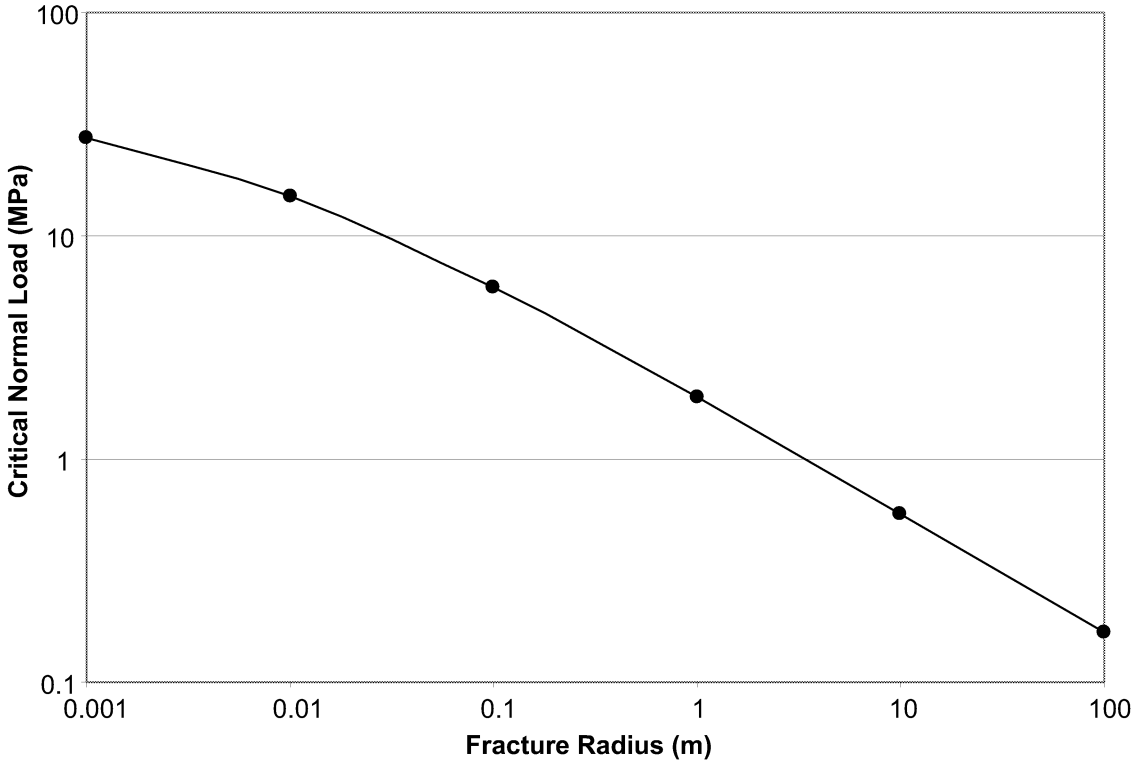


*Figure 3-3 Critical normal load that initiates fracture propagation as a function of the fracture radius.*

Curve fitting of the plot of $\gamma_I$ and $\gamma_{II}$ functions indicates that $\gamma_I$ and $\gamma_{II}$ are increasing exponential functions of the fracture radius of the form:

$$\gamma_I = a_I \cdot r^{b_I} ; 0<b_I<1 \tag{17}$$

$$\gamma_{II} = a_{II} \cdot r^{b_{II}} ; 0<b_{II}<1 \tag{18}$$

Replacing Eq. (17) and Eq. (18) in Eq. 16a and Eq. 16b, respectively, and then putting Eq. 16a and Eq. 16b in the propagation criterion F expression gives:

$$F = \sigma_n^2 \left[ \left( \frac{a_I \cdot r^{b_I}}{K_{Ic}} \right)^2 + \left( \frac{a_{II} \cdot r^{b_{II}}}{K_{IIc}} \right)^2 \right] \tag{19}$$

Propagation of the fracture occurs when $F=1$. This gives the expression of the normal load that initiate propagation as a function of the fracture radius:

$$\sigma_{nc} = \frac{1}{\sqrt{\left( \frac{a_I \cdot r^{b_I}}{K_{Ic}} \right)^2 + \left( \frac{a_{II} \cdot r^{b_{II}}}{K_{IIc}} \right)^2}} \tag{20}$$

Equation 20 is illustrated by Figure 3-3.

The critical normal load that initiates fracture propagation is a decreasing function of the fracture radius. The computation of the maximum shear displacement prior to fracture propagation can be calculated by Poly3D. The Poly3D models discussed in the next section are based on fracture radius and critical normal load presented in Figure 3-3.

## 3.2 Poly3D model set-up

### 3.2.1 Geometry

The Poly3D model is a penny shaped fracture. The angle between the fracture and the normal compressive load is 45°. The fracture shear displacement is observed by a vertical observation grid normal to the strike direction of the fracture (Figure 1-4).

### 3.2.2 Material properties

The material properties are the same as in the section 3.1.1. They are summarized in Table 3-3 below:

**Table 3-3 Material properties used in the Poly3D analysis**

| Parameter name | Value | Unit |
|---|---|---|
| E (Young's modulus) | $6.20 \cdot 10^9$ | Pa |
| ν (Poisson's ratio) | 0.28 | - |

Ranges of different fracture and observation grid sizes are summarized in the table below.

**Table 3-4 Size of the fracture and the observation grid**

| Fracture radius [m] | Observation grid height/width [m] |
|---|---|
| 0.001 | 0.01 |
| 0.01 | 0.1 |
| 1 | 10 |
| 10 | 100 |
| 100 | 1000 |

### 3.2.3 Boundary conditions

The penny shape fractures of different radii are subjected to the critical normal loads calculated in Franc3D. The loading values are presented in the table below.

**Table 3-5 Critical loading that initiate fracture propagation**

| Fracture radius [m] | Critical loading [MPa] |
|---|---|
| 0.001 | 27.50 |
| 0.01 | 15.00 |
| 0.1 | 5.84 |
| 1 | 1.88 |
| 10 | 0.57 |
| 100 | 0.17 |

### 3.2.4 Results

The results for displacements at the fracture centroid are presented in Figure 3-4. The figure shows that the maximum shear displacement in the fracture is an increasing function of the fracture radius. Even for large fractures, the shear displacements are still of the order of millimeters.

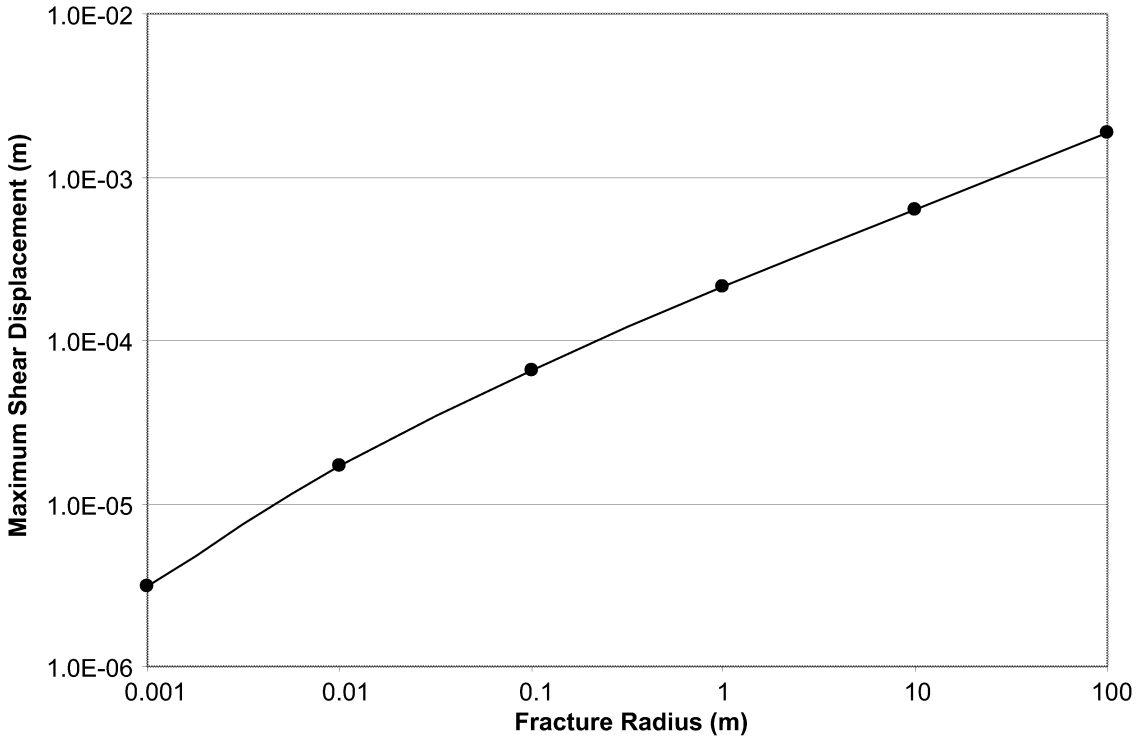


*Figure 3-4 Maximum shear displacement in the fracture as a function of the fracture radius*

### 3.2.5 Conclusions

The modeling results suggest the following conclusions:

1. For constant material properties and a constant angle between the loading stress and the fracture plane, the maximum shear displacement can be expressed as a function of the fracture radius.

2. For reasonably large fractures, e.g. radius < 100 m, the maximum shear displacement is far below the critical displacement of 100 mm that would compromise the integrity of the canister. The critical value of 100 mm that could lead to canister failure would involve extremely large fractures, ones that would most likely be identified during any site reconnaissance and avoided as canister locations. This implies that fractures that are sufficiently large to have slips exceeding 0.1 m are highly unlikely to be missed during the mapping that would take place during repository construction. Since canister holes could be placed a safe distance from these large fractures, if they are present, canister failures in a future repository due to induced fracture movements may be extremely unlikely.

3. The shear displacement model of Poly3D is friction free. In reality, a part of the strain energy applied to the fracture is consumed overriding the initial cohesion of the fracture and by friction processes due to the roughness of the fracture surface. The resulting slip of the fracture is less than the slip computing by Poly3D. The same remark can be made for Franc3D.

4. This task only concentrated on fracture propagation initiation. Fracture slip and propagation were treated as two uncoupled processes. This approach is still valid for the modeling of fracture propagation initiation. Modeling of the same system beyond propagation is much more complicated. In reality, as soon as a fracture begins to propagate, its geometry and state of stress change, sometimes radically. Both models should be updated continuously in small steps.

## 3.3 Task 2.2 – Fracture Interaction Effects

### 3.3.1 Results of the variation of the distance case

The stress intensity factors $K_I$ and $K_{II}$ are computed around the perimeter of the two fractures by the code Franc3D. The fracture propagation criterion is calculated for each fractures by Equation 9. Since the fractures are similar, the computed F criterions are almost equal. The small discrepancy between the F values is explained by a slight effect of the boundary of the model. Figure 3-5 shows the variation of the F factor as a function of angle for the two fractures when separated by 1m.

One can observe that the load applied to the system is larger than the critical load that initiates fracture propagation, since F>1 at some points. The peak observed at $270^o$ is due to the discretization step of $15^o$ chosen that is too coarse to show a smooth curve at $270^o$. The difference between the F factors is negligible around the perimeter of the fracture.

The maximum F factor is computed for the reference fracture for different distances between the fractures. The results of the analysis are presented in Figure 3-6 below.

The stress intensity factor F of the reference fracture increases as the fractures get closer to each other. The variation of the F factor is not linear. The F factor curve converges asymptotically toward a value equal to the F factor of a similar but single fracture. This F factor value can be assumed reached when the distance between the two fractures is 4 times the radius of the fractures. This distance is defined as the maximum influence distance of the system.

### 3.3.2 Results of the variation of the size of the disturbance fracture

The stress intensity factors $K_I$ and $K_{II}$ are computed around the perimeter of the two fractures by the code Franc3D. The fracture propagation criterion is calculated for each fractures by the Equation 9. Since the fractures are different in size, the computed F criterions are different, as seen in Figures 3-7 and 3-8.

The criterion of propagation initiation of the disturbance fracture increases as its radius increases. This could be predicted by Equations 17 through 20. The criterion of propagation initiation of the reference fracture $F_{max}$ decreases as the radius of the disturbance fracture increases. Also the risk for propagation is slightly reduced by the presence of a large fracture in the neighborhood. In term of fracture shearing, the presence of a larger fracture parallel to the reference fracture reduces the risk for large shear displacements, since the strain energy is distributed over the cumulated surfaces of the fractures.

## 3.4 Conclusions

The following conclusions of the fracture interaction on energy dissipation can be drawn:

1. For constant material properties and a constant angle between the loading stress and the fractures orientation, there exists a maximum distance of influence in terms of propagation criterion F between two identical fractures. This distance was found equal to four times the radius of the fractures. One can assume that the fractures behave as isolated when their distance is more than the maximum distance of influence.

2. When the distance between the two identical fractures decreases below the maximum distance of influence, the propagation criterion increases. Also the risk for fracture propagation increases when the fractures get closer.

3. Increasing the size of a particular fracture increases the risk for its propagation. On the other hand, it reduces slightly the risk for propagation of the parallel fractures in the neighborhood.

The study was carried out on a fracture with parallel orientation and specific geometry to investigate qualitatively the effect of distance and size on the risk of propagation. A more exhaustive investigation would be to carry out a similar analysis for different fracture orientations and the interactions of multiple fractures.

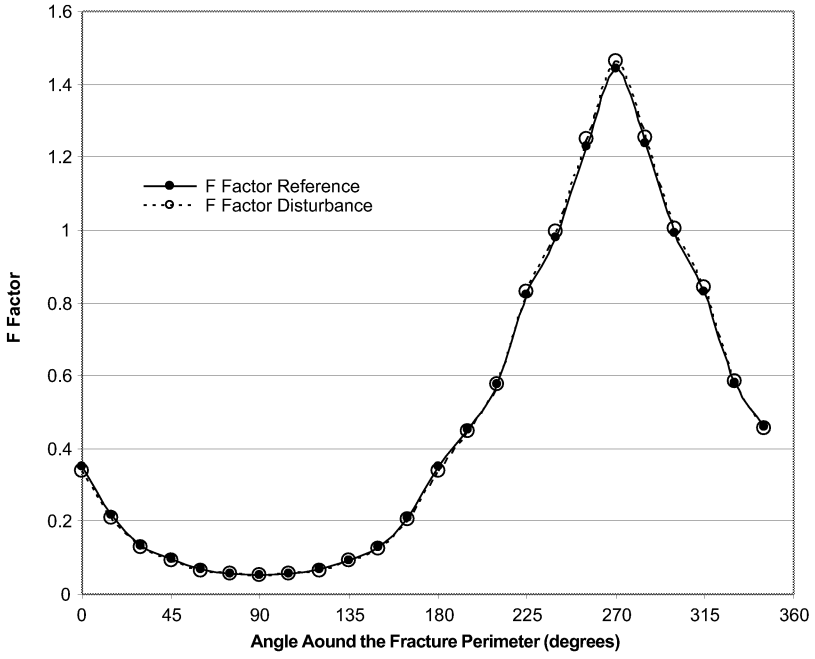


*Figure 3-5 Comparison of the F factor of the two fractures at a distance of 1m*

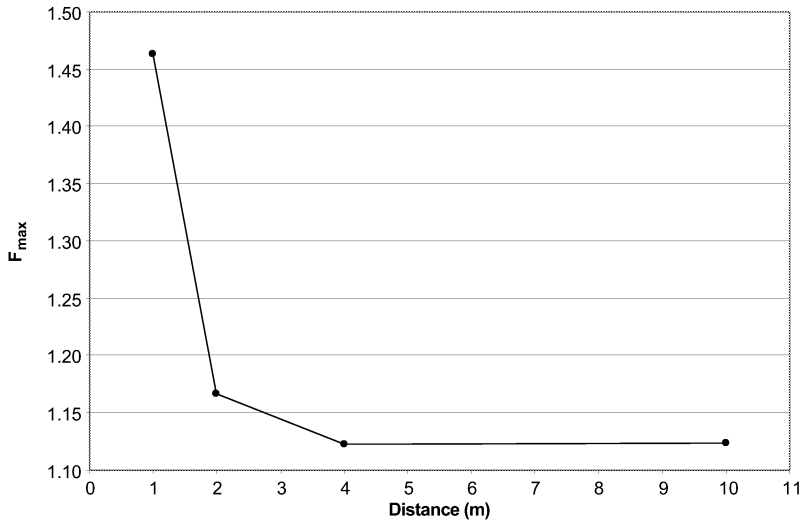


*Figure 3-6 Maximum F factor of the reference fracture as a function of the distance between the two fractures*

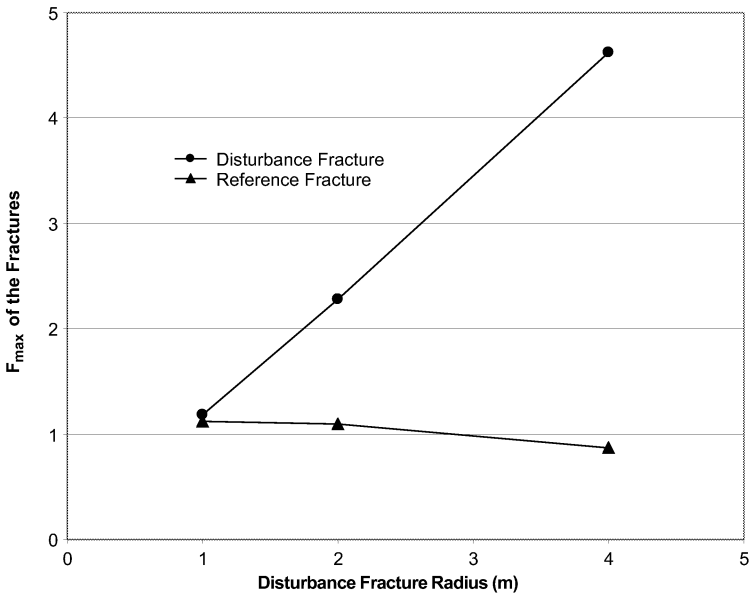


*Figure 3-7 Sensitivity of the reference fracture Fmax factor to the radius of the disturbance fracture at a distance of 4m*

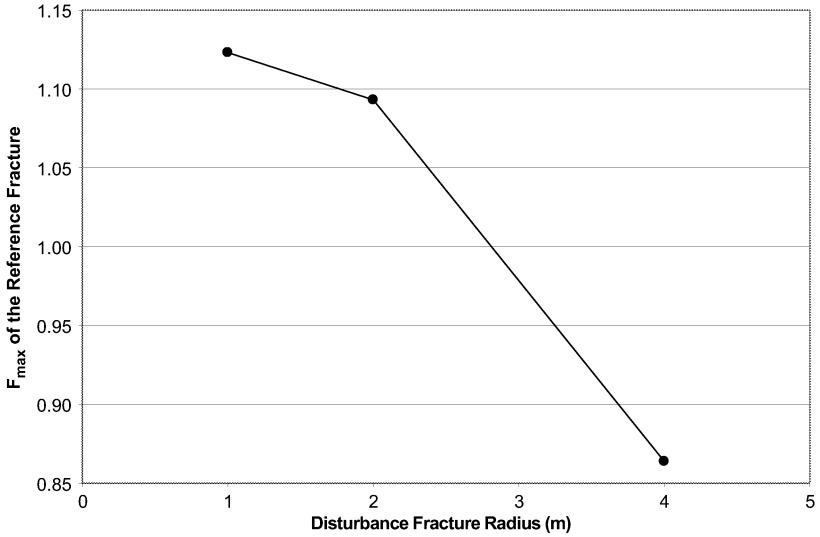


*Figure 3-8 Sensitivity of the reference fracture $F_{max}$ factor to the radius of the disturbance fracture at a distance of 4m*

## 3.5 Task 2.3 – Impact of Fracture Cohesion and Friction

The inclusion of fracture cohesion and friction will prevent fracture slippage in some instances. The question that is of greatest interest with regards to performance of a repository over the next 100,000 years is whether some of the canister failures reported in TR 99-03 would not have been predicted had these effects been taken into account. The results for the three cases of cohesion and friction angle shown in Table 1-4 are shown in Table 3-7. The results have been sorted by distance and magnitude intervals. The percentage number in each cell refers to the percentage of fractures that had 0.1 m or more of slip predicted that did not exceed the Mohr-Coulomb threshold. For example, an entry of 100% means that all of the fractures in that distance-magnitude range whose slips had previously been predicted to be greater than 0.1 m did not exceed the Mohr-Coulomb criterion, and so would not have failed. Table 3-7 shows how conservative the assumption of no friction and no cohesion may be. As shown in this Table, and by the Ceberg calculations reported in TR 99-03 (Table 5-7), most of the damaging earthquakes tend to occur between 100 m and 1 km of the repository. Even for the weakest set of assumptions, Table 3-7 shows that more than half of the induced slips greater than 0.1 m might not have taken place, since the Mohr-Coulomb criterion was not exceeded. Moreover, no earthquakes less than magnitude 6.0 for this distance range with predicted slips exceeding 0.1 m ever exceeded the Mohr-Coulomb criterion. Only 5% to 10% of the damaging earthquakes in the 6.0 to 7.0 magnitude range would have exceed the Mohr-Coulomb criterion. Since between 90% and 95% of all damaging earthquakes in the Ceberg example presented in TR 99-03 occurred at distances greater than 100 m

For earthquakes within 1 km, the reduction is on the order of 10% to 30%. At distances greater than 1 km, the impact is much greater. In fact, although the Figure extends to distances beyond 10 km, not a single earthquake beyond 10 km leads to induced slips greater than 0.1 m when the friction and cohesion cases are taken into account. This suggests that the radius of investigation for potential earthquakes should focus on the immediate region within 10 km of the repository, and can largely ignore potential

earthquakes outside this area. Figure 3-9 shows the reduction in canister failure percentage due to damaging earthquakes as a function of distance if the three scenarios are taken into account. A value of 50% would mean that half of the predicted canister failures would not take place, since the induced shear tractions would not be sufficient to overcome the cohesion and friction. A value of 100% would mean that taking friction into account would not have changed the results in TR 99-03.

**Table 3-6 Percentage of fractures originally exceeding the 0.1 m displacement threshold that did not exceed the Mohr-Coulomb criterion**

| **Cohesion = 0.1 MPa, Friction Angle = 25° (Intermediate Case)** | | | | | |
|---|---|---|---|---|---|
| | Distance Range | | | | |
| Earthquake Magnitude Range | 1 - 10 m | 10 m - 100 m | 100 m - 1 km | 1 km - 10 km | 10 km - 100 km |
| 8.0-8.5 | 1.17% | 1.60% | 55.64% | 100.00% | |
| 7-5-8.0 | 2.03% | 4.96% | 75.51% | 100.00% | |
| 7.0-7.5 | 3.28% | 11.37% | 93.84% | | |
| 6.5-7.0 | 5.65% | 32.21% | 100.00% | | |
| 6.0-6.5 | 13.37% | 46.55% | 97.41% | | |
| 5.5-6.0 | 24.50% | 33.42% | 100.00% | | |
| 5.0-5.5 | 10.60% | 26.83% | 100.00% | | |
| 4.5-5.0 | 65.98% | 59.81% | | | |
| 4.0-4.5 | 62.60% | 67.88% | No Fractures Exceeded 0.1 m | | |
| 3.5-4.0 | 69.86% | 86.61% | | | |
| 3.0-3.5 | 91.90% | 94.68% | | | |
| 2.5-3.0 | 100.00% | 98.41% | | | |
| 2.0-2.5 | 100.00% | 100.00% | | | |

| **Cohesion = 0.01 MPa, Friction Angle = 20° (Weakest Case)** | | | | | |
|---|---|---|---|---|---|
| | Distance Range | | | | |
| Earthquake Magnitude Range | 1 - 10 m | 10 m - 100 m | 100 m - 1 km | 1 km - 10 km | 10 km - 100 km |
| 8.0-8.5 | 0.88% | 1.04% | 51.70% | 100.00% | |
| 7-5-8.0 | 1.26% | 2.91% | 70.21% | 100.00% | |
| 7.0-7.5 | 2.28% | 8.27% | 91.82% | | |
| 6.5-7.0 | 3.46% | 28.70% | 100.00% | | |
| 6.0-6.5 | 8.86% | 43.55% | 92.59% | | |
| 5.5-6.0 | 18.66% | 30.43% | 100.00% | | |
| 5.0-5.5 | 6.40% | 20.65% | 100.00% | | |
| 4.5-5.0 | 60.77% | 54.32% | | | |
| 4.0-4.5 | 57.20% | 66.83% | | | |
| 3.5-4.0 | 66.32% | 83.48% | No Fractures Exceeded 0.1 m | | |
| 3.0-3.5 | 88.36% | 93.46% | | | |
| 2.5-3.0 | 100.00% | 98.41% | | | |
| 2.0-2.5 | 100.00% | 100.00% | | | |

| Cohesion = 1.0 MPa, Friction Angle = 30° (Strongest Case) | | | | | |
|---|---|---|---|---|---|
| | Distance Range | | | | |
| Earthquake Magnitude Range | 1 - 10 m | 10 m - 100 m | 100 m - 1 km | 1 km - 10 km | 10 km - 100 km |
| 8.0-8.5 | 1.95% | 2.41% | 65.12% | 100.00% | |
| 7-5-8.0 | 2.82% | 8.39% | 84.48% | 100.00% | |
| 7.0-7.5 | 6.17% | 16.67% | 95.79% | | |
| 6.5-7.0 | 9.04% | 39.12% | 100.00% | | |
| 6.0-6.5 | 19.24% | 50.45% | 99.63% | | |
| 5.5-6.0 | 33.39% | 37.24% | 100.00% | | |
| 5.0-5.5 | 17.89% | 32.82% | 100.00% | | |
| 4.5-5.0 | 71.39% | 64.24% | | | |
| 4.0-4.5 | 67.19% | 73.94% | No Fractures Exceeded 0.1 m | | |
| 3.5-4.0 | 86.15% | 90.91% | | | |
| 3.0-3.5 | 95.34% | 96.44% | | | |
| 2.5-3.0 | 100.00% | 98.41% | | | |
| 2.0-2.5 | 100.00% | 100.00% | | | |

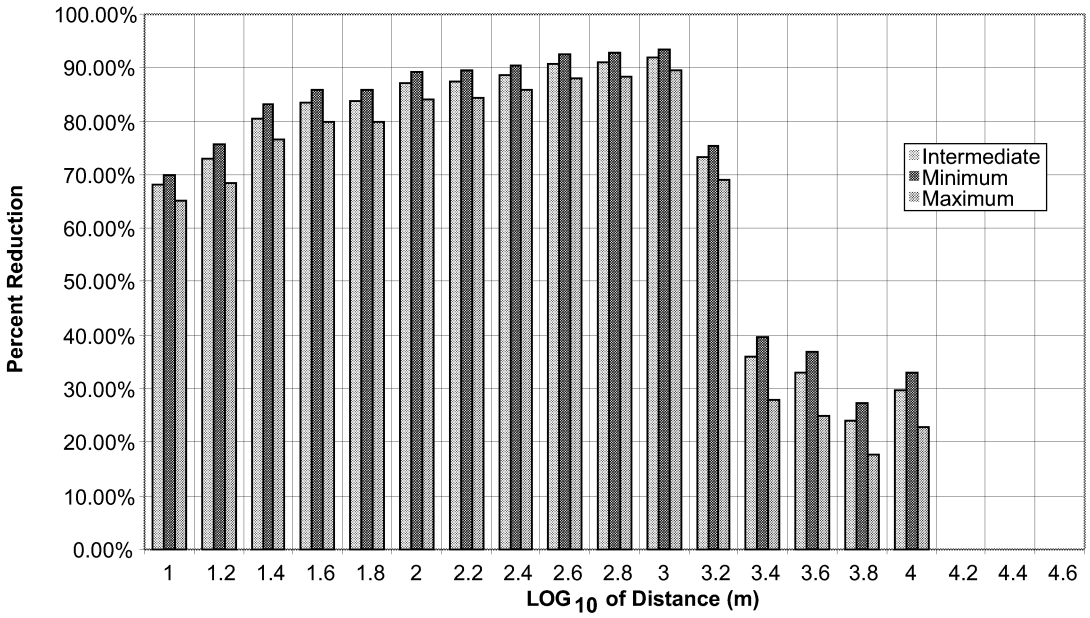


*Figure 3-9 Reduction in canister failure percentage due to incorporation of friction and cohesion effects*

# 4 CONCLUSIONS AND RECOMMENDATIONS

## 4.1 Conservativeness of the Methodology in TR 99-03

This study has shown that the estimates of canister failure reported in TR 99-03 are conservative. Three conservative assumptions were examined in detail: fracture propagation, fracture interactions, and fracture cohesion and friction. The results summarized in Chapter 3.2.6 suggest that fractures less than 100 m radius would use up most of the earthquake energy to propagate the fracture rather than to slip. The implications for the three generic sites where maximum fracture size was not much greater than 100 m is that none of the estimated canister failures might have taken place, or if they did, they would have been on very large (radius > 100 m) fractures that probably could be identified during site reconnaissance and avoided as canister locations, effectively reducing earthquake risk to 0.0.

Fracture interaction effects also show some reduction in slip. The analyses focused on the interactions of two parallel fractures. Even for this simple case, the impact could be measured on the fracture propagation criterion for the fracture intersecting the canister. The modeling results showed that even a single fracture parallel to the fracture intersecting the canister would require more energy for slip or propagation. Effects might be to increase the necessary energy by 10 percent or more.

Incorporation of fracture friction and cohesion suggests that predicted slip magnitudes, not considering fracture interaction effects or propagation, could be significantly reduced. The simulations reported in Section 3.5 suggest that the number of fractures with slips predicted to exceed 0.1 m in the case of frictionless and cohesionless fractures would be substantially reduced when cohesion and friction are considered. For smaller earthquakes and greater distances, almost 100% of the fractures that previously exceeded the 0.1 m threshold would not exceed the Mohr-Coulomb threshold, and would not slip. On the order of 10% to 50% of the fractures previously exceeding the 0.1 m threshold for larger earthquakes would not exceed the Mohr-Coulomb threshold. Thus, consideration of friction and cohesion alone ought to reduce the number of predicted canister failures by a minimum of 10%, and more likely by 50% to 90%.

When all three of these studies are taken into account, it seems plausible that the earthquake risk reported in TR 99-03 is highly conservative, and that for the three generic sites, the only fractures that might slip during the next 100,000 years are those that are so large that they would be easily detectable during site reconnaissance or repository construction.

## 4.2 Tools for Site Comparison

The sensitivity studies reported in Chapter 2.2 shows that knowledge of nothing more than the earthquake magnitude/frequency parameters for a given site can be used to predict risk characteristics for a single reference fracture. If fracture intensity and fracture size distributions are assumed to be similar for alternative sites, then a simple multiplication of the sensitivity matrix results with a matrix of earthquake magnitude/frequency can be used to rank alternative sites.

## 4.3 Tools for Estimating risk

Additional results reported in Chapter 2.2 show that the sensitivity analysis results can be combined with site-specific knowledge of fracture size and intensity to approximate the results of more detailed numerical simulations. While these estimates have a greater uncertainty than the results in TR 99-03, it is encouraging that their mean estimates of canister failure due to damaging earthquakes are within the same order of magnitude as the more sophisticated calculations of TR 99-03.

## 4.4 Critical Data for Estimating Earthquake Risk

Many parameters influence predicted displacements on fracture due to earthquakes. The most important is earthquake magnitude. Predicted displacement has a power law dependence on earthquake magnitude.

Several parameters exert a linear dependence on predicted displacements. These include fracture radius, distance between the earthquake and the fracture, and fracture intensity. For comparison of sites, fracture radius distribution and distance from earthquakes many not vary much; fracture intensity may be the parameter that accounts for the greatest differences.

A few parameters exert less than a linear dependence, like fracture orientation.

Since only earthquake greater than magnitude 6.0 produce slips greater than 0.1 m, the critical parameter for ranking sites may be the number of earthquakes with magnitudes greater than 6.0. This, coupled with the fracture intensity, are likely to be the two most critical parameters for assessing the relative risk of canister failure for alternative sites.

## 4.5 Earthquake Risk Relative to Canister Failure in Swedish Repositories

The conservative calculations reported in TR 99-03 suggested that canister failure due to movements along fractures intersecting these fractures as a result of earthquakes would be small. These calculations relied upon simplifications of the physical processes that take place during an earthquake. When the simplifications were further investigated, it was found that canister failure should be much less. Unless the repository is located in an area where magnitude 6.0 and greater earthquakes are much more likely to occur, and fracture intensity is much greater than the three generic sites, it is unlikely that canister failures will occur.

**ACKNOWLEDGEMENTS**

Dr. Bruce J. Carter of Cornell University provided valuable help with FRANC3D. The authors would also like to thank Raymond Munier for help developing the scope of this study and his enthusiasm throughout.

# 5 REFERENCES


Cornell University Fracture Group (1998). *Franc3D Users Guide*. Cornell Fracture Group, Cornell University, Ithaca, NY 14853, USA.

Coulomb, C.A. (1773). Sur une application des règles de Maximis et minimis a quelques problèmes de statique relatifs à l'Architechture, *Acad. Roy. Des Sciences Memoires de math. Et de physique par divers savans*, 7, 343-82.

Davison, F. and C. Scholz (1985). Frequency-moment distribution of earthquakes in the Aleutian Arc: A test of the characteristic earthquake model Bulletin of the Seismological Soc. America, Vol. 75, 1349-1361.

Hanks, T. C. and H. Kanamori (1979). A moment-magnitude scale. *J. Geophys. Res.*, Vol. 84, 2348-2350.

Hertzberg, R. W. (1976). *Deformation and Fracture Mechanics of Engineering Materials*. John Wiley & Sons, New York, 605 p.

Kijko, A., E. Skordas, R. Wahlström and P. Mäntyniemi (1993). Maximum likelihood estimation of seismic hazard for Sweden. Natural Hazards, Vol. 7, 41-57.

La Pointe, P. R. and J. A. Hudson (1985). *Characterization and Interpretation of Rock Mass Joint Patterns.* Special Paper 199, Geological Society of America Book Series.

La Pointe, P. R., P. Wallmann, A. Thomas and S. Follin (1997). A methodology to estimate earthquake effects on fractures intersecting canister holes. Svensk Kärnbränslehantering AB (*Swedish Nuclear Fuel and Waste Management Company)* Stockholm, Sweden, Technical Report 97-07. 61 p.

La Pointe, P. R., T. Cladouhos and S. Follin (1999). Calculation of displacements on fractures intersecting canisters induced by earthquakes: Aberg, Beberg and Ceberg examples. Svensk Kärnbränslehantering AB (*Swedish Nuclear Fuel and Waste Management Company)* Stockholm, Sweden, Technical Report 99-03. 103 p.

Li, V.C. (1991). Mechanics of shear rupture applied to earthquake zones. *Fracture Mechanics of Rock* (ed. B.K. Atkinson). Academic Press, London, 351-428

Mohr, O. (1900). Welche Umstände bedingen die Elastizitätsgrenze und dem Bruch eines materials? *Z. Ver. Dt. Ing.,* 44, 1524-30; 1572-77.

Pollard, D. D. and P. Segall (1987). Theoretical displacements and stresses near fractures in rock: with applications to faults, joints, veins, dikes and solution surfaces. *In Fracture Mechanics of Rock*, (ed. B.K. Atkinson). Academic Press Ltd., London.

Pusch, R. (1996). JADE, Jämförelse av bergmekaniska funktionssätt hos KBS3-V. KBS3-H och MLH, draft report.

Riddell, W., A. R. Ingraffea and P. A. Wawrzynek,. (1997). Experimental Observations and Numerical Predictions of Three-Dimensional Fatigue Crack Growth. *Eng. Fract. Mech.*, 58,4, 293-310.

Scholz, C. and C. A. Aviles, 1986). The fractal geometry of faults and faulting, *in* Earthquake Source Mechanics, AGU Monograph 37 (S. Das, J. Boatwright and C. Scholz, eds.) American Geophysical Union, Washington, D. C. pp. 147-155.

Shen, B. (1993). Mechanics of Fractures and Intervening Bridges in Hard Rocks, Ph. D. Thesis. Royal Institute of Technology KTH, Stockholm, Sweden

Slunga, R. (1985). The seismicity of southern Sweden 1979-1984, Final Report. FOA-Rapport C 20572-Tl (ISSN 0347-3694), Försvarets Forskningsanstalt (National Defense Research Institute), Stockholm, Sweden. 45p.

Wells, D. L. and K. J. Coppersmith (1994). New empirical relationships among magnitude, rupture length, rupture width, rupture area and surface displacement. *Bulletin of the Seismological Society of America*, 84(4), 974-1002.

Thomas, A. L. (1993). Poly3D: A three-dimensional polygonal element displacement discontinuity boundary element computer program with applications ot fractures, faults and cavities in the earth's crust. M. S. thesis, Stanford University, Stanford, CA. 221p.

Thomas, A.L., and Pollard, D.D. (1993). The geometry of echelon fractures in rock: implications from laboratory and numerical experiments. *Journal of Structural Geology* 15, 323-334.

# APPENDIX A

# DERIVATION OF PARENT FRACTURE POPULATION STATISTICS FROM TRACE LENGTH MEASUREMENTS FOR FRACTAL FRACTURE POPULATIONS

## A1 Overview

### A.1 1 Introduction

Published methods to estimate fracture size combine Discrete Fracture Network (DFN) modeling with a forward modeling approach to match various statistical parameters of the 1D or 2D data (Dershowitz and others, 1992[1]; La Pointe and others, 1993[2]). While these methods are very general and powerful, they require sophisticated numerical simulations.

Many researchers who have analyzed fracture geometry in wells, outcrop, lineament maps or seismic profiles have concluded that individual fracture sets often exhibit Power Law or fractal characteristics for many of their parameters, including fracture size. If a fracture set does conform to a fractal size distribution model, then it is possible to derive a host of useful equations that relate statistics for the observed fracture trace lengths to the statistics that describe the unobserved three-dimensional parent fracture population, making numerical simulations unnecessary. The sections that follow detail the derivation of these equations, and illustrate through numerical DFN simulations that they provide accurate estimates of the parent fracture population size statistics.

### A.1 2 Assumptions

For the equations developed in Sections 2 and 3, fractures are assumed to be planar and circular. The representation of fractures as circular discs, rather than as some other shape, is not a required assumption, but is convenient for the mathematical development presented in these sections. It turns out that the derived equations apply with minor modifications to fractures of other shapes, as discussed in Section 3.2.

---

[1] Dershowitz, W. S. (1992). Interpretation and synthesis of discrete fracture orientation, size, shape, spatial structure and hydrologic data by forward modelling. *Proceedings of the international Congress on fractured and Jointed Rock Masses*, Lake Tahoe, 3-5 June 1992. A. A. Balkema, Rotterdam. pp. 579-586.

[2] La Pointe, P. R., P. C. Wallmann and W. S. Dershowitz (1993). Stochastic estimation of fracture size from simulated sampling. Int. Jour. Rock Mech., Min. Sci. & Geomech. Abstr. v. 30, 1611-1617.

It is also convenient to characterize fracture size by the effective radius of the fracture, since this parameter is often used in modeling simulations or engineering calculations. The effective radius of a fracture is defined as the radius of a circular fracture that has the same area as the actual fracture. Critical equations in the text are highlighted by a surrounding box.

# A2 PARENT FRACTURE POPULATION STATISTICS

## A.2 1 Functional Forms for the Parent Fracture Radius Distribution

A group of fractures that have a Power Law or fractal radius distribution implies that the Complementary Cumulative Density Function (CCDF) of the fracture radii conforms to a power law. The CCDF is defined as the probability that a fracture radius is equal to or greater than a particular radius. Power Law distributions require the specification of a minimum value for their distributional mass and moments to be finite. The probability that a value is equal to or greater than the minimum value is 1.0, while the probability that the radius is greater than or equal to infinity is 0.0. The formal representation of the CCDF is given by Equation 1:

$$G(x) = \left(\frac{x_0}{x}\right)^D \tag{1}$$

where $x_0$ is the minimum (radius) value,
$x$ is any fracture radius between $x_0$ and $\infty$,
$D$ is the exponent of fractal dimension, and
$G(x)$ is the probability that $x$ is greater than or equal to $x_0$.

The Cumulative Density Function (CDF) of the three-dimensional radius distribution, is defined as:

$$F(x) = 1 - G(x) = 1 - \left(\frac{x_0}{x}\right)^D \tag{2}$$

The Probability Density Function (PDF) defined as the derivative of the cumulative density function:

$$f(x) = \frac{\partial}{\partial x} F(x) = \frac{D x_0^{\,D}}{x^{D+1}} \tag{3}$$

Note that the PDF and CCDF have a power law functional form, and so would plot as a straight line on doubly logarithmic axes, while the CDF does not have a power law functional form, and would not plot as a straight line on doubly logarithmic axes.

## A.2 2 Mean Value

Statistical distributions can be characterized by their moments, such as their mean or standard deviation. Power law distributions differ from many common distributions, like the lognormal or the exponential, in that their moments are not always finite. For power law distributions, the value of $D$ governs whether a particular moment is finite or not, as is shown in this section in the Section 2.3. These considerations are important for

using trace length data to infer the population characteristics of the parent fracture population.

The mean radius ($\mu$) is defined as the expected value (*E[]*) of the radius distribution, or:

$$\mu = E[f(x)] = \int_{x_0}^{\infty} x f(x) \partial x \tag{4a}$$

$$= D x_0^{\,D} \int_{x_0}^{\infty} x^{-D} \partial x \tag{4b}$$

$$= \frac{D x_0^{\,D}}{1-D} x^{-D+1} \Big|_{x_0}^{\infty} \tag{4c}$$

$$= \frac{D x_0^{\,D}}{1-D} \left[ \infty^{1-D} - x_0^{\,1-D} \right] \tag{4d}$$

Now the term $\infty^{1-D}$ will not vanish unless $D > 1.0$, which implies that the mean value is not finite unless $D > 1.0$. For $D > 1.0$, Equation 4d becomes:

$$\mu = \frac{D x_0^{D}}{D-1} x_0^{1-D} \tag{5a}$$

or

$$\boxed{\mu = \frac{D x_0}{D-1}} \tag{5b}$$

Equation 5b represents the expected value, or mean radius for the distribution for the case where $D > 1.0$.

## A.2 3 Variance and Standard Deviation

The variance of a function is defined as:

$$\sigma^2 = \int_{x_0}^{\infty} f(x) * (x-\mu)^2 \partial x \tag{6}$$

where *f(x)* is the probability density function (pdf) for *x*,

$\mu$ is the mean or expected value of *x*, and

$x_0$ is the minimum value of *x* and

$\sigma^2$ is the variance.

As has been shown, the PDF of x for a Power law distribution is given by:

$$f(x) = \frac{D{x_0}^D}{x^{D+1}} \tag{7}$$

and the mean or expected value of the distribution is:

$$\mu = \frac{x_0 D}{D-1} \tag{8}$$

So, inserting these two expressions into Equation 6 yields:

$$\sigma^2 = \int_{x_0}^{\infty} \left(\frac{D{x_0}^D}{x^{D+1}}\right) * \left(x - \frac{x_0 D}{D-1}\right)^2 \partial x \tag{9}$$

Expanding the terms in brackets and bringing quantities not dependent upon $x$ outside of the integration brackets yields:

$$\sigma^2 = D x_0^D \int_{x_0}^{\infty} \left[ x^{1-D} - \frac{2x_0 D x^{-D}}{D-1} + \frac{x_0^2 D^2 x^{-D-1}}{(D-1)^2} \right] \partial x \tag{10}$$

Carrying out the integration produces:

$$\sigma^2 = D x_0^D * \left[ \frac{x^{2-D}}{2-D} - \frac{2x_0 D}{D-1} * \frac{x^{-D+1}}{1-D} + \frac{x_0^2 D^2}{(D-1)^2} * \frac{x^{-D}}{(-D)} \right]_{x_0}^{\infty} \tag{11}$$

Now this quantity is finite iff $D > 2.0$. Thus,

$\forall D > 2.0$,

$$\sigma^2 = -D x_0^D * \left[ \frac{x_o^{2-D}}{2-D} + \frac{2x_0 D x_0^{-D+1}}{(D-1)^2} - \frac{x_0^2 D^2 x_0^{-D}}{D(D-1)^2} \right] \tag{12a}$$

$$= -D x_0^D * x_o^{2-D} * \left( \frac{1}{2-D} + \frac{D}{(D-1)^2} \right) \tag{12b}$$

$$\boxed{\sigma^2 = \frac{x_0^2}{(D-1)^2} * \frac{D}{D-2}} \tag{13}$$

Since the standard deviation, $\sigma$, equals $\sqrt{(\sigma^2)}$, the standard deviation of the radius distribution is:

$$\boxed{\sigma = \frac{x_0}{D-1} * \sqrt{\frac{D}{D-2}}} \tag{14}$$

# A3 TRACE LENGTH STATISTIC

The traces observed on a planar surface, such as an outcrop, are biased in that larger fractures have a higher probability of intersecting the surface than do smaller ones. The solution to the problem of how the scaling properties of trace lengths relate to the scaling properties of the parent fracture radius distribution requires decomposition of the problem into two stages:

The relation between the radius distribution of the parent fracture population and the radius distribution of the fracture population intersecting the trace plane; and

The relation between the radius distribution of fractures intersecting a trace plane and the observed trace length distribution.

Section 3.1 analyzes the relation between the parent and intersecting radii distributions, while Section 3.2 examines the relation between the radius distribution of the intersecting fractures and the observed trace length distribution. The reason why the problem needs to be decomposed is in part to facilitate a clearer exposition of the mathematics, and in part due to the fact that the relation between trace lengths and the intersecting fracture radius distribution requires an assumption about fracture shape.

## A.3 1 Relation Between the Radius Distribution of the Parent Fracture Population and the Radius Distribution of Fractures Intersecting a Plane

### A3.1.1 Probability Density Functions

La Pointe and Hudson (1985)[3] showed that, for the assumption that fractures are circular, planar discs, the probability of a fracture intersecting a plane is linearly proportional to the fracture radius. In general, if the fracture is represented by any convex polygonal shape, the probability of the intersection is proportional to the dimension of the polygon parallel to the plane. For simplicity, we consider circular fractures in the following derivations.

Denoting the radius distribution of the parent fracture population by *f(x)* as in Equation 7, the radius distribution for fractures intersecting a plane is given by:

$$o(x) = xf(x) = D\left(\frac{x_0}{x}\right)^D \tag{15}$$

where *o(x)*is the radius distribution of the intersecting fractures.

---

[3] La Pointe, P. R. and J. A. Hudson (1985). *Characterization and Interpretation of Rock Mass Joint Patterns*. Special Paper 199, Geological Society of America Book Series.

The above expression is not a proper probability distribution function, since it does not integrate to 1.0 between $x_0$ and ∞. A correction (*C*) must be made to insure that the total probability density equals 1.0:

$$C\int_{x_0}^{\infty} o(x) \equiv 1.0 \text{ or} \tag{16a}$$

$$C\frac{Dx_0}{D-1} \equiv 1.0 \tag{16b}$$

$$\mathrm{C} = \frac{\mathrm{D\text{-}1}}{\mathrm{Dx_o}} \tag{16c}$$

So

$$\mathrm{f_{int}}(x) = \frac{\mathrm{D\text{-}1}}{\mathrm{Dx_o}} xf(x) \tag{16d}$$

Or

$$\boxed{f_{int}(x) = (D-1)\frac{x_0^{D-1}}{x^D}} \tag{16e}$$

Now the CDF is the integral of the PDF, or:

$$F_{\mathrm{int}}(x) = \frac{D-1}{Dx_0}\int_{x_0}^{x} f_{\mathrm{int}}(x)\partial x \tag{17a}$$

$$= \frac{D-1}{Dx_0} * \frac{Dx_0}{1-D}\left[x^{1-D} - {x_0}^{1-D}\right] \tag{17b}$$

$$= -x_0\left[x^{1-D} - {x_0}^{1-D}\right] \tag{17c}$$

$$= \left(\frac{x_0}{x}\right)^{D-1} + 1 \tag{17d}$$

$$\boxed{F_{\mathrm{int}}(x) = 1 - \left(\frac{x_0}{x}\right)^{D-1}} \tag{17e}$$

This implies that $G_{int}(x)$, the CCDF of the trace lengths, is:

$$\boxed{G_{\mathrm{int}}(x) = 1 - F_{\mathrm{int}}(x) = \left(\frac{x_0}{x}\right)^{D-1} \therefore} \tag{18}$$

Thus, if it were possible to plot the CCDF of the radii of the intersecting circular fractures, the slope of the line would be equal to slope for the true, three-dimensional radius distribution minus 1.0.

### A3.1.2 Mean Value

It is straightforward to derive the expected value, or mean radius value for the intersecting fractures:

$$\mu_{\text{int}} = E[f(x)] = \frac{D-1}{Dx_0}\int_{x_0}^{\infty} x^2 f(x)\partial x = (D-1)x_0^{D-1}\int_{x_0}^{\infty} x^{1-D}\partial x \tag{19a}$$

$$= \left(\frac{(D-1)x_0^{\,2-D}}{2-D}\right) x^{2-D}\Big|_{x_0}^{\infty} \tag{19b}$$

$$= \left(\frac{(D-1)x_0^{\,2-D}}{2-D}\right)\left[\infty^{2-D} - x_0^{\,2-D}\right] \tag{19c}$$

$$= \left(\frac{(D-1)x_0^{D-1}}{2-D}\right)\left[0 - x_0^{2-D}\right] \tag{19d}$$

The equation above is finite if $D>2.0$. So, for $D > 2.0$, the above equation becomes:

$$\frac{(D-1)}{(D-2)} x_0^{\,D-1} x_0^{2-D} \tag{20a}$$

$$\boxed{\mu_{\text{int}} = \frac{x_0(D-1)}{D-2}} \tag{20b}$$

### A3.1.3 Variance and Standard Deviation

The derivation of the variance of the radii of intersecting fractures can be simplified by making a simple variable transformation and considering the independence of $D$ and $x$.

Let $D' = D - 1.0$ (21)

Then Equations 16e, 17e, 18 and 20b become:

$$f_{\text{int}}(x) = \frac{D' x_0^{\,D'}}{x^{D'+1}} \tag{22}$$

$$F_{\text{int}}(x) = 1 - \left(\frac{x_0}{x}\right)^{D'} \tag{23}$$

$$G_{\text{int}}(x) = \left(\frac{x_0}{x}\right)^{D'} \tag{24}$$

$$\mu_{\text{int}} = \frac{x_0 D'}{D' - 1} \tag{25}$$

These equations show that the statistical quantities associated with intersecting fracture radius distribution are identical in form to the three-dimensional radius distribution if the substitution $D' = D - 1$ is made in the three-dimensional radius formulae.

Because $D'$ does not depend upon $x$, the variance ($\sigma^2_{traces}$) and standard deviation ($\sigma_{traces}$) for the intersecting fracture radius distributions will have the forms:

$$\sigma^2_{\text{int}} = \frac{x_0^2}{(D'-1)^2} * \frac{D'}{D'-2} \tag{26}$$

$$\sigma_{\text{int}} = \frac{x_0}{D'-1} * \sqrt{\frac{D'}{D'-2}} \tag{27}$$

where $D' = D - 1$.

This implies that the exponent for the radius distribution of fractures intersecting a plane can be used to calculate the correct three-dimensional radius distribution by simply adding 1.0 to the exponent, and statistics such as the mean and standard deviation of radius size can be calculated from the intersecting fracture distribution. Although the radius distribution of the intersecting fractures cannot be directly measured, it can be estimated from the trace length distribution as described in the next section.

## A.3 2 Relation Between Intersecting Fracture Radius Distribution and the Observed Trace Length Distribution

Unfortunately, the radius of a fracture cannot be measured in outcrop, so it is impossible to compute the scaling properties of the intersecting fracture population. This is true whether the fracture sizes are fractal or follow any other distribution. However, it turns out that for the fracture shape geometry often assumed for fractures, it is possible to derive relatively simple relations between the observed fracture trace length population and the radius distribution of the intersecting fractures. It turns out that the scaling property of the radii of fractures intersecting a plane is identical to the scaling properties of the observed trace lengths!

As an illustration, consider a single circular fracture of radius $R$, oriented perpendicular to a trace plane. If the fracture intersects the plane, then the trace can vary in length from *0.0* to *2R*. As shown in Figure 1, the trace length can be expressed as a function of distance $z$ between the fracture center and the trace plane, and the fracture radius, according to the equation:

$$T = 2\sqrt{R^2 - z^2} \tag{28}$$

The mean observed trace length, $T_\mu$ is calculated as:

$$T_\mu = \frac{1}{R}\int_0^R 2\sqrt{R^2 - z^2}\,\partial z \tag{29}$$

or, carrying out the integration,

$$T_{\mu} = \frac{\pi R}{2} \tag{30}$$

Equation 30 is significant in that is shows that the mean observed trace length is equal to the radius multiplied by a constant. This means that the expected distribution of trace lengths is equal to the distribution of radii of the intersecting fractures multiplied by the constant $\pi/2$. In a log-log plot, multiplication of a power law function by a constant does not change its slope. This implies that the scaling exponent of trace lengths will be the same as the scaling exponent of the radius distribution of intersecting

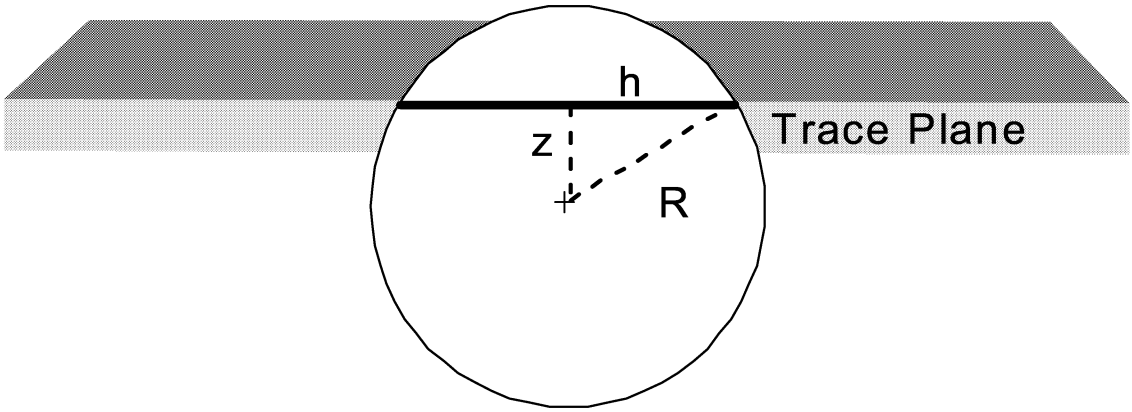


*Figure 1. Fracture intersection with trace plane.*

fractures. Moreover, the scaling exponent of the trace lengths will be equal to one less than the scaling exponent of the radius distribution of the parent fracture population.

Now consider fractures of other shapes. For rectangular fractures in which at least two sides are parallel to the plane, the trace of an intersecting fracture will always be equal to the length of the side that is parallel. This type of fracture shape would represent a fracture that is confined between two bedding planes or terminates on the upper and lower surfaces of a mechanical layer. In this situation, the relation between the observed trace length and the intersecting fracture is:

$$T = L \tag{31}$$

Where $T$ is the observed trace length, and $L$ is the length of the side that intersects the bedding or layer boundary. $T_{\mu} = T$, and so $T_{\mu}$ in Equation 31 is also directly proportional to $R$, as in Equation 30. The only difference is that the multiplicative constant is *1.0* instead of $\pi/2$. Thus, the scaling exponent for the trace lengths will also be equal to the scaling exponent of the intersecting fracture polygon radius (or edge length) distribution.

These two simple examples indicate that for any planar, anisotropic convex polygon, so long as one of its directions of anisotropy is parallel to the trace plane, the scaling exponent of the traces should be equal to the scaling exponent of the dimension of the intersecting fracture that parallels the trace plane. this, in turn, will be equal to the scaling exponent of the same dimension of the parent fracture population minus 1.0.

## A.3 3 Verification

Since it is not possible to verify the equations derived in Sections 3.1 and 3.2 from field data, as the three-dimensional fracture population cannot be observed directly or through others means, such as geophysics, numerical models of fractures were constructed for this purpose.

Three DFN models were constructed to verify the equations. The models had different combinations of values of the exponent and minimum size, and also orientation. The parameter values are summarized in Table 1 below.

**Table 1. Parameters used in simulations**

| Simulation # | D | Minimum Size | Orientation |
|---|---|---|---|
| 1 | 3.5 | 1.0 | Constant, (90., 0.) |
| 2 | 2.5 | 5.0 | Constant, (45., 45.) |
| 3 | 1.5 | 0.5 | Fisher, (0., 0.), $\kappa$ = 0.0 |

All fractures were generated within a 100-m cube embedded with a larger 200 m cube in order to minimize truncation effects on observed trace lengths of fractures terminating against the outer surfaces of the model. 5000 fractures were generated in each model simulation. Locations were selected at random throughout the 100-m cube generation region.

After each simulation was created, a horizontal trace plane was inserted into each of the three models, and the traces saved in a file for subsequent trace length analysis. The names of the files containing the three-dimension DFN model, the trace plane results, and the horizontal plane sampling file are listed in Table 2.

**Table 2. List of file names for verification tests.**

| Simulation # | 3D DFN file | Trace Length File |
|---|---|---|
| 1 | Sim1.fab | Sim1.f2d |
| 2 | Sim2.fab | Sim2.f2d |
| 3 | Sim3d.fab | Sim3d.f2d |
| Trace Plane | Htplane.sab | |

The first series of verification tests are on the 3D DFN model itself. Each simulation is created essentially through the generation of a uniformly random field of numbers over the interval (0,1), and then transformation of this field into a power law distribution through Gaussian anamorphosis. This procedure sets the cumulative probability of the uniform field equal to the cumulative probability of the power law distribution, or:

$$U = 1 - \left( \frac{x_0}{x} \right)^D, \; where \; U \in (0.0, 1.0) \tag{32}$$

Solving this equation for $x$ yields:

$$x = \frac{x_0}{(1-U)^{\frac{1}{D}}} \tag{33}$$

The resulting random realization of $x$ will have a power law distribution characterized by Equations 1, 2, 3, 5b and 14.

$D$ and $x_0$ were estimated (denoted in Table 3 as $D^*$ and $x_0^*$) through non-linear estimation of the CCDF function (Equation 3) for the radii of the 5000 fractures actually generated. In addition, the mean radius and the standard deviation of the radius distribution were estimated from Equations 5b and 14, respectively, from $D^*$ and $x_0^*$ for the cases where these moments were finite. These were then compared to the values actually calculated from the 5000 radius values for each of the fractures. The results shown in Table 3 verify that the simulation method produced three-dimensional fracture models with the desired power law characteristics, and that the mean and standard deviation of the radius distribution can be reliably estimated through Equations 5b and 14. Figure 2 shows the results of the non-linear fits for each CCDF.

**Table 3. Comparison of simulation results with predicted results**

| **Simulation** | **Specified D** | **Specified $x_0$** | **Estimated D ($D^*$)** | **Estimated $x_0$ ($x_0^*$)** |
|---|---|---|---|---|
| 1 | 3.5 | 1.0 | 3.47 | 1.00 |
| 2 | 2.5 | 5.0 | 2.44 | 5.00 |
| 3 | 1.5 | 0.5 | 1.50 | 0.50 |
| Simulation | Predicted Mean | Predicted σ | Calculated Mean | Calculated σ |
| 1 | 1.40 | 0.62 | 1.40 | 0.57 |
| 2 | 8.48 | 8.20 | 8.47 | 6.29 |
| 3 | 1.49 | | 1.47 | |

In Table 3, the standard deviations for Simulation 3 were not calculated since $D < 2.0$, which violates the constraint used to derive Equation 14.

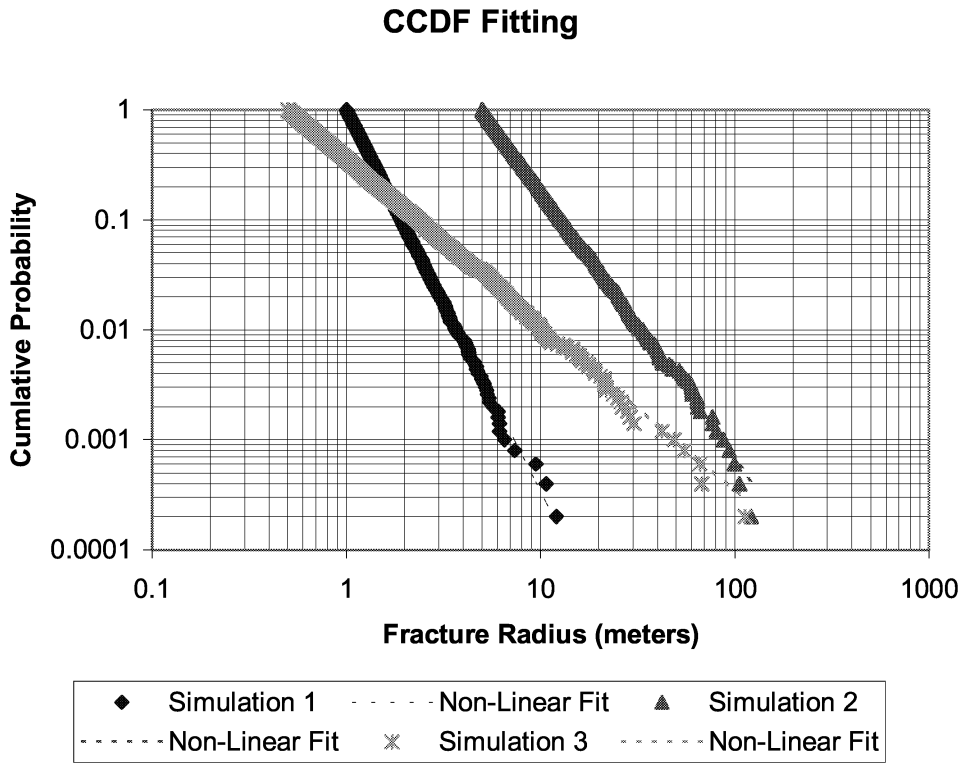


*Figure 2. Complementary Cumulative Density Functions (CCDF) of fracture radii for three simulations. Dashed lines represent non-linear fit to Equation 14.*

The next stage in the verification process is to the trace length distributions using the files listed in Table 1. The scaling exponents of the trace length distributions are given in Table 4, and non-linear fits to the trace length distributions are shown in Figure 2.

**Table 4. Parameter values estimated for the observed trace lengths.**

| Simulation | D | $x_0$ | Mean |
|---|---|---|---|
| 1 | 2.50 | 84.53 | 2.55 |
| 2 | 1.52 | 16218.1 | 20.32 |
| 3 | 0.54 | 31117.2 | 10.27 |

**Table 5. Parameters for the radius distribution of fractures intersecting the trace plane.**

| Simulation | D | $x_0$ | Mean | Mean Predicted From Mean Trace |
|---|---|---|---|---|
| 1 | 2.51 | 1.00 | 1.67 | 1.62 |
| 2 | 1.48 | 5.02 | 12.85 | 12.94 |
| 3 | 0.51 | 0.51 | 7.15 | 6.54 |

In Table 5, the mean radius has been predicted from the mean trace length using Equation 30, which multiplies the mean trace length by $2/\pi$. A comparison of Tables 4 and 5 shows that the trace length exponent and the radius exponent are in excellent agreement, and also that the mean radius is well-predicted from the mean trace length.

Equation 25 shows that the parameter, $x_0$, can be estimated from $D$ and $\mu$ or $\sigma$. For Simulation 1, the only simulation in which both first- and second-order moments are finite (since $D > 2.0$), the values of $D$ and $\mu$ can be used to estimate $x_0$:

$$x_0 = \frac{\mu(D-1)}{D} \tag{34a}$$

or

$$x_0 = \frac{1.62 * (2.50 - 1.00)}{2.50} = 0.972 \tag{34b}$$

This is very close to the actual simulation mean of 1.00.

Since $x_0$ and $D$ are now estimated for the radius distribution of fractures intersecting the plane, the values for the parent fracture population radius distribution are:

$$D_{fractures} = 2.50 + 1.0 = 3.50 \tag{35a}$$

$$x_o(fractures) = x_o(\text{intersecting fractures}) = 0.972 \tag{35b}$$

In turn, these values can be put into Equations 5b and 14 to compute the mean and standard deviation of the radius distribution of the parent fracture population:

$$\mu_{fractures} = \frac{0.972 * 3.50}{3.50 - 1.0} = 1.36 \tag{36a}$$

$$\sigma_{fractures} = \frac{0.972}{3.50 - 1.00}\sqrt{\frac{3.50}{1.50}} = 0.59 \tag{36b}$$

The actual values for the simulation are 1.40 and 0.57, respectively. This illustration shows that it is possible to make quite accurate predictions of the parent population from trace length data alone, and that the scaling exponent of trace lengths for a fractal fracture population is 1.0 less than the scaling exponent of the parent fracture radius distribution.

# A4 MODIFICATION FOR ROUGH OUTCROP SURFACES OR OTHER NON-PLANAR SAMPLES

## A.4 1 Overview

Natural objects, such as fractures, have been shown to have many fractal properties. However, these properties are typically sampled by methods that have a particular dimension. For example, boreholes or scanlines have a dimension of 1.0, since they are (if their width is neglected) line samples. Another typical sample is a surface, which may or may not be approximately planar. Examples include outcrops, underground exposures, lineament maps and two-dimensional seismic profiles.

The equations developed in Sections 2 and 3 were for perfectly planar surfaces. Section 4 extends the equations in those sections to any general fractal or Euclidean sampling object. The basis for the method relies upon a theorem in topology (Mandelbrot, 1983) that states that the co-dimension of the intersection of two sets is equal to the sum of the co-dimensions of each set.

The theorem also extends to *n* sets. This theorem does not require the sets to be fractal, but certainly can be used for fractal sets.

The co-dimension of a set is denoted by *C*. The dimension of the set is denoted by *D*. Then, the co-dimension is related to the dimension as:

$$C = E - D \tag{37}$$

where *E* is the Euclidean dimension of the space in which the sets exist.

For a volume of rock, $E = 3.0$.

Suppose a set of fractures has a dimension $D_f$. Then the co-dimension is:

$$C_f = E_3 - D_f \tag{38}$$

where $E_3$ is the Euclidean dimension of the embedding space, in this case, 3.0.

A plane within a volume has a dimension of 2.0, and a line has a dimension of 1.0. Thus:

$$C_{plane} = E_3 - 2.0 \tag{39a}$$

$$C_{line} = E_3 - 1.0 \tag{39b}$$

According to the theorem, the intersection of the fracture set and a plane has a co-dimension equal to the sum of the individual co-dimensions, or:

$$C_{traces} = C_{fractures} + C_{plane} \tag{40}$$

which implies that:

$$C_{traces} = E_3 - D_{fractures} + E_3 - D_{plane} \tag{41}$$

or

$$D_{traces} = E_3 - (E_3 - D_{fractures} + E_3 - D_{plane}) \tag{42}$$

or

$$D_{traces} = D_{fractures} + D_{plane} - E_3 \tag{43}$$

and, after inserting the numerical values for $D_{plane}$ and $E_3$,

$$D_{traces} = D_{fractures} + 2 - 3 = D_{fractures} - 1 \tag{44}$$

Thus, the dimension of the trace plane pattern is equal to the dimension of the parent fracture population minus 1.0. A similar line of reasoning shows that the dimension of a line sample will be equal to the dimension of the parent population minus 2.0.

Note that Equation 35 is identical to Equation 21. In fact, Equation 34 could be re-written for a fractal sampling object of any dimension:

$$D_{traces} = D_{fractures} + D_{sampling\ object} - E_3 \tag{45}$$

So, for example, assume that the traces were on a rough fractal surface whose dimension is $D = 2.5$. Then by substitution in Equation 37, the dimension of the traces is:

$$D_{traces} = D_{fractures} + 2.5 - 3.0 \tag{46}$$

or

$$D_{traces} = D_{fractures} - 0.5 \tag{47}$$

In this case, $D' = D - 0.5$, rather than $D - 1.0$ as in the case with a perfectly planar surface. This value of $D'$ would be substituted into Equations 22 through 27 to compute the appropriate fracture radius statistics from the observed trace lengths.

ISSN 1404-0344

CM Digitaltryck, Bromma, 2000